Universidade de Aveiro Departamento de Engenharia Civil
2014

José Filipe Miranda Melo

CARACTERIZAÇÃO DA RESPOSTA CÍCLICA DE ELEMENTOS DE BETÃO ARMADO COM ARMADURA LISA

CHARACTERISATION OF THE CYCLIC RESPONSE OF REINFORCED CONCRETE ELEMENTS WITH PLAIN BARS

Universidade de Aveiro Departamento de Engenharia Civil
2014

José Filipe Miranda Melo

CARACTERIZAÇÃO DA RESPOSTA CÍCLICA DE ELEMENTOS DE BETÃO ARMADO COM ARMADURA LISA

CHARACTERISATION OF THE CYCLIC BEHAVIOUR OF REINFORCED CONCRETE ELEMENTS WITH PLAIN BARS

Tese apresentada à Universidade de Aveiro para cumprimento dos requisitos necessários à obtenção do grau de Doutor em Engenharia Civil, realizada sob a orientação científica do Prof. Doutor Humberto Varum, Professor Catedrático do Departamento de Engenharia Civil da Faculdade de Engenharia da Universidade do Porto, e coorientação da Prof. Doutora Tiziana Rossetto, Professora Catedrática do Department of Civil, Environmental & Geomatic Engineering da University College London.

Apoio financeiro da FCT e do FSE no âmbito do III Quadro Comunitário de Apoio.

POPH QUALIFICAR É CRESCER. QUADRO DE REFERÊNCIA ESTRATÉGICO NACIONAL PORTUGAL 2007.2013 GOVERNO DA REPÚBLICA PORTUGUESA UNIÃO EUROPEIA Fundo Social Europeu

o júri

presidente

Prof. Doutor Armando da Costa Duarte
professor catedrático da Universidade de Aveiro

Prof. Doutor Humberto Varum
professor catedrático da Faculdade de Engenharia da Universidade do Porto

Prof. Doutor Aníbal Costa
professor catedrático da Universidade de Aveiro

Prof. Doutor António Arêde
professor associado da Faculdade de Engenharia da Universidade do Porto

Prof. Doutor José Sena Cruz
professor associado da Escola de Engenharia da Universidade do Minho

Prof. Doutor Hugo Rodrigues
professor adjunto da Escola Superior de Tecnologia e Gestão de Leiria do Instituto Politécnico de Leiria

agradecimentos

acknowledgements

Firstly, I would like to express my gratefulness to Professor Humberto Varum, supervisor of this thesis, who has been coordinating my academic career since the beginning. I also thank him for the constant motivation, friendship and dedication.

To Professor Tiziana Rossetto, co-supervisor of this thesis, for her guidance, friendship and encouragement, especially when I was at University College London for one year.

To Professor Aníbal Costa, for his advices in the definition of the experimental campaign.

To Professor Hugo Rodrigues, for his friendship, motivation and assistance in the numerical modelling.

To Eng. Randolph Borg, for his support, friendship and assistance in the experimental testing campaign.

To Eng. Renato Garcia, Eng. Silvia Louro and Eng. Diogo Mariano, for their friendship and assistance in the experimental programme.

To the staff of the Civil Engineering Laboratory at the University of Aveiro, for the support in the preparation and development of the testing campaign.

To Fundação para a Ciência e a Tecnologia, for the financial support provided in the form of the PhD grant with reference SFRH/BD/62110/2009.

To University College London for hosting me during one year of my PhD studies.

To my wife Tânia, for her constant encouragement, friendship, patience and love. My academic achievements have been much harder without her support.

Finally, to my parents and family, for their unconditional support and encouragement.

palavras-chave

edifícios existentes de betão armado, armadura lisa, escorregamento, ensaios de arrancamento, ensaios cíclicos, pilares, nós viga-pilar, modelação numérica.

resumo

Sismos recentes comprovam a elevada vulnerabilidade dos edifícios existentes de betão armado. A resposta das estruturas aos sismos é fortemente condicionada pelas características da aderência aço-betão, que exibe degradação das propriedades iniciais quando sujeitas a carregamentos cíclicos e alternados. Este fenómeno é ainda mais gravoso para elementos com armadura lisa, predominantes na maioria das estruturas construídas até à década de 70 nos países do sul da Europa. A prática corrente de conceção, dimensionamento e pormenorização das estruturas antigas leva a que tenham características de comportamento e níveis de segurança associados não compatíveis com as exigências atuais. Os estudos realizados sobre o comportamento cíclico de elementos estruturais de betão armado com armadura lisa são ainda insuficientes para a completa caracterização deste tipo de elementos.

Esta tese visou a caraterização da relação tensão de aderência versus escorregamento para elementos estruturais com armadura lisa e o estudo da resposta cíclica de pilares e nós viga-pilar de betão armado com armadura lisa.

Foram realizados dez séries de ensaios de arrancamento (nove monotónicos e um cíclico) em provetes com varões lisos. Os resultados destes ensaios permitiram propor novas expressões empíricas para a estimativa dos parâmetros usados num modelo disponível na literatura para representação da relação tensão de aderência versus escorregamento. É ainda proposto um novo modelo monotónico para a relação tensão de aderência versus escorregamento que representa melhor a resposta após a resistência máxima de aderência.

Uma campanha de ensaios unidirecionais em pilares e nós viga-pilar foi também realizada com o objetivo principal de caracterizar o comportamento cíclico deste tipo de elementos. No total foram realizados oito ensaios em pilares, sete ensaios em nós viga-pilar interiores e seis ensaios em nós viga-pilar exteriores representativos de estruturas antigas de betão armado com armadura lisa. Os resultados experimentais permitiram avaliar a influência do escorregamento e estudar o mecanismo de corte em nós e a evolução dos danos para elementos com armadura lisa. Com base nos resultados experimentais foi proposta uma adaptação na expressão do Eurocódigo 8-3 para o cálculo da capacidade última de rotação de elementos com armadura lisa.

Foi também desenvolvido um estudo paramétrico, com diferentes estratégias de modelação não linear, para a simulação da resposta de pilares considerando o escorregamento da armadura lisa. Por último, foi proposto um novo modelo simplificado trilinear para o aço que contempla o efeito do escorregamento da armadura lisa.

keywords

old reinforced concrete structures, plain reinfrocing bars, bond-slip, pull-out tests, cyclic tests, columns, beam-column joints, numerical modelling.

abstract

Recent earthquakes have shown the significant vulnerability of existing reinforced concrete buildings. The seismic response of structures is largely conditioned by the bond-slip properties that may experience an accelerated degradation under cyclic loading. The influence of this effect can be even larger for elements with plain reinforcing bars, as typically used in structures built before the 1970s in Southern European countries. The principles, design and practice adopted in the past do not guarantee that the existing reinforced concrete structures meet performance requirements recommended in modern codes. The available studies on the cyclic behaviour of reinforced concrete elements with plain reinforcing bars are still limited.

This thesis intended to contribute for the characterization of the bond-slip relationship for plain reinforcing bars and to study of the cyclic response of columns and beam-column joints reinforced with plain bars representative of existing building structures.

Ten sets of pull-out tests (nine monotonic and one cyclic) were performed on specimens built with plain bars, which allowed to propose new empirical expressions for some parameters adopted in bond-slip models available in the literature for plain bars. Also, a new monotonic bond-slip model was proposed better representing the post-peak strength bond-slip relationship.

An experimental campaign of unidirectional tests on full-scale columns and beam-column joints was carried out to characterize their cyclic response. In total eight columns, seven interior beam-column joints and six exterior beam-column joints were tested, representing old reinforced concrete building structures. The experimental results confirms the influence of the reinforcing bars' slippage and allowed to better understand the shear mechanism in the joints and damage evolution of elements with plain reinforcing bars. Based on the experimental results, it was proposed a modification to the Eurocode 8-3 expression used to calculate the ultimate rotation capacity of elements with plain reinforcing bars.

A comparative study of different strategies for the non-linear numerical modelling of columns taking into account the slippage was also developed. Finally, a new simplified tri-linear steel model was proposed that includes the effect of slippage of plain reinforcing bars.

TABLE OF CONTENTS

LIST OF FIGURES

CHAPTER 2 - Experimental study of bond-slip in RC structural elements with plain bars

CHAPTER 3 - Experimental cyclic behaviour of RC columns with plain bars

CHAPTER 4 - Cyclic behaviour of interior beam-column joints reinforced with plain bars

CHAPTER 5 - Cyclic tests on exterior beam-column joints non-seismically designed

CHAPTER 6 - Numerical modelling of RC columns and a new steel model for elements with plain bars

LIST OF TABLES

CHAPTER 2 - Experimental study of bond-slip in RC structural elements with plain bars

CHAPTER 3 - Experimental cyclic behaviour of RC columns with plain bars

CHAPTER 4 - Cyclic behaviour of interior beam-column joints reinforced with plain bars

CHAPTER 5 - Cyclic tests on exterior beam-column joints non-seismically designed

CHAPTER 6 - Numerical modelling of RC columns and a new steel model for elements with plain bars

CHAPTER 1

INTRODUCTION, OBJECTIVES AND ORGANIZATION OF THE THESIS

1.1 MOTIVATION AND INTRODUCTION

Natural disasters like earthquakes are responsible for large human and material losses. The earthquake damage level depends not only on the seismic magnitude, but also on the structural solution, materials properties, elements' detailing and soil properties. In the last decades many studies focused on the improvement of the buildings' seismic performance, particularly for reinforced concrete structures (RC). However, the seismic behaviour of old RC structures is still not completely understood and it is recognised the need for the assessment and strengthening of these structures.

The damage observed in the last earthquakes demonstrates the large vulnerability of RC structures, especially of the existing structures built with plain reinforcing bars. Moreover, a significant number of existing RC buildings are located in areas with high seismic activity and were built before the 1970s, prior to the enforcement of the current seismic design philosophies. Consequently, many of these structures are not provided of adequate ductility and specific detailing for seismic demands. These seismic performance limitations are even more significant when plain reinforcing bars are used, which is commonly found in old RC structures.

The cyclic loads induced by the earthquakes lead to progressive bond degradation, resulting in relative displacement (slippage) between the reinforcing bars and the surrounding concrete, which is frequently addressed as bond-slip. The bond-slip

mechanism is reported as one of the common causes of severe damage and even collapse of RC structures under seismic loading.

In the regions where demands are larger, such as beam-column joints and extremities of the columns, the bond-slip mechanism may have an important contribution to the lateral deformation of the elements and, as a consequence, condition the overall response of the structure. The bond-slip mechanism is caused by the force transfer between reinforcing bars and the surrounding concrete. If bar slippage occurs, the force transfer mechanism is affected and might lead to reduction in stiffness and dissipation energy capacity of the structure.

It is internationally recognised that bar slippage may influence the cyclic behaviour of the RC structures dramatically. However, bond-slip is typically neglected in the numerical analysis of RC structures. Moreover, the specifications of recent RC design codes were developed under the assumption of perfect bond between concrete and steel. As a consequence the seismic behaviour of RC structures built with plain reinforcing bars can be substantially different from theoretical predictions.

In the last years several experimental studies have investigated the cyclic behaviour of RC elements, but few focused on the behaviour of elements designed according to old RC codes. In particular, experimental data on the cyclic behaviour of RC elements with substandard details built with plain reinforcing bars is scarce in comparison with that available for elements with deformed bars. Consequently, the cyclic and post-elastic behaviour of elements with plain bars is still not well known.

The proper characterisation of the cyclic behaviour of RC elements is only possible based on extensive experimental data that covers a wide range of reinforcement detailing, typical geometrical characteristics, material mechanical properties and loading conditions. A broad experimental database representative of the existing structures is essential for the development of empirical and semi-empirical formulas and for the development of models that can be used to represent the cyclic behaviour of RC elements with plain bars. The experimental data is also crucial to calibrate and upgrade numerical models for the adequate simulation of the cyclic behaviour of this type of elements. Essentially, the available numerical models for simulating the bar slippage effects are limited to the

analysis of specific types of elements or too difficult to implement as a consequence of the limited experimental data available.

1.2 OBJECTIVES AND METHODOLOGY

The main objective of this PhD thesis is the characterisation of the effect of the bond-slip mechanism on the cyclic behaviour of RC elements representative of existing structures built with plain reinforcing bars. In particular, this research aimed to:

i) Identify, based on the literature review, the lacunas in terms of available experimental results and the knowledge limits regarding the cyclic behaviour of RC structural elements with plain reinforcing bars;

ii) Develop an experimental programme to study at local level the bond-slip relationship intending to develop an upgraded bond-slip model for plain reinforcing bars;

iii) Contribute to enlarge the existing experimental database on the cyclic behaviour of RC columns and beam-column joints with plain reinforcing bars, which can be used to develop empirical expressions and to calibrate numerical models that better simulate the cyclic behaviour of this type of structural elements;

iv) Contribute to the understanding of the cyclic behaviour of RC elements built with plain reinforcing bars by quantifying the influence of the bond-slip mechanism in different parameters and mechanisms of the structural response, such as: the bending and shear deformation contributions for the cyclic response of the elements, the energy dissipation capacity and the damage mechanisms;

v) Develop and calibrate numerical models that take into account the slippage of plain reinforcing bars;

vi) Compare the conclusions derived in this work with the main outputs from similar research available in the literature.

The strategy adopted to achieve these objectives can be summarised as follows:

i) Development of a literature review related to: the seismic vulnerability of existing RC structures designed and built until the 1970s; the old RC codes' specifications

for seismic safety; and, the available experimental data concerning the cyclic behaviour of RC elements built with plain reinforcing bars;

ii) Preparation and development of an extensive experimental campaign, including: pull-out tests, RC columns and beam-column joints (interior and exterior), detailed according to the old Portuguese RC codes and built with plain reinforcing bars;

iii) Proposal of empirical expressions for the bond-slip relationship model and proposal of improvement of Eurocode 8 formula for the ultimate rotation capacity, based on the experimental results on pull-out specimens and on the tests on full-scale RC elements built with plain reinforcing bars;

iv) Development and calibration of numerical non-linear models to simulate the experimental response of the tested column specimens, investigating the influence of the bond-slip mechanism. Also based on the experimental results and analytical correlations, a new simplified steel model taking into account the bond-slip mechanism is proposed.

1.3 ORGANISATION OF THE THESIS

This thesis has been structured into seven chapters. The main chapters of this thesis corresponds to work that has been published, or submitted, for publication in peer-reviewed journals. This first chapter presents the motivation and introduces the subjects addressed in the thesis. Chapter two reports the experimental results of pull-out tests and the proposed new empirical expressions for the bond-slip relationship between concrete and plain reinforcing bars. In chapters three, four and five are presented and discussed the experimental tests carried out on full-scale RC elements with plain reinforcing bars developed to characterise their cyclic behaviour. Chapter six presents the results of the numerical models developed to simulate the response of columns, considering the bar slippage effect. The last chapter discusses the main conclusions of this research and presents possible future directions of research on this subject. The contents of each chapter are described in further detail in the next paragraphs.

The second chapter presents the results of ten sets of pull-out tests (nine monotonic and one cyclic) performed on specimens built with plain bars. Based on the experimental results, upgraded empirical expressions are proposed for the parameters adopted in one of

the more recent bond-slip models for plain bars available in the literature. The new empirical expressions take into account the concrete compressive strength, rebar yield stress, embedded length and bar diameter. A new monotonic bond-slip model is also proposed, better representing the bond-slip relationship after the peak strength.

Chapter three describes the results of a testing campaign composed of unidirectional cyclic and monotonic tests performed on full-scale columns built with plain bars, without adequate reinforcement detailing for seismic demands. The influence of bond properties, cold joint at the column base, lapping of longitudinal reinforcing bars, amount of reinforcing steel, cross-section dimensions and of the imposed loading history is studied. A correction coefficient of the expressions of EC8-3 for the calculation of the ultimate rotation capacity of columns with plain reinforcing bars is also proposed in this chapter.

The fourth chapter reports the results of cyclic tests carried out on interior full-scale beam-column joints built with plain bars. These joint specimens are also representative of existing reinforced concrete structures, i.e. built without adequate reinforcement detailing for seismic demands. The specimens and the testing campaign were designed and detailed so as to allow the investigation of the influence of bond properties, lapping of the longitudinal bars in columns and beams, bent-up bars in the beams, slab contribution and concrete strength.

The fifth chapter addresses the cyclic and monotonic testing of full-scale RC exterior beam-column joints built with plain reinforcing bars. These specimens are also representative of RC structures built without adequate reinforcement detailing for seismic demands. For these elements, the influence of bond properties, lapping of the longitudinal bars, anchorage of the beam reinforcing bars and loading on the beam-column joints response are investigated.

Chapter six is devoted to the numerical modelling of the cyclic response of two RC columns, one built with deformed bars and the other with plain bars. For each column, different modelling strategies were adopted. The numerical models were built using the OpenSees and SeismoStruct platforms, and were calibrated with the experimental test results presented in Chapter 3. The bond-slip effects were included in the OpenSees models using a simple modelling strategy. A new simplified tri-linear steel material model

that considers slippage of the plain reinforcing bars in RC structural elements is also proposed.

Chapter seven summarises the main conclusions of the present work and outlines possible future research directions.

CHAPTER 2

EXPERIMENTAL STUDY OF BOND-SLIP IN RC STRUCTURAL ELEMENTS WITH PLAIN BARS

Melo, J., Rossetto, T., Varum, H. (in press) Experimental study of bond–slip in RC structural elements with plain bars. *Materials and Structures*. doi: http://dx.doi.org/10.1617/s11527-014-0320-9

2.1 ABSTRACT

A considerable number of reinforced concrete buildings in European countries were built before the 1970s according to rules and principles which are now obsolete, and using reinforcing bars with plain surface that do not guarantee proper bond properties. Most existing studies concerning the characterisation of the bond-slip relationship have been carried out on elements built with deformed reinforcing bars. The bond-slip relationship for plain bars is still not well known, and current empirical expressions are found not to take into account all the factors that influence bond-slip performance. This chapter presents the results of ten sets of pull-out tests (nine monotonic and one cyclic) performed on specimens built with hot-rolled plain bars. One additional set of specimens built with deformed bars was tested monotonically to highlight the difference, in terms of bond-slip relationship, between plain and deformed rebars. Based on the experimental results, new empirical expressions are proposed for the parameters adopted in one of the more recent bond-slip models for plain bars available in the literature. The new empirical expressions take into account the concrete compressive strength, rebar yield stress, embedded length and bar diameter, and are an improvement on existing expressions. Finally, a new

monotonic bond-slip model is proposed, which better represents the bond-slip relationship after the peak strength.

2.2 INTRODUCTION

It is recognised that the behaviour of reinforced concrete (RC) structures is conditioned by the bond-slip mechanism between concrete and steel. This mechanism may influence the performance of structures in terms of strength, deformation, ductility, energy dissipation capacity and, eventually, the type and distribution of damage under cyclic loads. For RC structures built before the 1970s, designed according to old codes and built with plain reinforcing bars, the influence of the bond-slip is particularly important. In these types of structures, the bond stress developed at the interface between the concrete and steel is insufficient to avoid the slippage of the bar, and consequently the deformations of the structure are largely increased. This phenomenon is discussed in recent studies carried out on RC elements built with plain bars [1-5].

This chapter aims to study the bond-slip relationship for RC elements built with plain bars and proposes a new bond-slip monotonic model based on experimental results. Empirical expressions are commonly used to estimate the maximum bond stress. With few exceptions (e.g. [6,7]) most of these empirical expressions take into account only the concrete strength neglecting other parameters that also influence the maximum bond stress. Hence, a new empirical expression is proposed to compute the maximum bond stress that considers not only the compressive concrete strength, but also the bar diameter, embedded length and yield stress of the rebar.

The chapter first presents the factors that affect the bond-slip relationship, and the bond-slip constitutive relationships available in the literature. Next the pull-out experiments carried out for this study are described: specimen details, material properties and test setup. Existing bond-slip relationships are compared with the experiments and found to justify the need for empirical equations and model. Finally, a new bond-slip model is proposed that better represents the experimental results obtained in this campaign than other models obtained by other authors.

2.3 PREVIOUS WORK ON BOND-SLIP

2.3.1 Factors affecting bond-slip

A limited number of studies are available in the literature on bond-slip mechanisms in structural elements with plain bars. Few expressions are also available for the parameters used in the definition of the constitutive bond-slip relationship. In contrast, for deformed reinforcing bars several theoretical models may be found for the interaction mechanisms between steel bars and surrounding concrete [8].

One of the first studies on bond-slip behaviour in RC was conducted by Abrams [9], who describes the results of more than one thousand tests carried out on beams and pull-out specimens with plain and deformed bars. In this testing campaign, different variables were studied, such as bar diameter, embedded length, concrete block dimensions, bar surface, age and concrete mix, anchoring ends and storage conditions. Abrams concluded that the bond between concrete and plain reinforcing bars is influenced in terms of resistance by two main components, adhesive and sliding resistance. Adhesive resistance takes place before the slippage starts and is responsible for about 60% of the maximum bond stress. This ratio does not vary much for a wide range of mixes, ages, bar sizes and conditions of storage. Sliding resistance starts when the relative movement between both materials begins. Another conclusion was that the maximum bond stress is developed for a slip value about 0.25mm (0.01in).

Stoker and Sozen [10] state that the bond-slip on plain reinforcing bars is provided by two mechanisms: i) a physical interlocking between the microscopic, rough steel surface and the surround concrete before the slip starts and ii) a frictional mechanism between two sliding contact surfaces after the original interlocks have sheared off. Stoker and Sozen [10] also state that the bond-slip may be represented by a curve idealized by three linear branches: one vertical to represent the initial interlocking mechanism between steel and concrete, followed by a descending transition linear branch, and one horizontal branch to represent the mechanism of sliding friction. The authors state that both mechanisms are related to the shear strength of concrete. For the interlocking phase, the strength is influenced by the roughness of the steel surface and is independent of the lateral stress. For the frictional phase, the bond strength is influenced by the lateral stress.

Recently, a few studies [7,11-14] have been published that report the results of pull-out tests on specimens with plain reinforcing bars, with the intention to better define the parameters influencing the constitutive bond-slip relationship. Feldman and Barlett [7,13] have carried out around 250 pull-out tests on specimens with plain round and square reinforcing bars. Based on their results they have suggested an empirical expression to compute the maximum bond stress, as a function of the concrete strength, and reinforcing bar section shape (round or square), roughness and diameter. Moreover, Feldman and Barlett [13] propose a simple adhesion-sliding bond model that provides the force distribution along the bar length as a function of the applied load for an idealized bond stress-slip relationship. Based on this model, the bond stresses can be evaluated analytically using the mechanics-based relationships provided between bond stress and slip, slip and bar force, and bar force and bond stress.

2.3.2 Review of bond-slip models

CEB-217 [15] and CEB-FIB [6] report an idealized bond-slip curve for hot rolled plain reinforcing bars, which is shown in Figure 2.1a. The model includes a non-linear initial branch given by expression (2.1) until s_{max} followed by a second constant branch. s_{max} is defined as the slip value corresponding to the maximum bond stress.

$$\tau_b = \tau_{b,\max} \cdot \left(\frac{s}{s_{\max}} \right)^{\alpha} \tag{2.1}$$

CEB-217 [15] and CEB-FIB [6] suggest that for plain hot rolled bars: s_{max} = 0.10mm (0.004in) and the empirical factor α = 0.5. A maximum bond stress ($\tau_{b,max}$) equal to $0.30 \cdot \sqrt{f_{ck}}$ is suggested for good bond conditions or $0.15 \cdot \sqrt{f_{ck}}$ for poor bond conditions, where f_{ck} is the characteristic cylindrical concrete compressive strength (in MPa).

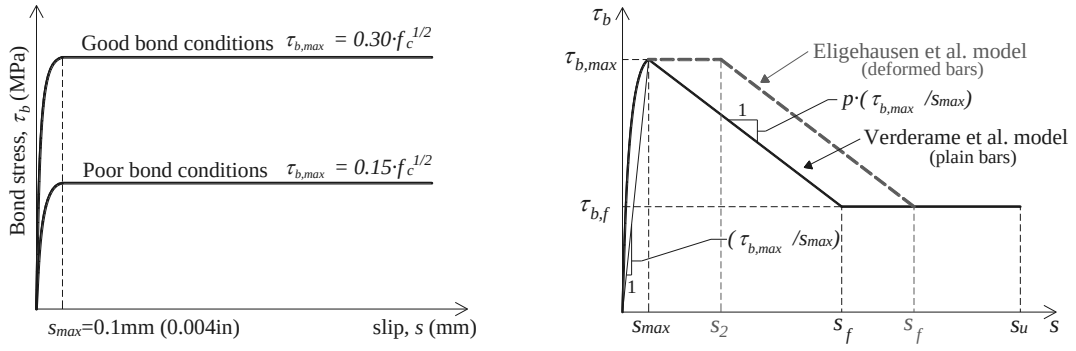

Figure 2.1 – Bond-slip relationship for hot rolled reinforcing bars adapted from: a) CEB-217 [15] and CEB-FIB [6] (plain bars); and b) Verderame et al. [11] (plain bars) and Eligehausen et al. [16] (deformed bars).

Verderame et al. [11,12] report the results of a series of monotonic and cyclic pull-out tests with plain round bars. Based on the experimental results, the authors suggest a modification on the bond-slip model proposed by Eligehausen et al. [16] for deformed bars. Basically, the proposed model is similar to the model proposed by Eligehausen et al. [16], but without the plateau (see Figure 2.1b). Verderame et al. [11] have also proposed a new model for the representation of the cyclic response of the steel-concrete interface for elements with plain reinforcing bars.

Based on their experimental results, Verderame et al. [11] proposed the following parameters for the model: $\tau_{b,\max} = 0.31 \cdot \sqrt{fc}$, s_{max}=0.23mm (0.0091in), α=0.26, $\tau_{b,f} = 0.43 \cdot \tau_{b,\max}$ and p=0.06, where $\tau_{b,max}$, s_{max} and α have the same meaning as in the CEB-217 [15] model. $\tau_{b,f}$ is the frictional bond stress, f_c is the cylindrical concrete compressive strength and p represents the slope of the softening branch expressed as a function of the secant stiffness ($\tau_{b,max}/s_{max}$). These mean values were obtained from results of pull-out tests carried out on specimens with 12mm (0.47in) reinforcing bar diameter, with an embedded length equal to 10 times the bar diameter and a mean concrete cylindrical strength equal to 15.9MPa (2.31ksi). In the later experimental campaign, the tests were done under displacement control. Table 2.1 summarises the main outcomes from several previous studies [7,9-13].

Table 2.1 – Resume of the main outcomes of previous experimental studies on bond-slip mechanism of plain reinforcing bars.

Reference	No. of tests	Type of tests	Output	Observations
Abrams [9]	804	Monotonic pull-out tests on round plain bars	$\tau_{b,\max} = 0.19 \cdot f_c$ $\tau_{b,f} = 0.50 \cdot \tau_{b,\max}$	$\tau_{b,max}$ is reached at s_{max} equals to 0.25mm (0.01in). $\tau_{b,max}$ is equal to about 19% of f_c. The frictional bond stress is approximately 50% of $\tau_{b,max}$. Small bar diameters give higher bond strength than the large bars during the early stages. The slippage begins at about 60% of $\tau_{b,max}$.
Stoker and Sozen [10]	26	Monotonic pull-out tests on round plain wires		$\tau_{b,max}$ increase approximately linearly with the bar diameter. The bond strength increase by approximately 10% per 6.9MPa (1Ksi) of concrete compressive strength.
Feldman and Barlett [7,13]	252	Monotonic pull-out tests on round and square 16mm (0.63in) and 32mm (1.26in) plain bars	For 16mm round plain bars: $\frac{\tau_{b,\max}}{\sqrt{f_c}} = \begin{pmatrix} 0.19 \cdot \sqrt{R_y} \\ -2.7\times10^{-5} \cdot R_y \cdot l_{emb} \end{pmatrix}$ $\frac{\tau_{b,f}}{\sqrt{f_c}} = \begin{pmatrix} 0.042 \cdot \sqrt{R_y} \\ -1.65\times10^{-5} \cdot R_y \cdot l_{emb} \end{pmatrix}$ For 32mm round plain bars: $\frac{\tau_{b,\max}}{\sqrt{f_c}} = \begin{pmatrix} 0.12 \cdot \sqrt{R_y} \\ +1.3\times10^{-5} \cdot R_y \cdot l_{emb} \end{pmatrix}$ $\frac{\tau_{b,f}}{\sqrt{f_c}} = \begin{pmatrix} 0.051 \cdot \sqrt{R_y} \\ -1.65\times10^{-5} \cdot R_y \cdot l_{emb} \end{pmatrix}$ Empirical bond-slip relationship: $\tau_b = \frac{1}{3}\begin{bmatrix} 2 \cdot \tau_{b,f} + \tau_{b,\max} \\ +\left(\tau_{b,f} - \tau_{b,\max}\right) \cdot \log(s) \end{bmatrix}$	$\tau_{b,max}$ and $\tau_{b,f}$ are proportional to the $\sqrt{fc}$ for the same group of bars. When the surface roughness increases, maximum bond stress and the associate slip increase. $\tau_{b,max}$ tend to decrease when the bar diameter increase. The bond-slip relationship is non-linear. Mechanics based relationships show that bond stress is a function of relative bar slip, slip is a function of bar force, and bar force is a function of bond stress.
Verderame et al. [11,12]	11	Monotonic and cyclic pull-out tests on 12mm (0.47in) round plain bars	For 12mm round plain bars: $\tau_{b,\max} = 0.31 \cdot \sqrt{f_c}$ $\tau_{b,f} = 0.43 \cdot \tau_{b,\max}$	The maximum bond is proportional to $\sqrt{fc}$. The frictional bond stress corresponds to 43% of the maximum bond. The bond-slip relationship is given as show in Figure 2.1b.

Notes: R_y is the surface roughness; l_{emb} is the embedded length; τ_b is the bond stress; and s is the slip.

2.3.3 A critical gap

From the studies presented in the previous sections and summarised in Table 2.1, it is clear that bond performance is affected by concrete compressive strength, bar diameter, embedded length, surface roughness, storage conditions and lateral stress parameters. However, only concrete compressive strength is included in almost all the models present

in Section 2.3.2. Moreover, most models consider linear branches after peak strength bond, which do not reflect the shape obtained experimentally. The empirical bond-slip relationship proposed by Feldman and Barlett [7] take into account other factors besides compressive concrete strength. Their empirical relationships are based on 16mm (0.63in) and 32mm (1.26in) bar diameters and show a dependence of bond on bar diameter. However, these particular bars diameters are not very representative of the bar diameters used in the construction of most existing RC buildings in the Mediterranean area, which tend to be smaller [17-19]. Therefore, there appears to be a need for a new empirical bond-slip model for plain bars that includes more of the parameters that influence bond-slip and better represent its behaviour after peak bond strength.

This chapter presents the approach followed to develop this new bond-slip model. Firstly, the experimental campaign of pull-out tests used to generate the empirical data for the new model is presented. Secondly, the experimental results are compared with existing bond-slip relationships (Verderame et al. [11] and by CEB-217 [15]). Finally, a new bond-slip model is proposed in the present chapter that adopts the Verderame et al. [11] shape up to peak but better characterises the descending branch of the bond-slip model. This new empirical model is derived based on the results of 27 experiments. This work has the potential to change how bond-slip is modelled in structural analyses and highlights the need for further experimental work to further refine the model.

2.4 EXPERIMENTAL CAMPAIGN, MATERIALS CHARACTERISATION AND TESTING SETUP

An experimental campaign on pull-out tests was carried out in the Department of Civil Engineering at University of Aveiro with the aim of study the bar diameter, embedded length and yield bar stress on bond-slip performance. The campaign consisted of a series of monotonic and cyclic pull-out tests carried out on specimens built with plain bars in order to characterize the bond-slip relationship in old RC structures.

Table 2.2 summarises the nomenclature adopted for the specimens, the details and bar diameter (ϕ) for each test. For each bar diameter and specimen type (EN, WP and SP) studied, a set of three specimens where built. Two additional sets of three EN specimens with 12mm (0.47in) bar diameter were also built. One of these sets was built with deformed bars (labelled as EN-12D) and was tested monotonically, for comparison with

the results for the specimens with plain bars. The other set was built with plain bars, and was used for cyclic pull-out tests (labelled as EN-C12). Hence, in total 33 specimens were tested, 30 under monotonic pull-out and 3 under cyclic pull-out.

The specimens labelled as EN follow the specifications of the standard EN 10080 [20], which define the details and specimen dimensions for pull-out tests. Therefore, in these specimens the embedded length is equal to 5 times the bar diameter (5 ϕ), and the cross-section dimensions of the concrete block are 0.20m × 0.20m (7.94in × 7.94in). To guarantee the bond between concrete and steel for the length specified in the standard, a plastic tube with 0.20m length (7.94in) was used to isolate the bar from the surrounding concrete in the upper part of the concrete block. The cross-section dimensions of specimens WP and SP are 0.25m × 0.25m (9.93in × 9.93in) and the embedded length is equal to 30 ϕ and 45 ϕ, respectively. The embedded length of specimens SP is the length recommended for full straight anchorage of plain bars according to CEB-217 [15]. The embedded length of specimens WP was defined based on the recommendations included in the first Portuguese codes [21,22], but adopting a straight shape, i.e. without hook. All specimens were cast in the horizontal position as specified in EN 10080 [20].

Table 2.2 – Specimens.

	EN	**WP**	**SP**
Specimen type	Detailed according to EN 10080 [20]	Straight anchorage with the embedded length suggested in codes [21,22] but without hook	Full straight anchorage according to CEB-217 [15]
Detailing (dimensions in meters, 1m=39.7in)	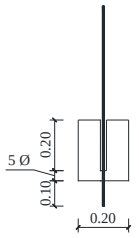	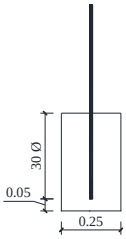	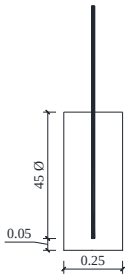
Bar diameter, mm (in)	10, 12 and 16 (0.40, 0.47 and 0.64)	10, 12 and 16 (0.40, 0.47 and 0.64)	10, 12 and 16 (0.40, 0.47 and 0.64)

The mean values of the mechanical properties of concrete and steel reinforcement are presented in Table 2.3. Cylinder samples of concrete with dimensions ϕ150mm×300mm (ϕ 5.9in×11.8in) were used for determining the compressive strength. The concrete samples were tested simultaneously with the pull-out tests, and after 90 days of concrete

curing. The grades of the hot-rolled plain and deformed reinforcing bars used in the specimens were A235 and A400NRSD, respectively. For each bar diameter, tensile tests were performed on three specimens according to the standard EN ISO 6892-1 [23]. The mean static values of yield and ultimate stress and young's modulus for each series of steel specimens are presented in Table 2.3.

Table 2.3 – Mean values of the material mechanical properties.

Concrete		**Steel**			
f_{cm}**, MPa (ksi)**	**Grade**	**Bar diameter, mm (in)**	f_{ym}**, MPa (ksi)**	f_{um}**, MPa (ksi)**	E_{ym}**, GPa (ksi)**
15.8 (2.3)	A235 (plain)	10 (0.39)	427 (62)	501 (73)	201 (29152)
		12 (0.47)	405 (59)	470 (68)	199 (28863)
		16 (0.63)	525 (76)	581 (84)	200 (29008)
	A400NRSD (deformed)	12 (0.47)	465 (67)	585 (85)	199 (28863)

The pull-out tests were performed with the setup shown in Figure 2.2. A reaction steel frame supports, in the upper part, the servo-actuator connected to load-cell and to the grip, and at the base a mechanism was installed to fix the specimen. For the tests of specimens EN, the bar slippage was measured with a linear variable differential transformer (LVDT) installed under the concrete block (Figure 2.2c), while for the other specimens the LVDT was mounted at the upper face of the concrete block. The relative displacement measured with the LVDT in the testing setup adopted for specimens WP and SP includes the elongation of the steel bar. To discount this elongation, an extensometer was installed at the bar. The elongation of the bar inside the concrete block of specimens EN was a maximum of 3% of the s_{max} value. Therefore, measuring of displacements at the loaded end (specimens WP and SP) or at the unloaded end (specimens EN) are approximately the same.

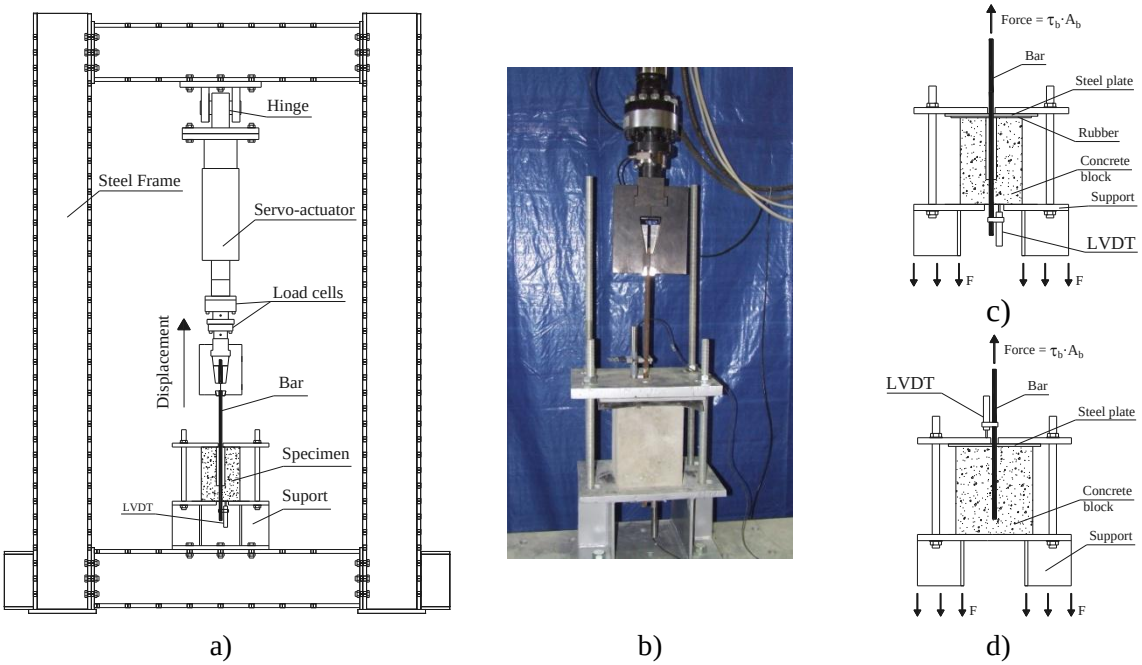

Figure 2.2 – Testing setup: a) schematics; b) general view; fixing elements and monitoring details for specimens c) EN and d) WP and SP.

The monotonic pull-out tests were carried out under force controlled conditions, with a load ratio velocity (v_p) of $v_p = 0.56 \cdot \phi^2$ (N/s), as specified in CEN EN 10080 [20], where ϕ is the nominal bar diameter in mm. The cyclic tests were performed under displacement controlled conditions, with a velocity equal to 0.1mm/sec (0.004in/sec).

2.5 RESULTS AND COMPARISON WITH AVAILABLE MODELS

2.5.1 Monotonic tests

The experimental campaign carried out has contributed to improve knowledge on the monotonic constitutive bond-slip relationship of RC elements with plain reinforcing bars. The interaction between concrete and reinforcing steel bars is usually described by the relationship between bond stress and slip. For the analysis of the experimental results, as has been commonly adopted in previous works (namely in CEB-217 [15] and CEB-FIP [6]), the bond stress was computed considering a constant bond stress distribution along the embedded bar length. Hence, the bond stress τ_b is calculated according to equation (2), where F is the tensile force measured during the test, ϕ is the bar diameter and l_{emb} is the embedded bar length. In this work it is assumes that s_{max} occurs close to the interface between the steel bar and concrete block, as commonly adopted in the literature, CEB-FIP [8].

$$\tau_b = \frac{F}{\phi \cdot \pi \cdot l_{emb}} \tag{2.2}$$

For each testing set, the average curve of the three individual bond-slip curves for each tested specimen was derived. The average curves are compared with the bond-slip relationships proposed by Verderame et al. [11] and by CEB-217 [15], as shown in Figure 2.3 to Figure 2.5, for specimens EN, WP and SP, respectively. The results are represented up to a slip equal to 10mm (0.39in), since after this point the bond-slip relationship becomes approximately constant. Splitting failure were not observed in the tests.

For the comparison with Verderame et al. [11] the mean values of parameters defined in their work were used. For the CEB-217 [15] model, good bond conditions and plain hot rolled bars were considered, resulting in $\tau_{b,\max} = 0.3\sqrt{fc}$, $s_{\max} = 0.1mm(0.004in)$ and $\alpha = 0.5$.

Figure 2.3 also shows the average curve of the specimens built with deformed bars, as well as the CEB-217 [15] law based on the model for deformed bars considering good bond conditions and hot rolled bars. The tests show that the maximum bond stress obtained was approximately 6.6 times larger than the maximum bond stress achieved on the specimens with plain reinforcing bars.

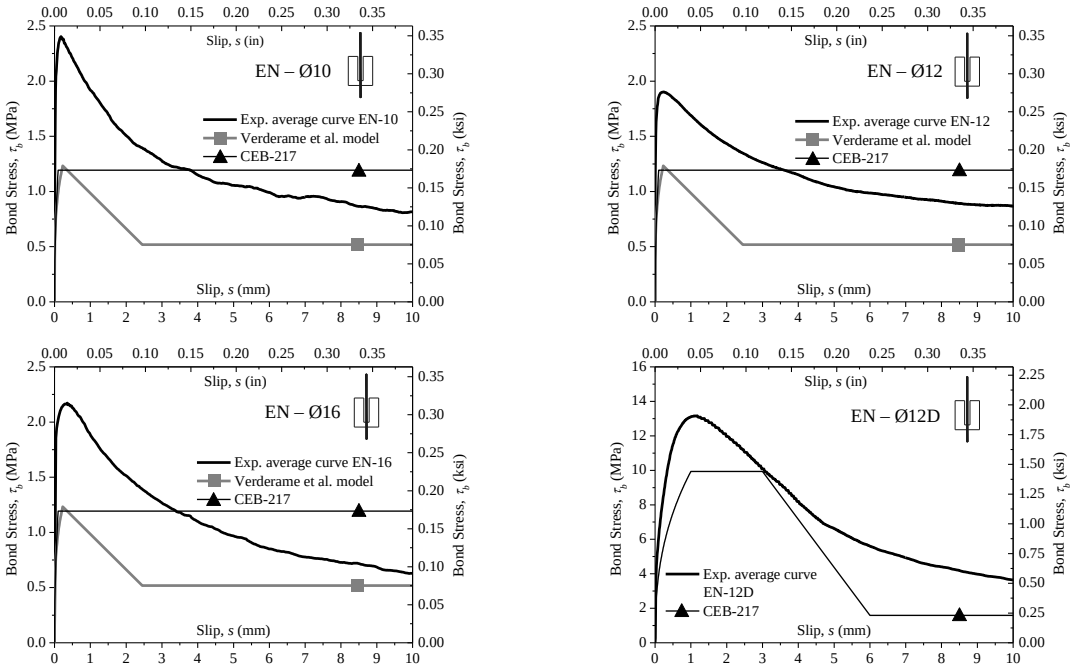

Figure 2.3 – Comparison between experimental results and existing curves for specimens EN.

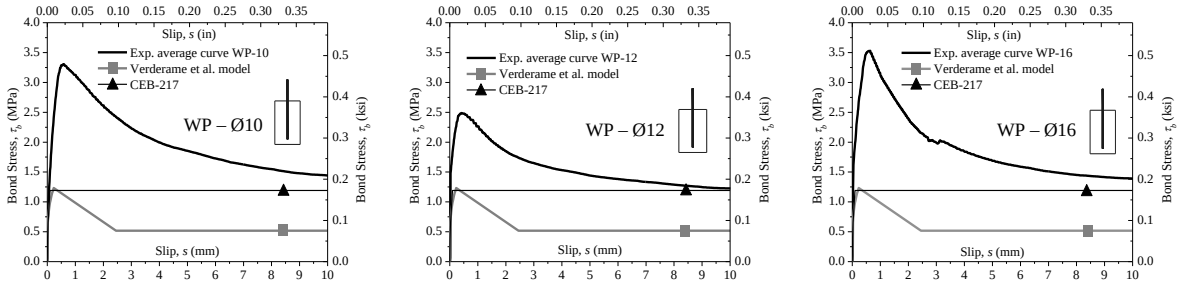

Figure 2.4 – Comparison between experimental results and existing curves for specimens WP.

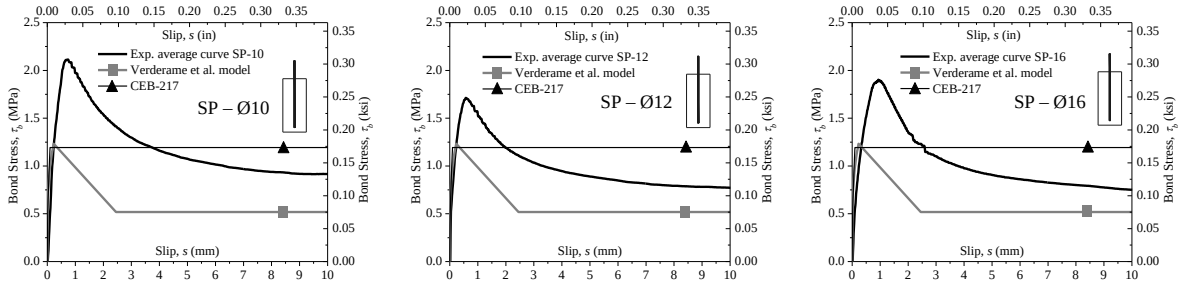

Figure 2.5 – Comparison between experimental results and existing curves for specimens SP.

From Figure 2.3 to Figure 2.5 it is evident that the model proposed by Verderame et al. [11] with three branches tends to better represent the experimental results than the CEB-217 model. But for deformed bars (set EN-12D) the CEB-217 [15] model represents better the experimental bond-slip relationship than for the other sets with plain bars.

The differences in terms of maximum bond stress and softening effect (bond degradation) found between the experimental results and the two considered models can be justified by several factors that are not taken into account by the models, such as: i) bar diameter [7,9,13]; ii) embedded length [9]; iii) surface roughness [7,9,13]; iv) storage conditions [9]; or v) lateral stress [10]. Another aspect that may justify the differences observed is the loading conditions, since the tests performed in this work were force controlled, as recommended in EN 10080 [20], while the model proposed by Verderame et al. [11] is based on pull-out tests performed under displacement control.

2.5.2 Cyclic tests

Figure 2.6 shows the results of the cyclic tests performed (EN-C12-i), as well as the average curve of the monotonic tests on similar specimens (EN-12). Figure 2.6 presents also the cyclic model proposed by Verderame et al. [11], considering $\tau_{b,\max} = 0.31\sqrt{fc}$, $\tau_{b,f} = 0.13\sqrt{fc}$, $\tau_{b,r} = 0.09\sqrt{fc}$, $\tau_{b,c} = 0.05\sqrt{fc}$, $s_{\max} = 0.23mm\,(0.009in)$, α=0.26 and

p=0.06, where $\tau_{b,r}$ is the residual bond stress and $\tau_{b,c}$ is the cyclic bond resistance. In one test a problem with the control system occurred and so the results of this test are here disregarded. The experimental results indicate that after reaching the maximum capacity in one loading direction the capacity in the opposite direction may not be limited to the residual value, but can be larger. This fact is in agreement with the experimental observations obtained by other authors in cyclic tests (Verderame et al. [11]). The cyclic model proposed by Verderame et al. [11] underestimates the bond stress, principally for the first cycles with small slippage values. Due to the lower number of cyclic tests performed in this study, is not possible to suggest improvements to Verderame et al. [11]. Future work should develop an extensive experimental campaign of cyclic pull-out tests in order to propose a new model based on the cyclic model of Verderame et al. [11].

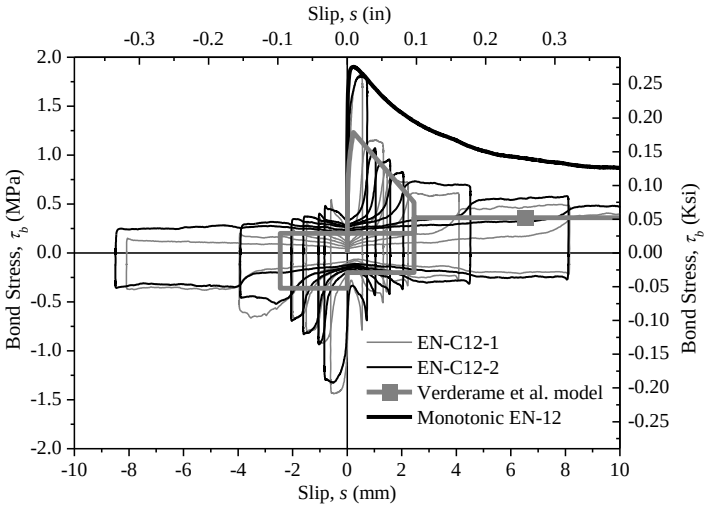

Figure 2.6 – Cyclic test results (EN-C12) and comparison with results of monotonic tests and empirical model.

Another aspect investigated in this comparison is the bond stress degradation for cyclic loading with increasing amplitude. Even if the number of tests performed is limited, results evidence the reduction of the bond capacity after maximum stress is reached but this is seen not tend immediately to the residual value. It was also observed that the maximum bond capacity for both, monotonic and cyclic tests, are similar.

2.5.3 Summary of main results

The mean values of the main properties of the bond-slip response ($\tau_{b,max}$, s_{max}, $\tau_{b,f}$) obtained in the tests (monotonic and cyclic) are summarised in Table 2.4. This table also includes the values of the parameters α and p computed according to the methodology presented in

Verderame et al. [11], in order to best-fit the experimental results, i.e., for each branch of the curve, equilibrating the area underneath the experimental and the empirical curves. The mean values and the coefficient of variation (CoV) presented in Table 2.4 correspond to the statistical measures of the specimens with plain bars. The variability found for the main properties of the bond-slip results is considerable, as indicated by the coefficients of variation. So, this conclusion confirms the influence of the studied variables (bar diameter, embedded length and reinforcement yield stress) in the bond properties, enforcing the need to include these variables in the empirical expressions for the estimation of the bond-slip laws.

Table 2.4 – Mean values of the parameters defining the bond-slip relationship.

Specimen type	Bar diameter, mm (in)	$\tau_{b,max}$, MPa (ksi)	s_{max}, mm (in)	$\tau_{b,f}$, MPa (ksi)	α	p
EN	10 (0.39)	2.4 (0.35)	0.18 (0.01)	0.80 (0.12)	0.14	0.025
	12 (0.47)	1.9 (0.28)	0.25 (0.01)	0.87 (0.13)	0.07	0.026
	16 (0.63)	2.2 (0.32)	0.35 (0.01)	0.63 (0.09)	0.06	0.044
EN-12D (deformed bar)	12 (0.47)	12.5 (1.81)	0.70-1.70 (0.03-0.07)	3.65 (0.53)	0.35	0.137
EN-C12 (cyclic test)	12 (0.47)	1.7 (0.24)	0.49 (0.02)	0.36 (0.05)	0.22	-
WP	10 (0.39)	3.3 (0.48)	0.60 (0.02)	1.44 (0.21)	0.33	0.063
	12 (0.47)	2.5 (0.36)	0.43 (0.02)	1.23 (0.18)	0.21	0.045
	16 (0.63)	3.5 (0.51)	0.64 (0.03)	1.39 (0.20)	0.27	0.097
SP	10 (0.39)	2.1 (0.31)	0.71 (0.03)	0.90 (0.13)	0.51	0.098
	12 (0.47)	1.7 (0.25)	0.57 (0.02)	0.77 (0.11)	0.41	0.080
	16 (0.63)	1.9 (0.28)	0.93 (0.04)	0.75 (0.11)	0.44	0.146
Mean (without EN-12D)		2.3 (0.33)	0.51 (0.02)	0.92 (0.13)	0.27	0.069
CoV (without EN-12D)		0.28	0.44	0.37	0.58	0.57

2.6 IMPROVED CONSTITUTIVE MODEL FOR THE BOND-SLIP RELATIONSHIP AND EMPIRICAL EXPRESSIONS FOR THE PARAMETERS INVOLVED

2.6.1 Fundamentals and formulation of the proposed model and empirical expressions

As discussed in Section 2.4, and supported by different authors, the bond-slip response is dependent on the compressive concrete strength, surface roughness and diameter of the bars [7,9,11-13], among other parameters. However, in the two models presented and discussed in Section 2.5 the maximum bond stress is estimated only from the compressive

concrete strength, with the parameters s_{max}, α and p being empirical constants. This makes the models highly specific to the test data that has been used to derive them, and arguably not extendible to applications outside the assumptions of their derivation data.

In Figure 2.3 to Figure 2.5, it is clear that the use of a non-linear function instead of the second and third branches of the Verderame et al. [11] model could better represent the bond response. In this section a new bond-slip model is proposed that is an extension and modification of the formulation presented in Verderame et al. [11], and which includes multiple parameters that affect the bond-slip and adopts a non-linear descending branch. In this work, when the new empirical expressions are used to obtain the model parameters, the Verderame et al. model [11] is called Verderame et al. modified model. The Verderame et al. modified model and the new bond-slip model are shown in Figure 2.7a,b, respectively. In both models the ascending branch is defined by expression (2.1), where α is computed in order that the area underneath ($A_{1,mod}$) of the bond-slip curve until s_{max} equals the corresponding area from experimental results. Such as explained in Section 2.4, the Verderame et al. modified model for slip values larger than s_{max} is defined by two linear branches, a softening branch (from s_{max} to s_f) followed by a plateau until the ultimate slip (s_u). In the new model, after s_{max}, the bond-slip relationship is defined by a third-degree polynomial function until the ultimate slip, s_u, and is followed by a plateau. A value of 10mm (0.39in) is assumed for s_u which is based on experimental observations made by others [7] and these presented in Section 2.3. The descending polynomial branch is computed taking in account four assumptions: i) the bond-slip curve is continuous at the point ($\tau_{b,max}$, s_{max}); ii) the curve must cross the point ($\tau_{b,f}$, s_u); iii) horizontal tangent at the point ($\tau_{b,f}$, s_u); iv) the area underneath the bond-slip curve between s_{max} and s_u ($A_{2,mod}$) is equal to the given by the respective experimental results.

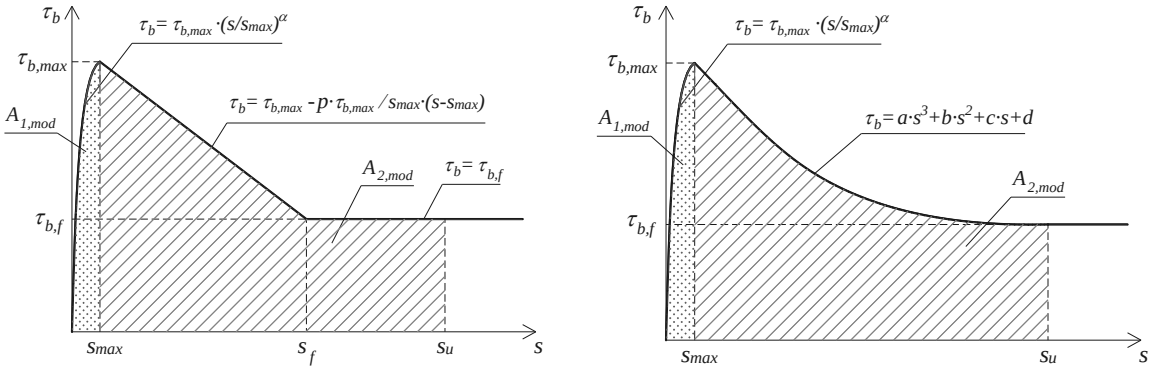

a) b)

Figure 2.7 – Bond-slip models: a) Verderame et al. modified model; b) proposed model.

The ascending branch of both models represents the contribution of chemical adhesion, mechanical micro-interlocking and friction to the bond strength. After the peak, the softening branch characterizes the progressive friction degradation without chemical adhesion or mechanical micro-interlocking. Finally, the horizontal branch characterizes the frictional residual bond strength.

Based on the experimental results, new expressions to compute the parameters of the modified Verderame et al. modified model are proposed, namely: $\tau_{b,max}$, $\tau_{b,f}$, α, s_{max}, p and s_f; where s_f is the slip value corresponding to the intersection between the softening branch and the plateau. The expressions proposed in this work (2.3-2.9) take into account material properties and geometrical characteristics, such as: cylindrical compressive concrete strength; yield stress of the reinforcing bars; embedded length; and, bar diameter. In this work was specifically chosen not include roughness as a parameter in the equations as it would not be possible to measure surface roughness in existing structures. It would reduce the practical usefulness of the equations. The empirical expressions (2.3-2.8) were obtained based on statistical analysis of all individual experimental results presented in previous section. For the determination of the empirical expressions, several relationships were tested based on the material and geometrical characteristics, and the one that best-fit the experimental results was chosen. The coefficient of determination (R^2) and root mean square error (RMSE) are used as first selection criteria. Based on a short list selected with the first criteria, the best-fit curve was chosen based on the Akaike's Information Criterion (AIC). This criterion is based on theory information and it combines maximum likelihood theory, information theory and the concept of the information entropy [24]. Figure 2.8

shows the empirical relationships chosen for each model parameter, corresponding coefficient of determination and root mean square error.

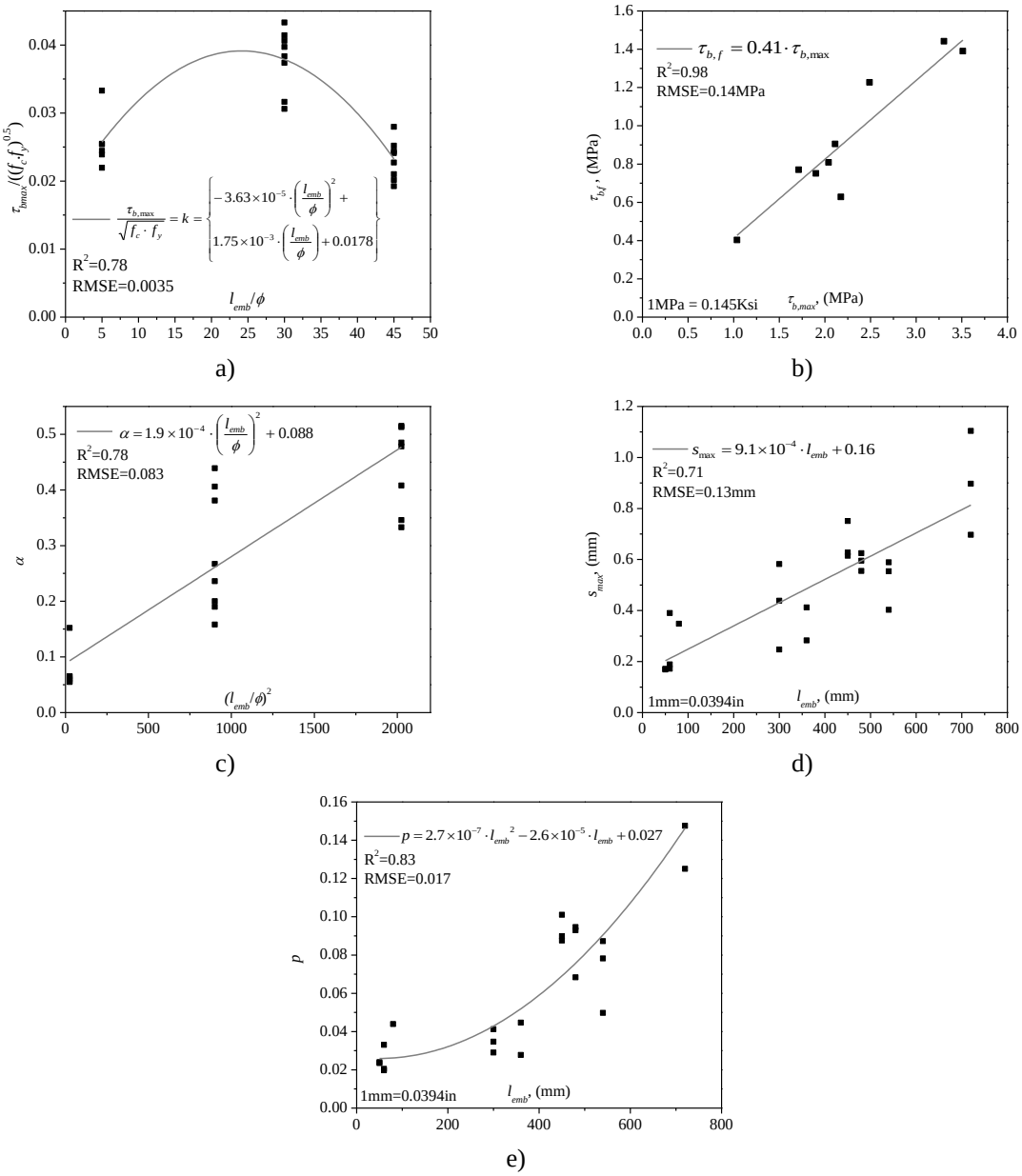

Figure 2.8 – Relationship between the model parameters and the material properties and geometrical characteristics: a) $\tau_{b,max}$; b) $\tau_{b,f}$; c) α; d) s_{max}; and e) p.

In practice, properties used in the expressions are normally known, which allows for the adoption of the suggested expressions in the definition of the model parameters. The proposed expressions were derived for RC elements with concrete strength between grades C12/15 and C16/20, according to EC2 [25] classification, and with hot rolled plain reinforcing bars with diameters between 10mm (0.39in) and 16mm (0.63in).

$$\tau_{b,\max} = k \cdot \sqrt{f_c \cdot f_y} \tag{2.3}$$

$$k = -3.63\times10^{-5} \cdot \left(\frac{l_{emb}}{\phi}\right)^2 + 1.75\times10^{-3} \cdot \left(\frac{l_{emb}}{\phi}\right) + 0.0178 \tag{2.4}$$

$$\tau_{b,f} = 0.41 \cdot \tau_{b,\max} \tag{2.5}$$

$$\alpha = 1.9\times10^{-4} \cdot \left(\frac{l_{emb}}{\phi}\right)^2 + 0.088 \tag{2.6}$$

$$s_{\max} = 9.1\times10^{-4} \cdot l_{emb} + 0.16 \tag{2.7}$$

$$p = 2.7\times10^{-7} \cdot {l_{emb}}^2 - 2.6\times10^{-5} \cdot l_{emb} + 0.027 \tag{2.8}$$

$$s_f = \frac{s_{max} \cdot \left(\tau_{b,max} + p \cdot \tau_{b,max} - \tau_{b,f}\right)}{p \cdot \tau_{b,max}} \tag{2.9}$$

The maximum bond stress is computed with expression (2.3), which depends on the constant *k*, the compressive concrete strength and yield stress of the reinforcing bar. The constant *k* takes into account the ratio between the embedded length and the bar diameter (expression 2.4). The yield stress of the reinforcing bar may influence the maximum bond stress, since the fitted results better represent the experimental values when the yield stress is taken into account. The frictional bond stress $\tau_{b,f}$ corresponds to 41% of the maximum bond (expression 2.5), which is similar to the value proposed by Verderame et al. [11] (43%). The parameter α is computed according to expression (2.6) and it depends on the ratio between the embedded length and the bar diameter. The slip corresponding to the maximum bond stress (s_{max}) is computed with expression (2.7) and takes into account the embedded length. The softening slope *p* of the Verderame et al. modified model is computed with expression (2.8) and it depends on the embedded length. The analytical expression (2.9) allows the computation of the slip value s_f.

The third-degree polynomial branch of the new proposed model is defined as presented in expression (2.10), where the constants *a*, *b*, *c*, *d* are calculated with expressions (2.11-2.14), respectively. The polynomial constants are affected by the area ($A_{2,mod}$) underneath the bond-slip curve between s_{max} and s_u, and it is computed with the empirical expression (2.15) depending on the maximum bond stress computed according to

expressions (2.3) and (2.4). (2.15) was found by fitting a curve to the relationship between the experimental area underneath the bond-slip curve between s_{max} and s_u, and the experimental $\tau_{b,max}$ obtained in all specimens.

$$\tau_b = a \cdot s^3 + b \cdot s^2 + c \cdot s + d \tag{2.10}$$

$$a = \frac{4 \cdot \left(3 \cdot A_{2,\mathrm{mod}} + \left(s_{\max} - 10\right) \cdot \left(\tau_{b,\max} + 2 \cdot \tau_{b,f}\right)\right)}{\left(s_{\max} - 10\right)^4} \tag{2.11}$$

$$b = \frac{-3 \cdot \left(4 \cdot A_{2,\mathrm{mod}} \cdot \left(20 + s_{\max}\right) + \left(s_{\max} - 10\right) \cdot \left(\left(30 + s_{\max}\right) \cdot \tau_{b,\max} + \left(50 + 3 \cdot s_{\max}\right) \cdot \tau_{b,f}\right)\right)}{\left(s_{\max} - 10\right)^4} \tag{2.12}$$

$$c = \frac{60 \cdot \left(4 \cdot A_{2,\mathrm{mod}} \cdot \left(5 + s_{\max}\right) + \left(s_{\max} - 10\right) \cdot \left(\left(10 + s_{\max}\right) \cdot \tau_{b,\max} + \left(10 + 3 \cdot s_{\max}\right) \cdot \tau_{b,f}\right)\right)}{\left(s_{\max} - 10\right)^4} \tag{2.13}$$

$$d = \left(s_{\max} - 10\right)^{-4} \cdot \left[\begin{array}{r} \left(-100 \cdot \left(10 + 3 \cdot s_{\max}\right) \cdot \tau_{b,\max} + s_{\max}\left(s_{\max}{}^2 - 30 \cdot s_{\max} - 600\right) \cdot \tau_{b,f}\right) \cdot \\ \cdot \left(s_{\max} - 10\right) - 1200 \cdot A_{2,\mathrm{mod}} \cdot s_{\max} \end{array}\right] \tag{2.14}$$

$$A_{2,\mathrm{mod}} = 5.1 \cdot \tau_{b,\max} + 0.51 \tag{2.15}$$

2.6.2 Comparison of the model predictions with the experimental results

The new expressions suggested in the section 2.6.1 were used to compute the parameters for both models, i.e. Verderame et al. modified model and our new proposal. In Figure 2.9 to Figure 2.11 are represented, for each test set, the obtained constitutive bond-slip relationships simultaneously with the experimental average curve. Comparing the experimental results with the predictions from the models, in generic terms, it is observed that both models approximate well the experimental results. However, the shape of the softening branch obtained with the new proposed model matches the experimental results much better than for the Verderame et al. modified model.

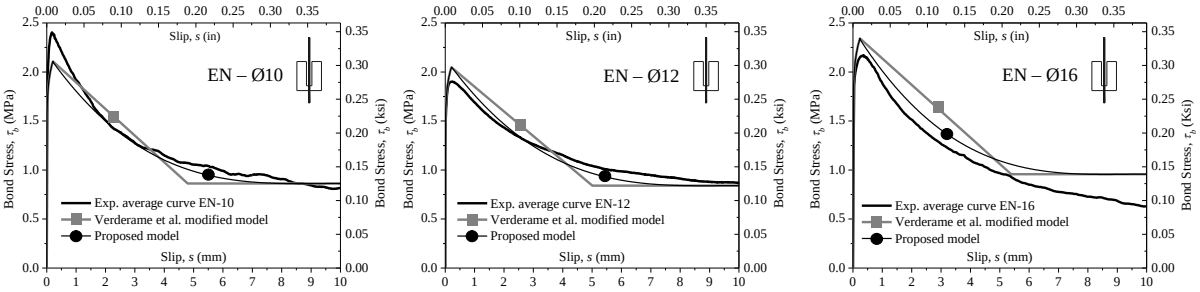

Figure 2.9 – Comparison between experimental results and model predictions for specimens EN.

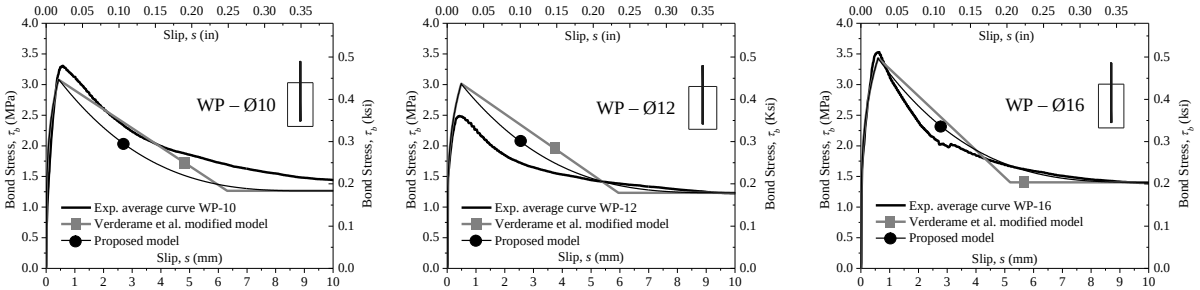

Figure 2.10 – Comparison between experimental results and model predictions for specimens WP.

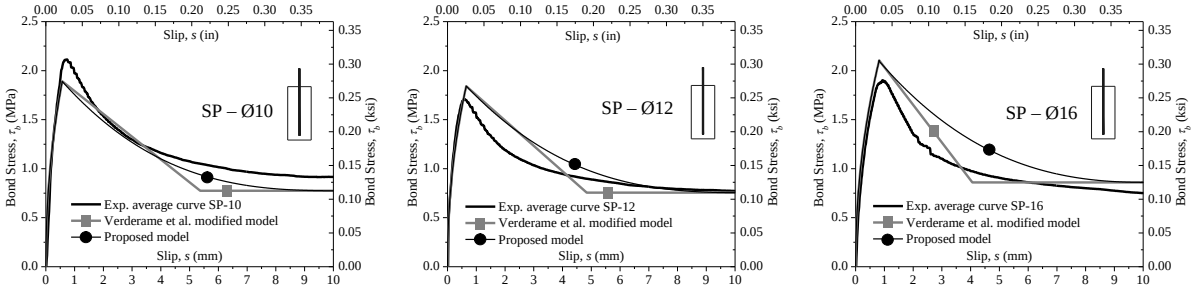

Figure 2.11 – Comparison between experimental results and model predictions for specimens SP.

Table 2.5 shows the mean values and the coefficients of variation of the error in the estimates of the Verderame et al. modified model and new model parameters. The error is calculated as the ratio between each parameter estimated (for the nine specimen sets) and the average experimental results for each test set. The maximum mean error is 2%.

The Verderame et al. modified model and the new model were derived from the same experimental results, and several model parameters are the same in both models. To verify which model might better represent the experimental results, the ratio between the area beneath each model curve up to a slip value of 10mm (0.39in) and the corresponding experimental area was calculated as an evaluation criteria. The average area ratio of Verderame et al. modified model is 1.02 and in the proposed model is 1.01. In both models the CoV is 0.10. Therefore, the proposed model provides a value of the area beneath the curve that is closer to the respective area beneath the experimental curves than the

Verderame et al. modified model, but the difference between both ratios is not significant (0.01). However, the new proposed model appears to better characterise the bond-slip behaviour after peak bond strength.

Table 2.5 – Errors (ratio model/experimental) of the both models parameters estimative.

	Verderame et al. modified model	**New model**				
	p_{mod}/p_{exp}	$\tau_{b,max,mod}/\tau_{b,max,exp}$	$\tau_{bf,mod}/\tau_{bf,exp}$	$s_{max,mod}/s_{max,exp}$	$\alpha_{mod}/\alpha_{exp}$	$A_{2,mod}/A_{2,exp}$
Mean	1.01	0.99	0.99	0.99	1.02	1.00
CoV	0.27	0.12	0.24	0.30	0.35	0.17

2.7 CONCLUSIONS

Two models available in the literature were compared with the obtained experimental results. Both models did not adequately represent the experimental average curves, in terms of maximum and frictional bond stress, typically underestimating these strengths. Based on new experimental results obtained, new empirical expressions were proposed to compute the values of the parameters for the Verderame et al. modified model. Also, a new constitutive bond-slip relationship was proposed in order to improve the characterisation of bond-slip after peak bond strength. The new empirical expressions take into account more factors that are seen to influence bond-slip behaviour but which are not included in existing bond-slip models. The comparison between the Verderame et al. modified model and the proposed model shows that the proposed model better predicts the obtained experimental results and present in this chapter.

The bond-slip relationship proposed still does not fully characterise the overall scenarios found in existing RC structures because it was obtained based only on the experiments present in this work. Therefore, additional tests might be developed in the future to better understand this mechanism. The limited number of available monotonic pull-out tests does not allow establishing general empirical expressions to compute the model parameters. For example, the influence of the compressive concrete strength should be better studied. Other authors refer the influence of the surface roughness of the plain reinforcing bars in the bond-slip, but normally this parameter is neglected. Further studies are suggested to investigate the influence of the bar roughness in the bond stress, as well as on the relationship between the roughness and the manufacturing process which may be

related to the tensile strength. Additional cyclic pull-out tests are essential to verify and improve the cyclic models available in the literature.

2.8 REFERENCES

[1] Fernandes C, Melo J, Varum H, Costa A. Cyclic behaviour of substandard RC beam-column joints with plain bars. *ACI Structural Journal* 2013:110(1):137-148.

[2] Melo J, Varum H, Rossetto T, Costa A. Experimental response of RC columns built with plain bars under unidirectional cyclic loading. Proceedings of the 15th World Conference on Earthquake Engineering. Lisbon. Portugal. 24-28 September. 2012. Paper No. 4495.

[3] Melo J, Fernandes C, Varum H, Rodrigues H, Costa A, Arêde A. Numerical modelling of the cyclic behaviour of RC elements built with plain reinforcing bars. *Engineering Structures* 2011:33(2):273-286. doi: 10.1016/j.engstruct.2010.11.005

[4] Verderame GM, Fabbrocino G, Manfredi G. Seismic Response of R.C. Columns with Smooth Reinforcement. Part II: Cyclic Tests. *Engineering Structures* 2008:30(9):2289-2300. doi: 10.1016/j.engstruct.2008.01.024

[5] Varum H. Seismic assessment, strengthening and repair of existing buildings. PhD Thesis, University of Aveiro, Portugal, 2013.

[6] CEB-FIP. Model Code 2010, First complete draft – Volume 1. International Federation for Structural Concrete. Lausanne, Switzerland, 2010.

[7] Feldman LR, Bartlett FM. Bond strength variability in pullout specimens with plain reinforcement. *ACI Structural Journal* 2005:102(6):860–867.

[8] CEB-FIP. Bulletin 10: Bond of reinforcement in concrete - State-of-art. International Federation for Structural Concrete, Lausanne, Switzerland, 2000.

[9] Abrams D. Tests of bond between concrete and steel. Bulletin No. 71 – Engineering Experiment Station. University Illinois Bull XI(15), 1913.

[10] Stocker MF, Sozen MA. Investigation of prestressed reinforced concrete for highway bridges, part V, bond characteristics of prestressing strand. Bulletin No. 503 – Engineering Experiment Station. University Illinois, 1970.

[11] Verderame GM, Ricci P, Carlo GD, Manfredi G. Cyclic Bond Behavior of Plain Bars. Part II: Analytical Investigation. *Construction and Building Materials* 2009:23(12):3512-3522. doi: 10.1016/j.conbuildmat.2009.07.001

[12] Verderame GM, Ricci P, Carlo GD, Manfredi G. Cyclic Bond Behavior of Plain Bars. Part I: Experimental Investigation. *Construction and Building Materials* 2009:23(12):3499-3511. doi: 10.1016/j.conbuildmat.2009.07.002

[13] Feldman LR, Bartlett FM. Bond stresses along plain steel reinforcing bars in pullout specimens. *ACI Structural Journal* 2007:104(6):685–692.

[14] Fabbrocino G, Verderame GM, Manfredi G. Experimental behaviour of anchored smooth rebars in old type reinforced concrete buildings. *Engineering Structures* 2005:27(10):1575-1585. doi: 10.1016/j.engstruct.2005.05.002

[15] CEB. Bulletin d'Information N. 217 - Selected justification notes. Comité Euro-International du Béton, April, 1993.

[16] Eligehausen R, Popov EP, Bertero VV. Local bond stress–slip relationships of deformed bars under generalized excitations. EERC University of California, Berkeley, Report No. UCB/EERC 83-23, 1983.

[17] Rossetto T, Peiris N, Alarcon J, So E, Sargeant S, Sword-Daniels V, Libberton C, Verrucci E, Re D Free M. The L'Aquila (Italy) Earthquake of 6th April 2009 – A Preliminary Field Report by EEFIT. The Earthquake Engineering Field Investigation Team. The Institution of Structural Engineers, 2009.

[18] Mola E, Negro P. Full scale PsD testing of the torsionally unbalanced SPEAR structure in the "as-built" and retrofitted configurations. SPEAR Workshop – An event to honour the memory of Jean Donea - Ispra, Italy, 2005.

[19] Spence R, D'Ayala D, Martin B, Marinescu J, Sabetta F, Zuccaro G. The Umbria Marche Earthquakes of 26 September 1997. The Earthquake Engineering Field Investigation Team. The Institution of Structural Engineers, 1998.

[20] CEN. EN 10080, Steel for the reinforcement of concrete - Weldable reinforcing steel – General. European Committee for Standardization, Brussels, Belgium, 2005.

[21] Governo D. Regulamento do Betão Armado (RBA), Decreto n.º 25948, 16 de Outubro, serie I, num. 240, Lisbon, 1935. (in Portuguese)

[22] Governo D. Regulamento de Estruturas de Betão Armado (REBA), Decreto n.º 47723, 20 de Maio, serie I, num. 119, Lisbon, 1967. (in Portuguese)

[23] CEN. EN ISO 6892-1:2009, Metallic materials – Tensile testing – Part 1: Method of test at ambient temperature. European Committee for Standardization, Brussels, Belgium, 2009.

[24] Motulsky H, Christopoulos A. Fitting models to biological data using linear and nonlinear regression. A practical guide to curve fitting. GrapPad Software Inc, San Diego, 2003.

[25] CEN. NP EN 1992-1-1, Eurocode 2 - Design of concrete structures. Part 1-1: General rules and rules for buildings. European Committee for Standardization, Brussels, Belgium, 2010.

CHAPTER 3

EXPERIMENTAL CYCLIC BEHAVIOUR OF RC COLUMNS WITH PLAIN BARS

Melo, J., Varum, H., Rossetto, T. Experimental cyclic behaviour of RC columns with plain bars and proposal for Eurocode 8 formula improvement. *Engineering Structures*, resubmitted after revision by authors; under review.

3.1 ABSTRACT

A significant number of existing reinforced concrete building structures were designed and built before 1970, prior to the enforcement of modern seismic design codes. The response of these structures when subjected to cyclic loads, such as that induced by earthquakes, is strongly influenced by the bond properties between the reinforcing bars and the surrounding concrete. This chapter describes the results of a testing campaign composed of seven unidirectional cyclic tests and one monotonic test performed on full-scale columns built with plain bars, without adequate reinforcement detailing for seismic demands. An additional unidirectional cyclic test was carried out on a specimen with deformed bars for reference. The influence of bond properties, a cold joint at the base, lapping of longitudinal reinforcing bars, amount of reinforcing steel, cross-section dimensions and imposed loading history (monotonic or cyclic) is discussed. Finally, a correction coefficient to the expressions of EC8-3 for the calculation of ultimate rotation capacity of columns with plain reinforcing bars is proposed.

3.2 INTRODUCTION

The hysteretic behaviour of reinforced concrete (RC) structures is highly dependent on the interaction between steel and concrete. Cyclic load reversals, such as the ones induced by earthquakes, may result in accelerated bond degradation and significant bar slippage. The bond-slip mechanism is reported as one of the most common contributors to damage and collapse of existing RC building structures subjected to earthquake demands [1]. This process can lead to the failure of structural elements at cyclic steel stress levels lower than their strength [1]. Despite this, bond behaviour is usually disregarded in the analysis of reinforced concrete (RC) structures, with a perfect bond between steel and concrete being typically assumed.

The behaviour of RC elements built with plain reinforcing bars is particularly sensitive to the bond-slip mechanism [2]. For instance, low bond capacities have a strong influence on the fixed-end rotations of structural elements, greatly increasing the bond-slip contribution to the overall element deformation, [3,4,5,6]. Several experimental studies have investigated the cyclic behaviour of RC columns, but few focus on the behaviour of columns designed according to building codes that pre-date the 1970s. In particular, experimental data on the cyclic behaviour of RC elements with substandard details built with plain reinforcing bars is scarce in comparison with that available for elements with deformed bars. Consequently, the cyclic and post-elastic behaviour of elements with plain bars is still not well understood [7]. Recent experimental studies on RC columns with plain bars include those of Verderame et al., [5,6] and Ludovico et al., [7], described here. Some additional experimental studies can also be found in the literature for beam-column joints [2,8-10] and beams [11,12], and are supplemented by data from pull-out tests [13].

Monotonic and cyclic tests on full-scale RC square columns subjected to the combined action of cyclic bending and constant axial forces were performed by Verderame et al. [5,6]. In this testing campaign, the columns were designed according to the guidelines enforced in Italy between 1940 and 1970. Lapping of the longitudinal bars with hooks was provided in three columns and two levels of axial load were adopted. The main aim of the study was to assess the rotation capacity at ultimate limit state of the columns and to compare these with predictions given by Eurocode 8: Part 3 (EC8-3) [14]. The authors concluded that the chord rotation of elements with plain bars results from a

combined action of the fixed end rotation at the base and yielding of the longitudinal reinforcement spread over the column length. They also observed that EC8-3 provisions generally underestimated the ultimate chord rotation of the tested columns and that the hysteretic response of elements was affected by a pinching effect that decreases as the axial load increases.

Ludovico et al. [7] carried out eight tests (monotonic or cyclic) on square and rectangular RC columns designed according to provisions, construction practices and material properties enforced in Italy between 1940 and 1970. The columns were built with continuous reinforcing bars and two axial load levels were adopted. The experiments demonstrated the main differences in terms of global and local behaviour, and also in terms of energy dissipation capacity, of RC columns representative of old RC structures built with plain and deformed reinforcing bars. Ludovico et al. [7] observed a spread crack pattern and a main singular crack on columns with deformed and plain bars, respectively. As a consequence, the contribution of the base rotation on the global deformation was larger in the columns with plain bars. Furthermore, the ultimate rotation capacity of columns with plain bars was observed to be higher than that of columns with deformed bars. Similar dissipated energy was obtained for both types of columns for the same deformation path imposed.

Available data on the cyclic behaviour of non-seismically detailed RC columns built with plain reinforcing bars is scarce and additional experiments are necessary to properly understand and characterise their cyclic behaviour. The experimental investigation described in this chapter contributes to enlarge the available database on RC columns built with plain reinforcing bars. Cyclic and monotonic tests are performed on nine full-scale columns, representative of existing RC structures designed according to the Portuguese RC codes enforced between 1935 and 1970 [15,16]. Eight specimens were built with plain reinforcing bars and one with deformed reinforcing bars, allowing the response comparison with the aim to better characterise and understand the influence of bar slippage on the response.

3.3 EXPERIMENTAL CAMPAIGN

3.3.1 Specimens detailing and materials properties

The experimental campaign was carried out in the Department of Civil Engineering at the University of Aveiro. It consisted of eight full-scale column specimens built with plain reinforcing bars, with different cross-sections and reinforcement details. Seven of the specimens were tested under unidirectional cyclic conditions and one was tested monotonically. A ninth specimen was built with deformed reinforcing bars and tested cyclically. The comparison of the results of this test with the results of a similar specimen built with plain bars allows for a better understanding of the influence of the bond-slip mechanism on the element's cyclic behaviour.

The nomenclature adopted for the specimens was: i) a first letter (C); ii) a second letter (P or D) refers to the reinforcing steel type (P, plain; or D, deformed); iii) a third letter (A to F) distinguishes the reinforcing detailing and cross-section type. The geometry, dimensions and reinforcing details of the specimens are shown in Figure 3.1. Each specimen represents a half-storey cantilever column (at foundation level) in a building with three or four storeys. So, the length of the column specimens is 2.17m (85.4in) and the lateral load is applied at 1.7m (66.9in) from the columns base. Seven specimens (CPA-1; CPA-2; CPA-3; CPB; CPC; CPD and CD) have square cross-sections with dimensions of 0.30x0.30m^2 (11.81x11.81in^2) and the other two specimens, CPE and CPF, have rectangular cross-sections with dimensions of 0.30x0.40m^2 (11.81x15.75in^2) and 0.30x0.50m^2 (11.81x19.67in^2), respectively. The foundation consists of a stiff RC block with a section of 0.30x(0.30+column cross-section depth)m^2 (11.81x(11.81+column cross-section depth)in^2) and 1.5m (59.1in) length.

The longitudinal reinforcement of the columns in both lateral faces is composed of three bars of 12mm (0.47in) diameter in specimens CPA-1, CPA-2, CPA-3, CPB, CD and CPE and of four bars of 12mm (0.47in) diameter for specimens CPC, CPD and CPF. Furthermore, in specimens CPE and CPF two bars with 12mm (0.47in) diameter were additionally placed at half section depth. The longitudinal reinforcement ratio (ρ_l) is equal to 0.75% in all specimens, except in specimens CPC and CPD where it has a value of 1%. The shear reinforcement in the columns was composed of 8mm (0.32in) diameter stirrups spaced at 0.20m (7.87in) centres.

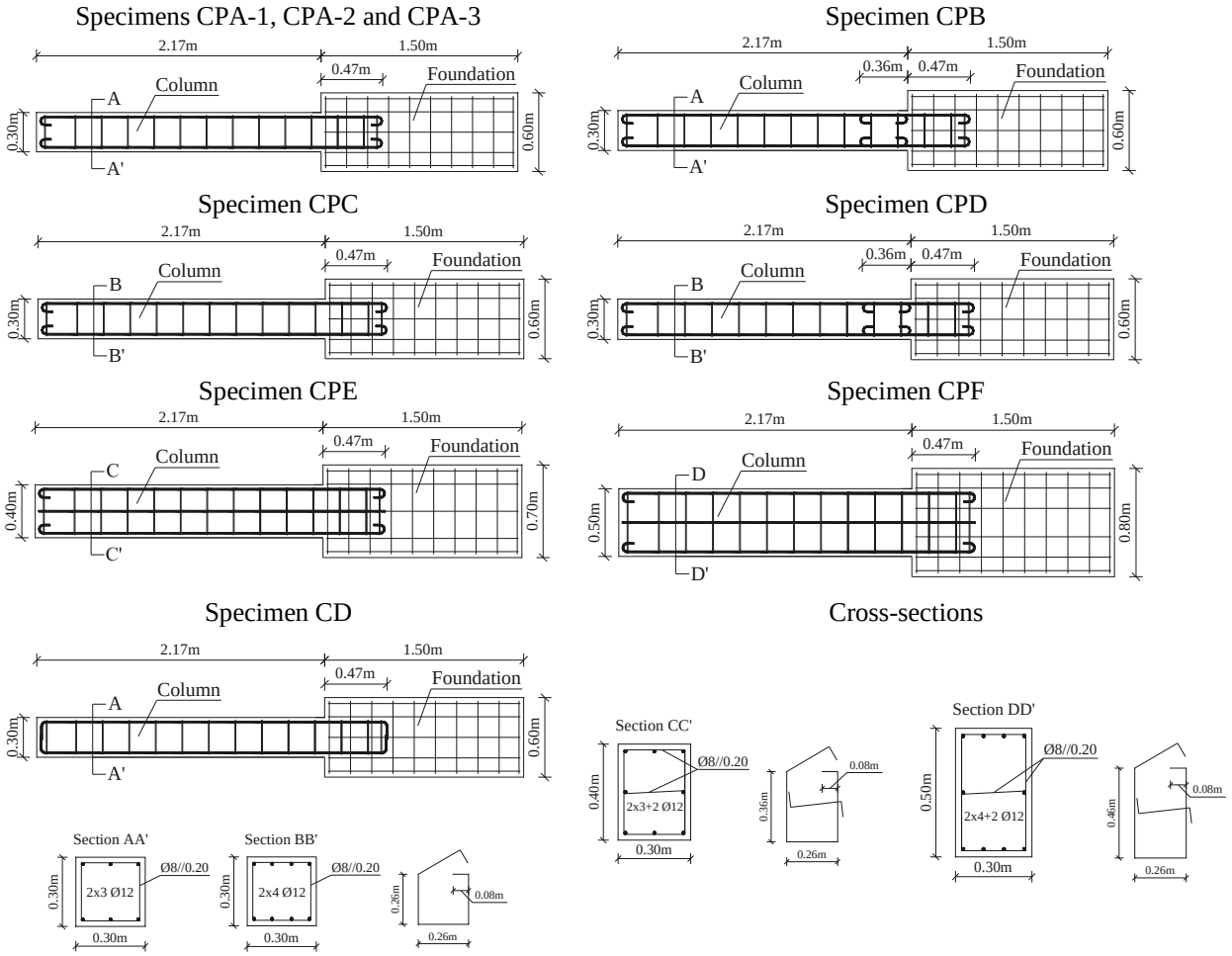

Note: 1m=39.4 in

Figure 3.1 – Geometry, dimensions and reinforcement detailing of the specimens.

All specimens were cast at different dates in a single phase, but specimen CPA-1 was cast in two phases, first the foundation and then the column. After the first casting phase a gouge was used to increase the surface roughness of the concrete surface on the column base area. This was done in order to be able to study the effect of a cold joint on the response of the column. Specimens CPA-1, CPA-2 and CPA-3 have the same column cross-section dimensions and reinforcement details, but specimen CPA-1 has a cold joint and specimen CPA-2 was tested monotonically. Specimen CPA-3 is assumed as the reference specimen in all the analyses made in this chapter. Specimen CPB is similar to the reference specimen but with lapping of the longitudinal reinforcement at the column base. Specimens CPC and CPD have larger amounts of longitudinal reinforcing steel relative to the reference specimen and specimen CPD also has lapping of the longitudinal reinforcement. Specimens CPE and CPF have larger cross-section depth and larger longitudinal steel amounts than specimen CPA-3. Specimen CD has the same cross-section

dimensions and reinforcing detailing as specimen CPA-3 but was built using deformed bars.

The length of the longitudinal reinforcing bars through the foundation is 0.47m, corresponding to a typical anchoring length for a foundation with 0.5m depth. The anchorage detailing of the reinforcing plain bars were designed according to the first Portuguese reinforced concrete structures codes, namely RBA (1935) [15] and REBA (1967) [16], which represents the common practice in southern European countries. The anchorage of the longitudinal plain reinforcing bars consisted in 180º end hooks, with the mandrel diameter and the straight prolongation after the hook being 4 times the bar diameter. In the specimen with deformed bars the bar anchorage consisted of 90º end hooks. The lap-splice length adopted in specimens CPB and CPD were also designed according to the above mentioned Portuguese codes, i.e. 30 times the bar diameter. The stirrups were anchored by a 90º hook.

Table 3.1 summarises the mean values of the material properties used in the construction of the specimens, where f_{cm} is the concrete compressive strength of cylinder samples with dimensions of 150mmx300mm (5.9inx11.8in), f_{ctm} is the axial tensile strength of concrete, f_{ym} is the yield strength of reinforcement, f_{um} is the ultimate tensile strength of reinforcement and E_{ym} is the Young's modulus of the reinforcing steel. The grades of the hot-rolled plain and deformed reinforcing steel bars used in the column specimens were A235 and A400NRSD, respectively. For each bar diameter three tensile tests were performed according to the standard norm EN ISO 6892-1 (2009) [17]. The concrete compressive tests were made according to the standard norm NP EN 12390-3 (2011) [18]. All concrete cylinder samples were tested simultaneously with the test on the corresponding column specimen, and never before of 90 days curing.

Table 3.1 – Mean values of the materials (concrete and steel) mechanical properties.

Column Specimen	Concrete MPa (ksi)		Bar surface	Steel Ø8 mm MPa (ksi)		Steel Ø8 mm GPa (ksi)	Steel Ø12 mm MPa (ksi)		Steel Ø12 mm GPa (ksi)
	f_{cm}	f_{ctm}		f_{ym}	f_{um}	E_{ym}	f_{ym}	f_{um}	E_{ym}
CPA-1	21.2 (3.07)	2.2 (0.32)	Plain	410 (59.5)	495 (71.8)	198 (28717)	405 (58.7)	470 (68.2)	199 (28863)
CPA-2	19.1 (2.77)	2.1 (0.30)							
CPA-3	17.4 (2.52)	2.1 (0.30)							
CPB	20.3 (2.94)	2.2 (0.32)							
CPC	17.1 (2.48)	2.1 (0.30)							
CPD	18.0 (2.61)	1.9 (0.28)							
CPE	18.0 (2.61)	1.9 (0.28)							
CPF	18.3 (2.65)	2.0 (0.29)							
CD	17.1 (2.48)	2.0 (0.29)	Deformed	470 (68.2)	605 (87.7)	198 (28717)	465 (67.4)	585 (84.8)	199 (28863)

3.3.2 Test apparatus, loading conditions and monitoring

Figure 3.2 illustrates the test apparatus, namely the idealised support and loading conditions, the imposed lateral displacement history at the top of the columns, the test setup schematics, the general view and the monitoring scheme adopted. The specimens were tested in the horizontal position, as shown in Figure 3.2-c. Two devices with high load-carrying capacity and low friction were connected to the column inferior face, allowing the transfer of its self-weight to two concrete blocks placed below the column.

The axial force (N) was applied by a hydraulic actuator mounted at the top of the column associated to two tie rods linked to the foundation of the column. The tie rods are hinged at the column base section. Thus, the axial load is always centred with the column section at the base, avoiding the occurrence of second order effects. The axial force applied was constant along the cyclic test for all specimens. An axial load corresponding to an axial force ratio (ν) of 18% was applied. Thus, for specimens with square cross-section, for specimen CPE and for specimen CPF, axial loads of 305kN (68.6kip), 408kN (91.7kip) and 485kN (109.0kip) were imposed, respectively. During the tests (cyclic or monotonic), the maximum axial load deviation was 4% relative to the initial imposed axial load due to the constant adjustments made by the actuator.

All tests were carried out under displacement-control conditions. Apart from specimen CPA-2, which was tested under monotonic loading conditions up to 9% drift, all other specimens were tested cyclically. The cyclic lateral displacement history adopted is represented in Figure 3.2-a. A hydraulic servo-actuator was mounted to impose the lateral

displacements (d_c) at 1.7m (66.9in) from the column base (see Figure 3.2). Three cycles with load reversals were imposed for each of the following peak drift values (± %): 0.1, 0.2, 0.3, 0.5, and then increments of 0.5 up to 5.5. Some tests were stopped before 5.5% drift due to the high damage level achieved.

Six Linear Variable Displacement Transducers (LVDTs) were used for monitoring the global displacement evolution at the top and base of the column, as well as the displacements of the block foundation. Twenty two potentiometers were used for monitoring the relative displacement evolution in different points along the span of the column. The potentiometer arrangements are shown in Figure 3.2-d.

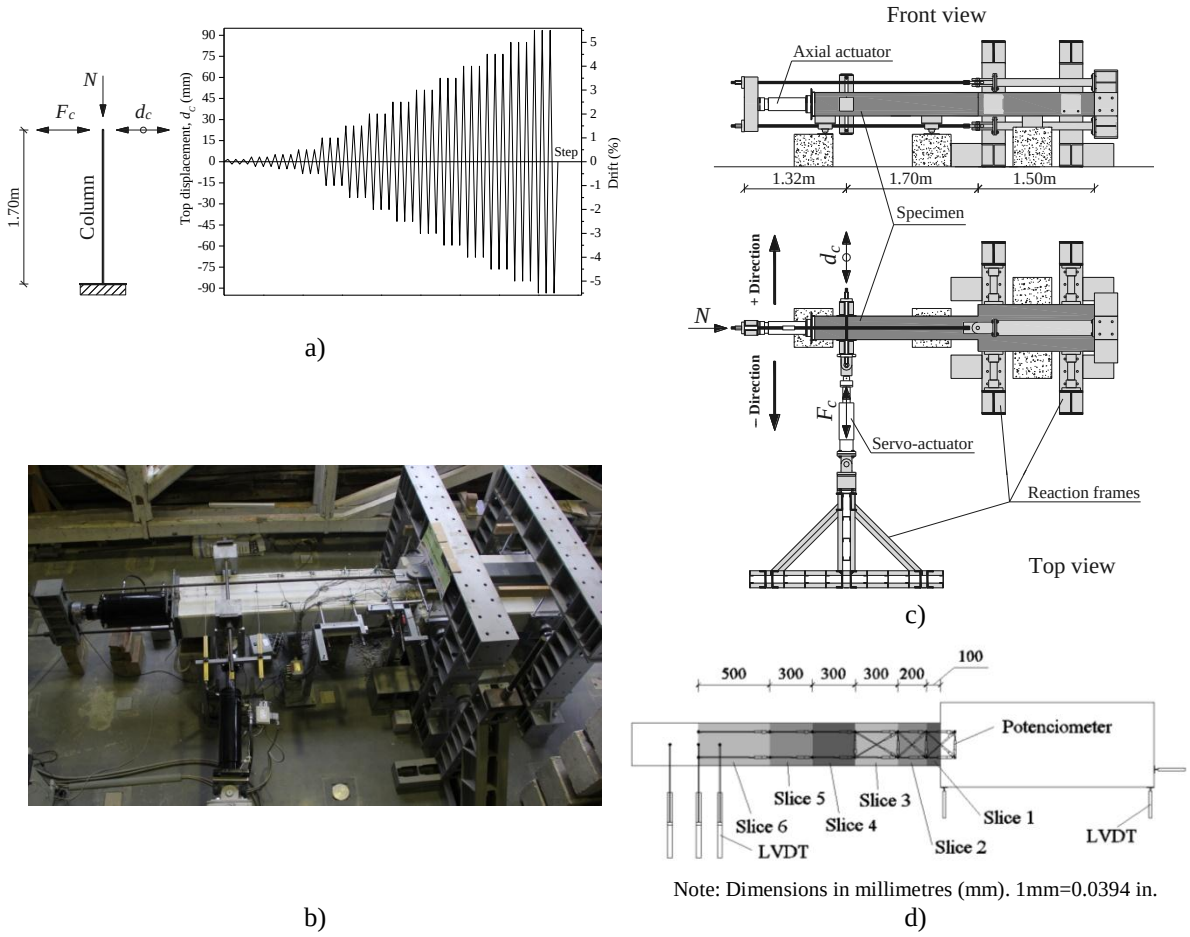

Note: Dimensions in millimetres (mm). 1mm=0.0394 in.

Figure 3.2 – Test apparatus: a) support and loading conditions idealized and imposed lateral displacement history; b) general view; c) test setup schematics; and d) monitoring scheme.

3.4 EXPERIMENTAL RESULTS AND DISCUSSION

In this section the experimental results are presented and discussed. In particular the hysteretic force-drift diagrams, the force-drift envelopes, the hysteretic dissipated energy

evolution, the equivalent damping-displacement ductility relationships, the ultimate rotation capacity, the HRC-damage index proposed by Rossetto and Elnashai [19] and the drift components of the columns tested are presented. Comparisons are made between the experimental results in order to discuss the influence of: i) reinforcing steel type (plain/deformed); ii) the presence of a lap-splice in the longitudinal reinforcing steel bars; iii) the presence of a cold joint at the column base; iv) amount of reinforcing steel; v) cross-section dimensions; and vi) imposed lateral load (monotonic or cyclic). The final damage states are also compared. The results of specimen CD are presented only up to 3.5% drift since a problem was observed with the data acquisition system past this stage of the test. But, the damage state showed in Figure 3.10 corresponds to the end of the test (5% drift).

3.4.1 Force-drift response

Figure 3.3 and Figure 3.4 present, respectively, the cyclic response of the columns tested, in terms of the lateral force versus imposed drift, and the envelope curves. In Figure 3.3 each plot represents the cyclic behaviour of two or three different specimens, in order to highlight the differences for each variable under study, namely: bond properties (CPA-3 versus CD); the presence of a lap-splice in the longitudinal reinforcing bars (CPA-3 versus CPB, and CPC versus CPD); the presence of a cold joint at the column base (CPA-3 versus CPA-1); amount of steel reinforcement (CPA-3 versus CPC); and cross-section dimensions (CPA-3 versus CPE and CPF). In Figure 3.3 the flexural capacity (corresponding to the maximum lateral load) of each specimen, computed according to the Eurocode 2, Part 1-1 (EC2-1-1) [20] formulation is also shown, i.e. assuming plane cross-section and perfect bond (no slippage between steel reinforcement and concrete) conditions. Moreover, in Figure 3.3 points are plotted corresponding to the onset of different damage states observed during the tests. These are: concrete cracking, concrete cover spalling and buckling of steel rebar. Table 3.2 summarises the response values (for positive direction) in terms of maximum force ($F_{c,max}$), drift at maximum force ($Drift_{Fc,max}$), ultimate force ($F_{c,ult}$) and drift at ultimate point ($Drift_{ult}$). The ultimate point corresponds to the conventional failure, i.e. when a strength reduction of 20% relative to the maximum force is observed as adopted by Park and Ang [21]. For specimen CPA-2 (monotonic test), the maximum strength

reduction was 7.5% at the end of the test (9.0% drift), consequently the ultimate point was not achieved.

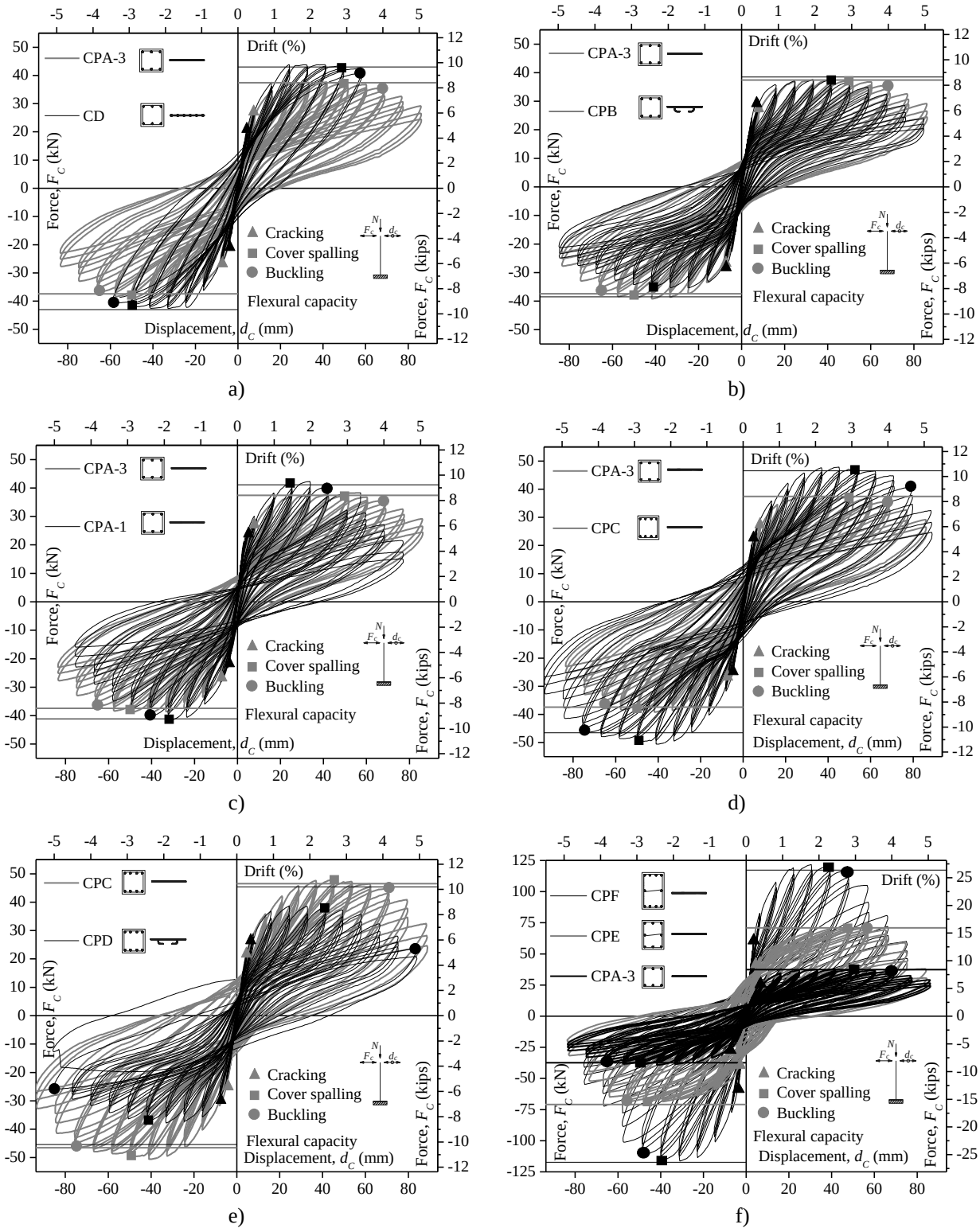

Figure 3.3 – Lateral force versus drift: a) CPA-3 versus CD; b) CPA-3 versus CPB; c) CPA-3 versus CPA-1; d) CPA-3 versus CPC; e) CPC versus CPD; and f) CPA-3 versus CPE and CPF. (Note: 1mm = 0.0394in)

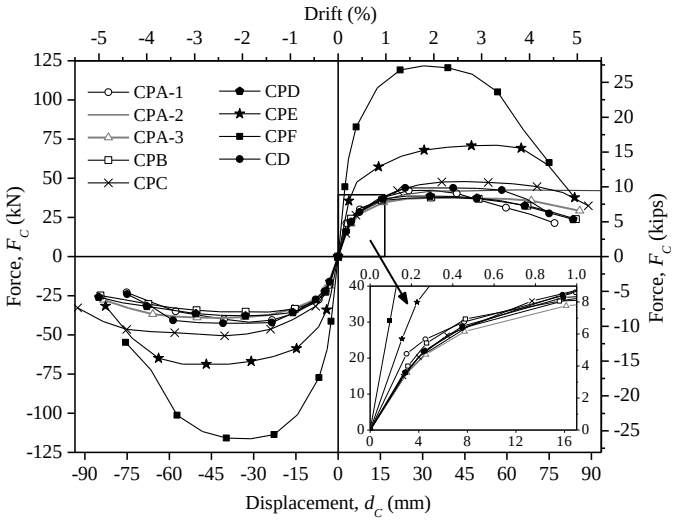

Figure 3.4 – Force-drift envelopes for all column specimens. (Note: 1mm = 0.0394in)

Table 3.2 – Force and drift for the maximum strength and ultimate points.

Specimen	$F_{c,max}$ kN (kips)	$Drift_{Fc,max}$ %	$F_{c,ult}$ kN (kips)	$Drift_{ult}$ %
CPA-1	42.3 (9.51)	1.98	33.8 (7.60)	3.21
CPA-2	42.6 (9.58)	3.73	-	-
CPA-3	39.2 (8.81)	2.45	31.3 (7.04)	4.53
CPB	37.6 (8.45)	2.43	30.1 (6.77)	4.26
CPC	50.6 (11.37)	2.37	40.4 (9.08)	4.97
CPD	38.7 (8.70)	1.43	30.9 (6.95)	4.07
CPE	71.1 (15.98)	3.32	56.9 (12.79)	4.43
CPF	121.7 (27.36)	1.79	97.4 (21.90)	3.50
CD	43.8 (9.85)	1.40	35.1 (7.89)	4.00

For all specimens, the cyclic response was fairly symmetric. Among the specimens with square cross-section and with the same amount of steel reinforcement, the maximum difference in terms of maximum force was 5kN (1.12kips), i.e. approximately 12%, relatively to the maximum strength of the reference specimen (CPA-3). The initial stiffness was similar for all the specimens with square cross-section (see Figure 3.4).

In specimen CPA-1 (with cold joint at the column base), the maximum strength was achieved for a lower drift value (1.98%) than that obtained for specimen CPA-3 (2.45%). Also, the specimen with cold joint reached the ultimate point at a lower drift value and showed larger strength degradation. These differences can be justified by the larger curvatures observed in slice 1 of specimen CPA-1 compared to specimen CPA-3, for the same drift demands, due to the cold joint. As a consequence, larger concrete damage was observed in slice 1 (see Figure 3.2-d) of specimen CPA-1 and the buckling of bars occurred for a small drift demand.

Specimen CPA-2, tested monotonically, shows larger maximum strength (8% more) than specimen CPA-3. The strength degradation associated to the specimen subjected to cyclic load (CPA-3) is much larger than that observed for the monotonically loaded specimen (CPA-2).

The specimen with lap-slice (CPB) displayed similar maximum strength and larger strength degradation than the specimen without longitudinal reinforcement lapping (CPA-3).

Specimen CPC shows a larger peak force (29% more) than specimen CPA-3. Specimen CPD displays a lower peak force (24% less) than specimen CPC. The maximum strength of specimen CD was 12% larger than the peak force of specimen CPA-3 and it was achieved at a lower drift value (1.40% drift against 2.45% drift).

The specimens with rectangular cross-section show larger peak force and larger strength degradation than the square columns. The flexural capacity estimated according to EC2-1-1 [20] shows good agreement with the experimental results of specimen CD (built with deformed bars), underestimating the maximum strength only by 1.9%. However, for specimens built with plain bars the predicted flexural capacity shows higher levels of error with respect to the experimental observations, the largest overestimation observed for specimen CPD (14.8%) and the largest underestimation for specimen CPC (8.7%). This larger uncertainty in flexural strength prediction might be related to the larger amount of reinforcement in specimen CPC and the presence of a lap-splice in specimen CPD.

Flexural cracks were first observed at the column base for drifts ranging from 0.2% (CPA-2) to 0.5% (CPA-3, CPB, CPD). The onset of concrete cover spalling was observed for drift values from 1.5% (CPA-1) to 3.5% (CPA-2). The onset of reinforcement buckling was observed at drifts ranging from 2.5% (CPA-1) to 4.5% (CPC).

3.4.2 Dissipated energy evolution and equivalent damping versus displacement ductility

Figure 3.5 shows the evolution of dissipated hysteretic energy, as computed from the experimental results. In the same figure, the larger points represent the energy dissipated at the ultimate drift. Specimen CD (with deformed bars) dissipated 22% more energy than specimen CPA-3 (with plain bars), as has already been observed by other authors [2].

Specimen CPA-1 had the smaller amount of dissipated energy compared to CPA-3 until the ultimate point (48% lower). Specimens with lap-splice (CPB and CPD) dissipated, up to the ultimate point, 22% and 57% less energy than similar specimens without lap-splices (CPA-3 and CPC). Despite the higher peak force observed for specimen CPF when compared with specimen CPE (71% higher), specimen CPE dissipated more energy (+49%) than specimen CPF. This is due to a more pronounced pinching effect observed in specimen CPF.

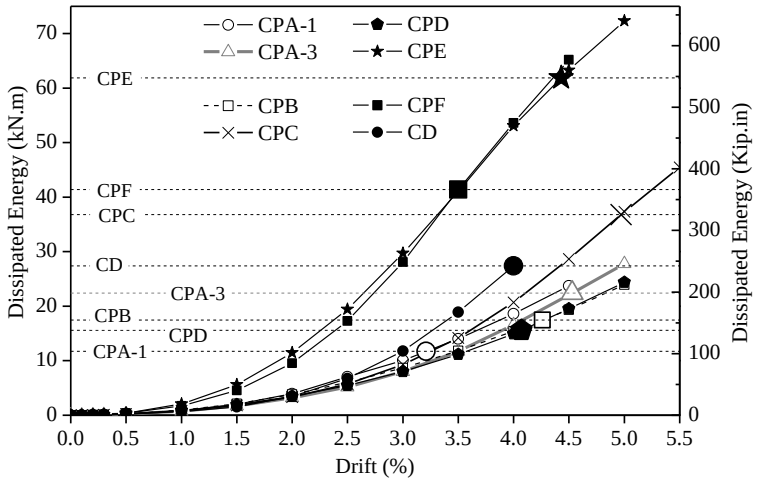

Figure 3.5 – Hysteretic dissipated energy evolutions.

The equivalent damping for concrete structures, is usually defined as a function of the structural displacement ductility (μ_Δ). The total equivalent viscous damping (ξ_{eq}) is the sum of the initial damping (ξ_0) in the elastic range and the hysteretic damping (ξ_{hyst}), where the hysteretic damping depends on the nonlinear response. The initial damping for concrete structures is normally taken as 5% [22]. The equivalent damping was computed according to expression (1), presented in Varum [23], where $A_{half\text{-}loop}$ is the area within a half force-displacement cycle and F_{max} and D_{max} are the maximum force and displacement achieved in that half cycle.

$$\xi_{eq} = \frac{1}{\pi} \cdot \frac{A_{half-loop}}{F_{\max} \cdot D_{\max}} \tag{3.1}$$

The displacement ductility (μ_Δ) is the ratio between the maximum displacement imposed in each cycle (d_c) and the displacement corresponding to yield (Δ_y). The yield displacement was computed according to Annex B.3 of EC8-1 [24], with an elastic-perfectly plastic force-displacement relationship assumed. For each column, an elastic-perfectly plastic

relationship was fitted to the experimental results up to the ultimate point of the force-displacement envelopes, ensuring the following requirements were satisfied (see Figure 3.6): i) the areas under (A_1) and above (A_2) the experimental envelope curve must have the same values; and ii) the area under (or above) the envelope curve is the lowest possible.

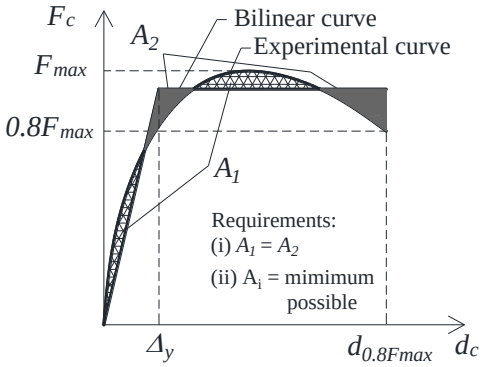

Figure 3.6 – Bilinear approach method adopted to find the yield displacement.

The equivalent damping versus displacement ductility relationship and the best fitted curve for each test are shown in Figure 3.7. In Table 3.3 the yield force ($F_{c,y}$), the yield drift value ($Drift_y$), the equivalent damping at the ultimate point ($\xi_{eq,ult}$) and the displacement ductility at the ultimate point ($\mu_{\Delta,ult}$) are shown. For displacement ductility $\mu_\Delta \geq 2.0$, the specimen with deformed bars (CD) presented larger equivalent damping when compared to other specimens with plain reinforcement and the same cross-section dimensions. For example, at the ultimate point, the equivalent damping of specimen CD is 49% larger than for the reference specimen CPA-3. This shows that better bond conditions provided by deformed reinforcing bars may increase the equivalent damping for the same demand level. Specimens CPC and CPD, with higher steel amount, presented larger equivalent damping than the reference specimen. Specimens with lap-splices showed lower equivalent damping than specimens with continuous longitudinal reinforcement for displacement ductility $\mu_\Delta \geq 3.0$. Specimen CPA-1, with a cold joint at the column base, presents lower displacement ductility at the ultimate point than the reference column, due to the earlier occurrence of damage.

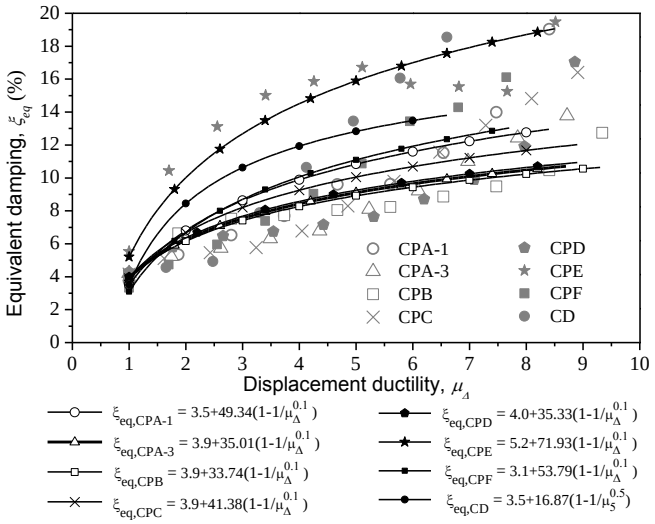

Figure 3.7 – Equivalent damping-displacement ductility diagrams: a) experimental results and fitted curves; and b) comparison between the experimental results and equations proposed by other authors.

Table 3.3 – Yield force, yield drift, equivalent damping and displacement ductility at ultimate point.

Specimen	$F_{c,y}$ **kN (kips)**	$Drift_y$ **%**	$\xi_{eq,ult}$ **%**	$\mu_{\Delta,ult}$
CPA-1	38.7 (8.70)	0.535	10.43	6.00
CPA-2	40.9 (9.19)	0.594	-	-
CPA-3	36.2 (8.14)	0.574	12.49	7.89
CPB	34.9 (7.85)	0.535	9.99	7.96
CPC	45.4 (10.21)	0.618	14.71	8.04
CPD	36.2 (8.14)	0.565	10.15	7.20
CPE	65.6 (14.75)	0.587	15.29	7.54
CPF	112.3 (25.25)	0.588	13.44	5.95
CD	40.7 (9.15)	0.606	18.55	6.60

Equations (3.2), (3.3) and (3.4) were proposed by other authors [25] for elements with deformed bars to compute the equivalent damping-displacement ductility relationships. Equation (3.2), proposed by Gulkan and Sozen [26], was defined based on Jacobsen's approach and using a Takeda hysteresis model. Equation (3.3), proposed by Kowalsky and Ayers [27], is associated with the Takeda modified model, and considers α=0.5, β=0 and r=0.05. Equation (3.4) was proposed by Priestley [28] for concrete columns and walls. In Equations (3.2) and (3.3), the initial damping (ξ_0) is assumed to be 5%, as assumed in other works [25].

Equation (3.5) is based on the experimental results obtained from pseudo-dynamic tests on a full-scale RC frame structure built with plain bars, reported in Varum [23]. Equation (3.5) was calibrated to the experimental results at the storey global level (storey shear versus inter-storey drift), due to the type of response of that frame (that was mainly

governed by the deformation of the columns) this equation can be compared with the equivalent damping curves obtained for columns. Equation (3.6) is based on experimental results of beam-column joints built with plain bars, developed by Fernandes et al. [2].

Takeda Model, Gulkan and Sozen [26]:

$$\xi_{eq} = \xi_0 + 0.2\left(1 - \frac{1}{\mu^{0.5}}\right) \tag{3.2}$$

Takeda Model, Kowalsky and Ayers [27], α=0.5, β=0, r=0.05:

$$\xi_{eq} = \xi_0 + \frac{1}{\pi}\left(1 - \frac{0.95}{\mu^{0.5}} - 0.95 \cdot \mu^{0.5}\right) \tag{3.3}$$

Concrete columns and walls, Priestley [28]:

$$\xi_{eq} = 5 + \frac{95}{\pi}\left(1 - \frac{1}{\mu^{0.5}}\right) \tag{3.4}$$

Structural response governed by column mechanisms, Varum [23]:

$$\xi_{eq} = 3.5 + \frac{173}{\pi}\left(1 - \frac{1}{\mu^{0.1}}\right) \tag{3.5}$$

Concrete beam-column joints, Fernandes et al. [2]:

$$\xi_{eq} = 4.8 + \frac{67}{\pi}\left(1 - \frac{1}{\mu^{0.1}}\right) \tag{3.6}$$

General equation proposed by Priestley [28]:

$$\xi_{eq} = \xi_0 + a \cdot \left(1 - \frac{1}{\mu^{\beta}}\right) \tag{3.7}$$

Concrete columns, fitted curve:

$$\xi_{eq} = 3.8 + \frac{146}{\pi}\left(1 - \frac{1}{\mu^{0.1}}\right) \tag{3.8}$$

Figure 3.8 compares the equivalent damping-displacement ductility relationships obtained from the experiments on columns with plain bars with the curves based on equations proposed by other authors for elements with deformed bars [25]. Equation (3.8) was obtained by fitting the curve, following the general Equation (3.7), with the experimental results present in this work. The equivalent damping-displacement ductility relationships computed according to Equations (3.2), (3.3) and (3.4) overestimate the values calculated directly from the experimental results. It is recalled that these equations were developed for concrete structures built with deformed bars, i.e., with larger energy dissipation capacities, which results in the overestimation observed. A value of 0.5 is commonly adopted for parameter β in Equation (3.7), for RC structures or elements built with deformed bars [26,28]. However, for RC structures or elements built with plain bars a different value is

suggested in this work, i.e. β=0.1. This suggestion is supported by the observations in experimental results available in the literature [2,23] and also by the results presented in this work. This conclusion highlights the need for the development of simplified expressions for the equivalent damping of RC elements typical of old structures built with plain bars. However, it is recognised that in order to achieve this a more extensive experimental testing campaign should be developed on RC elements and structures representative of the most common old RC buildings.

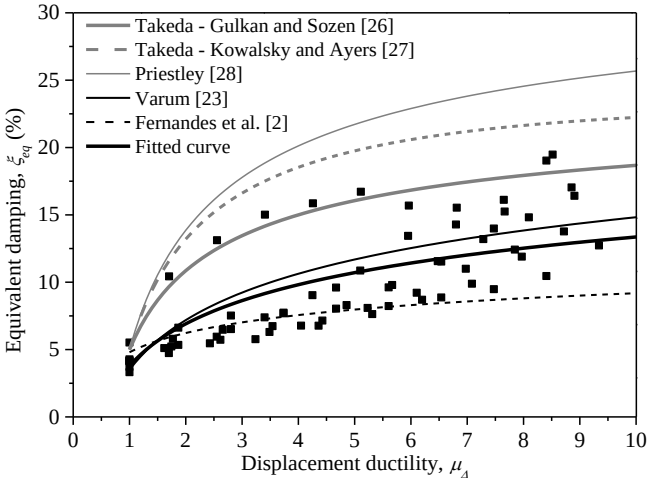

Figure 3.8 – Comparison between the experimental equivalent damping-displacement results and the equations proposed by other authors.

3.4.3 Ultimate rotation capacity

3.4.3.1 Experimental results

Eurocode 8: Part 3 (EC8-3) [14] evaluates the deformation capacity of linear RC elements in terms of chord rotation. Chord rotation is defined as the angle between the tangent to the axis at the yielding end and the chord connecting that end with the end of the shear span (contraflexure point). The chord rotation can be also defined by the element drift ratio, i.e., the deflection at end of the shear span with the respect to the tangent to the axis at the yielding end, divided by the shear span. EC8-3 and Corrigenda to EC8-3 [29] present an empirical expression (Equation (3.9)), called "expression A.1", to calculate the ultimate rotation (θ_{um}) for RC elements built with deformed bars and with adequate seismic detailing. In the same documents, an empirical correction coefficient to expression A.1 is proposed for the computation of the ultimate rotation capacity in elements built with plain reinforcing bars. The correction coefficient varies between 0.40 and 0.8, depending on the lap-splice length. For elements without lapping of the longitudinal bars the correction

coefficient is 0.8 [29]. For the cases in which the longitudinal bars are lapped from the base of the column, with standard hooks in both extremities of the lapping bars, and with a lap length (l_0) larger than 15 times the bar diameter (d_{bL}), the correction factor is taken equal to $0.019 \cdot [10+\min\{40; l_0/d_{bL}\}]$. Furthermore, in expression A.1 the shear span (L_V) is reduced by the lap length l_0, as the ultimate condition is controlled by the region right after the end of the lap. For elements without adequate seismic detailing, the correction factor is also multiplied by 1/1.2 [14,29].

Equation A.1 [29]:

$$\theta_{um} = \frac{1}{\gamma_{el}} 0.016 \cdot (0.3^{\nu}) \left[\frac{max(0.01,\omega')}{max(0.01,\omega)} f_c \right]^{0.225} \left(min\left(9; \frac{L_V}{h}\right) \right)^{0.35} 25^{\left(\alpha\rho_{sx}\frac{f_{yw}}{f_c}\right)} \left(1.25^{100\rho_d}\right) \quad (3.9)$$

In Equation (3.9): γ_{el} is equal to 1.5 for primary seismic elements and to 1.0 for secondary seismic elements; h is the depth of cross-section; L_V is the shear span; ν is the axial load ratio; ω and ω' are the mechanical longitudinal reinforcement ratio of the tension (including web reinforcement) and compression, respectively; f_c and f_{yw} are the concrete compressive strength (MPa) and the stirrup yield strength (MPa), respectively; ρ_{sx} is the ratio of the transverse steel parallel to the direction of loading; ρ_d is the steel ratio of diagonal reinforcement; and α is the confinement effectiveness factor (see [14]).

According to the EC8-3 design philosophy, the ultimate rotation capacity of RC columns built with plain bars is always inferior to similar elements built with deformed bars. However, according to Ricci et al. [30], experimental results indicate that certain elements with plain bars may have larger rotation capacities than similar elements with deformed bars. Based on 30 cyclic tests on columns with plain bars, carried out by different authors [6,7,31-40], Ricci et al. [30] proposed modifications to the correction coefficient present in Corrigenda to EC8-3 [29]. This proposal follows the previous study conducted by Verderame et al. [4]. For elements with continuous longitudinal reinforcement the coefficient proposed by Ricci et al. [30] is 1.0. Essentially, they propose to adopt the same ultimate rotation capacity for elements with plain and with deformed bars. For elements with lap-splice, the correction coefficient proposed is $0.010 \cdot [50+\min(50; l_0/d_{bL})]$. For reinforcing bars without lapping, the lap length ratio assumes the value 1.00.

Table 3.4 – Ratios between the experimental observed and the predicted ultimate rotation capacity.

#	Reference	Specimen	Section hxb (cmxcm)	L_V (m)	ν	f_{cm} (MPa)	f_{ym} (MPa)	l_0/d_{bL}	$\theta_{u,exp}$ (%)	(i) $\frac{\theta_{u,exp}}{\theta_{um}}$	(ii) $\frac{\theta_{u,exp}}{\theta_{um,EC8}}$	(iii) $\frac{\theta_{u,exp}}{\theta_{um,R.}}$	(iv) $\frac{\theta_{u,exp}}{\theta_{um,prop.}}$
1	Bousias et al. (2007) [31]	Q-0L1a	25x25	1.60	0.63	28.1	330	15	1.00	0.35	0.88	0.53	-
2		Q-OL1	25x25	1.60	0.41	30.3	330	15	2.50	0.65	1. 64	1.00	
3		Q-0L2	25x25	1.60	0.38	30.3	330	25	2.20	0.60	1.08	0.80	
4		Q-0L2a	25x25	1.60	0.57	28.1	330	25	1.35	0.45	0.81	0.60	
5	Arani et al. (2010) [37]	HOS-C	25x25	0.75	0.15	24.8	370	20	5.13	1.45	3.05	2.08	
6	Bousias et al. (2007) [31]	Q-0	25x25	1.60	0.44	27.0	313	100	2.20	0.58	0.73	0.58	1.02
7	Bournas et al. (2007) [32]	C	25x25	1.60	0.30	25.0	372	100	3.75	0.85	1.06	0.85	1.01
8	Verderame et al. (2008) [6]	C-540A1	30x30	1.57	0.12	24.3	355	40	6.48	1.45	1.83	1.61	1.23
9		C-540B1	30x30	1.57	0.24	24.3	355	40	3.81	0.98	1.24	1.09	1.02
10		C-540B2	30x30	1.57	0.24	24.3	355	40	2.77	0.71	0.90	0.79	0.74
11		C-270A1	30x30	1.57	0.12	24.3	355	100	6.22	1.22	1.53	1.22	1.03
12		C-270A2	30x30	1.57	0.12	24.3	355	100	5.81	1.14	1.43	1.14	0.96
13		C-270B1	30x30	1.57	0.24	24.3	355	100	3.72	0.84	1.05	0.84	0.88
14	Faella et al. (2008) [33]	C3-S	30x30	1.70	0.15	25.7	346	43	3.89	0.88	1.11	0.95	0.81
15		C16-S	30x30	1.70	0.40	27.5	346	43	3.21	0.98	1.24	1.05	1.69
16		C18-S	30x30	1.70	0.40	13.5	346	43	3.11	1.11	1.40	1.19	0.96
17	Marefat et al. (2008) [34]	CC2N	20x20	0.75	0.20	23.0	356	100	4.57	1.93	2.41	1.93	1.60
18	Ozcan et al. (2008) [35]	S-NL-0-34	35x35	2.00	0.40	14.0	287	100	2.50	0.86	1.08	0.86	0.78
19	Di Ludovico et al. (2009) [7]	C-S30-s(A2)	30x30	1.50	0.20	18.9	330	100	5.42	1.44	1.80	1.44	1.21
20		C-R30-s(C2)	30x50	1.50	0.10	18.9	330	100	6.22	1.39	1.74	1.39	1.03
21		C-R50-s(A2)	50x30	1.50	0.10	18.9	330	100	5.27	1.65	2.06	1.65	1.23
22	Bournas and Triantafillou (2009) [36]	control	25x25	1.60	0.20	25.6	372	100	6.24	1.25	1.56	1.25	1.27
23	Arani et al. (2010) [37]	WOS-C	25x25	0.75	0.15	22.9	370	100	6.07	1.53	1.91	1.53	1.20
24	Ozcan et al. (2010) [38]	S1	20x20	2.00	0.51	12.0	287	100	1.66	0.70	0.88	0.70	0.62
25	Acun and Sucuoglu (2010) [39]	2P3	35x35	2.00	0.20	13.0	315	100	5.25	1.43	1.79	1.43	1.09
26		3P3	35x35	2.00	0.40	13.0	315	100	3.50	1.21	1.51	1.21	1.05
27		4P4	35x35	2.00	0.20	13.0	315	100	5.25	1.43	1.79	1.43	1.09
28		5P5	35x35	2.00	0.20	13.0	315	100	5.25	1.43	1.79	1.43	1.09
29		6PV1	35x35	2.00	0.20	13.0	315	100	5.25	1.43	1.79	1.43	1.09
30	Melo et al. (2012) [41]	IPA-1 sup.	30x30	1.25	0.24	21.5	405	100	3.60	0.89	1.12	0.89	0.81
31		IPA-1 inf.	30x30	1.25	0.24	21.5	405	100	4.00	0.99	1.24	0.99	0.90
32		IPA-2 sup.	30x30	1.25	0.16	30.9	405	100	3.90	0.82	1.03	0.82	0.84
33		IPA-2 inf.	30x30	1.25	0.16	30.9	405	100	4.80	1.01	1.27	1.01	1.03
34		IPB sup.	30x30	1.25	0.21	24.5	405	30	4.20	1.10	1.74	1.38	0.98
35		IPB inf.	30x30	1.25	0.21	24.5	405	100	4.70	1.10	1.37	1.10	1.03
36		IPD sup.	30x30	1.25	0.27	18.5	405	30	4.40	1.33	2.10	1.66	1.66
37		IPD inf.	30x30	1.25	0.27	18.5	405	100	4.20	1.13	1.41	1.13	0.98
38		IPE sup.	30x30	1.25	0.24	21.2	405	100	4.40	1.10	1.38	1.10	0.99
39		IPE inf.	30x30	1.25	0.24	21.2	405	100	4.50	1.13	1.41	1.13	1.02
40		IPF sup.	30x30	1.25	0.22	22.5	405	100	4.10	1.00	1.24	1.00	0.92
41		IPF inf.	30x30	1.25	0.22	22.5	405	100	4.80	1.17	1.46	1.17	1.07
42	Current experimental results	CPA-1	30x30	1.70	0.16	21.2	405	100	3.21	0.66	0.82	0.66	0.56
43		CPA-3	30x30	1.70	0.19	17.4	405	100	4.53	1.01	1.26	1.01	0.83
44		CPB	30x30	1.70	0.17	20.3	405	30	4.26	0.96	1.52	1.20	0.79
45		CPC	30x30	1.70	0.20	17.1	405	100	4.97	1.11	1.39	1.11	0.91
46		CPD	30x30	1.70	0.19	18.0	405	30	4.07	0.97	1.53	1.21	0.78
47		CPE	40x30	1.70	0.19	18.0	405	100	4.43	1.07	1.34	1.07	0.89
48		CPF	50x30	1.70	0.18	18.3	405	100	3.50	0.90	1.13	0.90	0.74
						Mean for $l_0/d_{bL} \geq 30$ (i.e. test # 6 to 48)			4.37	1.11	1.43	1.15	1.00
						CoV for $l_0/d_{bL} \geq 30$ (i.e. test # 6 to 48)			0.26	0.25	0.26	0.25	0.22

Note: 1m = 100cm = 39.4in; 1MPa = 0.145ksi

Table 3.4 summarises the experimental ultimate chord rotation ($\theta_{u,exp}$) observed in recent studies [6,7,31-39,41] and the results obtained in the present experimental campaign. Moreover, Table 3.4 presents the mean geometrical and mechanical characteristics of the specimens and the ratios between the experimental and the predicted ultimate rotation capacity computed according to: i) Corrigenda to EC8-3 [29], without the correction for plain reinforcing bars ($\theta_{u,exp}/\theta_{um}$); ii) Corrigenda to EC8-3 [29], considering the correction coefficient for plain bars ($\theta_{u,exp}/\theta_{u,EC8}$); iii) Ricci et al. [30] ($\theta_{u,exp}/\theta_{u,R.}$) proposal; and iv) a new correction coefficient to expression A.1 of Corrigenda EC8-3 [29] ($\theta_{u,exp}/\theta_{u,prop.}$), which is proposed in this chapter and explained in the section: proposed correction factor to EC8-3. The mean and coefficient of variation (CoV) values presented in Table 3.4 refer only to specimens with continuous reinforcement or with lap-splice length-to-bar diameter ratio larger than 30. For the computation of the ultimate rotation capacity according to EC8-3 expression ($\theta_{u,EC8}$), the conditions corresponding to elements with plain bars without seismic detailing (multiplying the correction coefficient by 1/1.2) were considered. For all the cases, the parameter γ_{el} of expression A.1 was taken equal to 1.0, since the rotation capacity comparisons refer to experimental results. For the column test results presented in this chapter, the experimental ultimate chord rotation is assumed equal to the drift value at the ultimate point.

3.4.3.2 Proposed correction factor to EC8-3

Figure 3.9 presents the uncorrected experimental-to-predicted ratio of the ultimate rotation as a function of the lap-splice length-to-bar diameter ratio for the 48 columns reported in Table 3.4. In Figure 3.9, the results produced by [6,7,31-39] are called as "other test results" and the results reported in this chapter plus the results presented in [41] are called "results". The predicted ultimate rotation capacity (θ_{um}) was computed according to EC8-3 [29] without considering the correction for plain reinforcing bars. Figure 3.9 also shows the correction coefficients for RC elements with plain bars presented in EC8-3 [29] and the correction coefficient proposed by Ricci et al. [30].

From Figure 3.9 a high dispersion of results is observed both for specimens with continuous reinforcing bars and for specimens with lapping. The correction coefficient proposed by Ricci et al. [30] provides a better prediction of the ultimate rotation capacity than the expression in Corrigenda of EC8-3 [29]. The normal distribution adjusted to the

data presented in Figure 3.9 for elements without lapping show that 17% of the available results have lower ultimate rotation capacity than the EC8-3 predictions with the correction coefficient. Therefore, the EC8-3 correction coefficient appears to be conservative (compared with the average value), as is also stated by Verderame et al. [4] and Ricci et al. [30]. Considering all the available results for columns without lapping, the correction coefficient proposed by Ricci et al. [30] is slightly conservative, since the average uncorrected experimental-to-predicted ratio for ultimate rotation is 1.13.

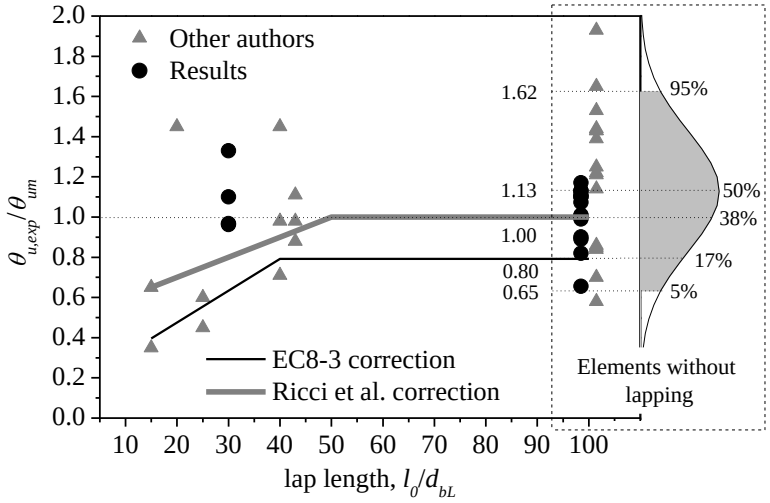

Figure 3.9 – Comparison between the correction coefficient present in Corrigenda of EC8-3 [29] and the proposed by Ricci et al. [30].

The large dispersion of the results presented in Figure 3.9 highlights the difficulty in estimating the ultimate rotation capacity for certain columns. The average uncorrected experimental-to-predicted ratio for columns with lap-splice length-to-bar diameter ratio equal or larger than 30 is 1.05 with CoV equal to 0.28, while for columns with continuous reinforcement the average value is 1.13 with CoV equal to 0.21. Therefore, the average values and the dispersion are similar, which justifies the eventual adoption of the same correction coefficient for columns with lap-splice length-to-bar diameter ratio equal or larger than 30 and for columns with continuous reinforcement. Moreover, the minimum lap-splice length considered in some old RC codes [15,16] is 30 times the bar diameter and thereby lower lap-splice lengths were not a common practice in the past. For these reasons, the authors consider that the same correction coefficient may be applied in columns without lapping and in columns with lap-splice length-to-bar diameter ratio equal or larger than 30. Still, the correction coefficient should take into account other parameters for better predictions, and to reduce the dispersion in the results.

$$a_{slip} = -0.055 \times \left(\upsilon^{1/2} \cdot f_c \cdot {L_V}^{1/3} \right) + 1.72 \quad (3.10)$$

With the aim of reducing the uncorrected experimental-to-predicted ratio dispersion, a new empirical expression (3.10) is proposed for the calculation of the correction coefficient (a_{slip}) of expression A.1 present in Corrigenda of EC8-3 for columns built with plain reinforcing bars. The new expression is a function of the axial load ratio (υ), the concrete compressive strength (f_c) and the shear span (L_V). To derive expression (3.10), the last 42 experimental results presented in Table 3.4 were used in order to better represent both columns with continuous bars and columns with lap-splice length-to-bar diameter ratio equal or larger than 30. For specimens with lap-splices, the lapping length should be subtracted from the estimate of the shear span length. Table 3.4 shows the uncorrected experimental-to-predicted ratio ($\theta_{u,exp}/\theta_{u,prop.}$) taking into account the a_{slip} correction coefficient proposed here. The proposed a_{slip} coefficient reduces the CoV of the uncorrected experimental-to-predicted ratio to 15% and 16%, relatively to the ultimate capacity predictions with the correction coefficients values given by Ricci et al. [30] and Corrigenda to EC8-3 [29], respectively. Moreover, as seen in Table 3.4, the average of the uncorrected experimental-to-predicted ratio obtained with expression (10) is 1.00. It is observed that in some cases, a_{slip} is greater than 1.0, i.e. the ultimate rotation capacity of columns built with plain bars is larger than that corresponding to columns built with deformed bars. This phenomenon has also been observed by other authors [42].

Figure 3.10 shows the relationship between the experimental ultimate rotation capacity of the last 42 tests presented in Table 3.4 and the corresponding predicted ultimate rotation. Each plot corresponds to a different prediction of the ultimate rotation capacity for the 42 columns. The first and second predictions were calculated according to expression A.1, without considering and considering the correction coefficient for plain reinforcing bars, respectively. The third prediction was computed according to the proposal of Ricci et al. [30]. Finally, the fourth case results from the adoption of the here proposed a_{slip} correction coefficient in expression A.1.

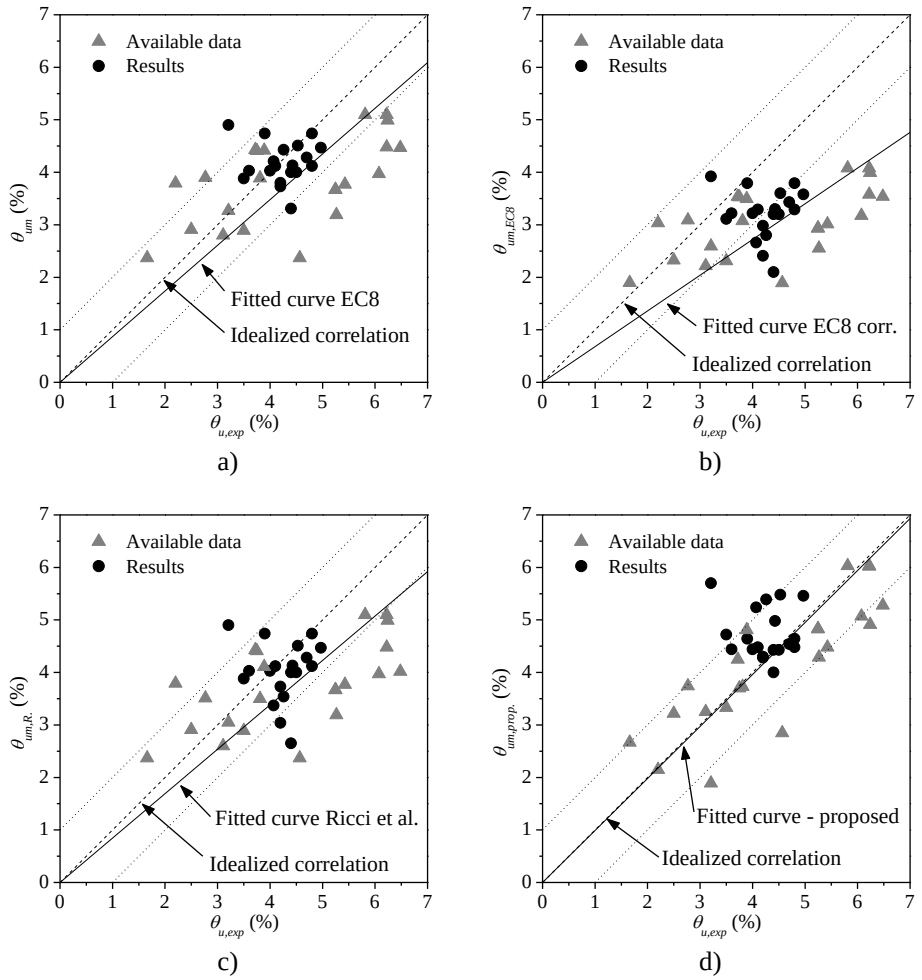

Figure 3.10 – Prediction of the ultimate rotation capacity of columns with different correction coefficients: a) Corrigenda EC8 [29]; b) Corrigenda EC8 [29] considering the plain bars correction; c) Ricci et al. [30] correction; and d) proposed correction.

The plot of the fourth case (Figure 3.10-d) confirms the lower dispersion obtained when the new expression is used to correct the ultimate rotation capacity given by expression A.1. Moreover, the fitted curve in the fourth case is almost coincident with the idealized correlation between the experimental and the predicted ultimate rotation (with slope equal to 1.0). Once again, it is demonstrated that the proposed correction coefficient might reduce the dispersion of the predicted ultimate rotation relatively to the experimental results. This analysis confirms that the proposed correction coefficient may better predict the ultimate rotation capacity for columns with continuous plain reinforcing bars and for columns with lap-splice length-to-bar diameter ratio equal or larger than 30, than Corrigenda EC8 [29] or Ricci et al. [30]. However, it is highlighted here that the number of available test results for columns with short lap-splice length (length-to-bar diameter ratio

lower than 30) is small (5). This number of tests is insufficient to support the proposal of a new empirical correction coefficient for this type of columns.

3.4.4 Damage state

For all specimens, the damage observed during the tests was associated to flexural response, and no shear cracks occurred. Two different failure modes were observed, namely concrete cover spalling followed by buckling of the longitudinal reinforcing bars, and large bar slippage. Buckling occurred due to the poor confinement associated to the large stirrup spacing (as was common practice in the past). The bar slippage increases the curvature demands in the plastic hinge region. As a consequence, for specimens with plain bars, cover spalling and bar buckling start earlier than for the specimen with deformed bars.

Figure 3.11 illustrates the damage pattern observed for each specimen at the end of the test. The first flexural crack is, generally, aligned with a stirrup due to the discontinuity created in the concrete by the stirrups. In specimens with lap-splice (CPB and CPD) concrete spalling along the lap-splice length was observed. Also, for these specimens a larger number of cracks were observed (particularly for specimen CPD) in the plastic hinge region, when compared with the other specimens. Specimens without lap-splice showed concrete spalling approximately along a length of 0.27m (10.6in) measured from the base of the column. In the specimens with larger section depths (CPE and CPF), the concrete spalling was not limited to the detachment of the concrete cover but includes part of the concrete column core. Specimen CPA-1 showed larger damage in the plastic hinge region than the reference specimen due to the local discontinuity introduced at the cold joint, which increases the curvature demands at the column base. Specimens with lap-splices (CPB and CPD) developed damage along the entire lap-splice length (0.36m – 14.2in). Also, they experienced higher levels of damage in the concrete at the plastic hinge region when compared to the specimens without lap-splice due to the stress concentration in the concrete surrounding the anchorage hooks. Specimens CPB and CPD have the same detailing of the lapping bars, but they differ in terms of steel amount (CPB with six bars and CPD with eight bars). A larger amount of longitudinal cracks was observed for specimen CPD (with larger steel amount) in the plastic hinge region, associated to the larger force transferred from the steel reinforcement to the concrete, which then fails in

compression in the lap-splice zone. For the reference specimen (CPA-3), with plain reinforcing bars, the damage observed was more concentrated at the column base when compared with the column with deformed steel (specimen CD). For the latter, damage was distributed along a length equal to the section depth. Evident buckling of the reinforcing bars was observed in all specimens except for specimens CPA-2 and CPB. Where it occurred, buckling was observed to start at drift values ranging from 2.5% (for specimen CPA-1) to 5.0% (for specimen CPD), as shown in Figure 3.3.

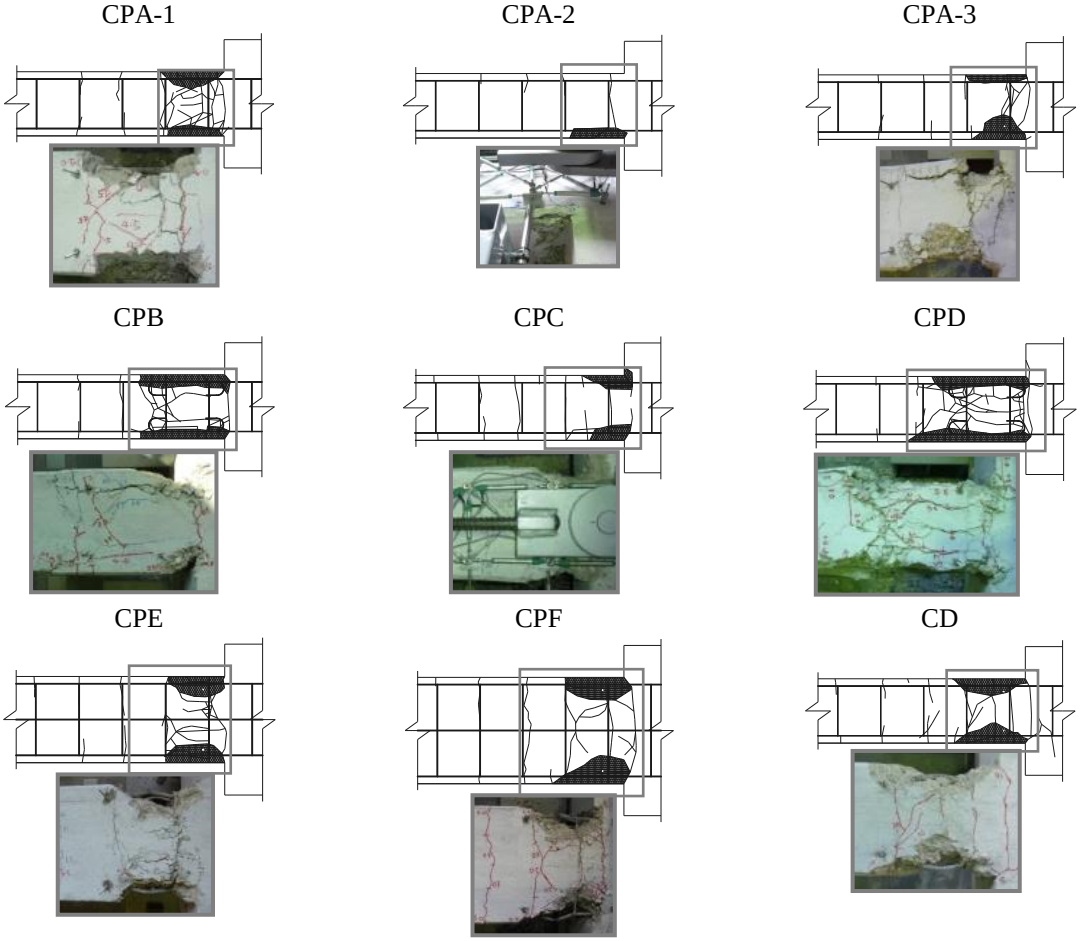

Figure 3.11 – Damage state at the end of the tests (top face of the specimens).

3.4.5 HRC-damage index

Rossetto and Elnashai [19] developed a damage scale called homogenised reinforced concrete damage scale (HRC-scale). The HRC-scale was designed to be used to generate vulnerability curves but was calibrated to large scale experimental data (see Rossetto 2004 [43]). This scale is subdivided into seven damage states. It is defined according the typical structural and non-structural damage expected in ductile, non-ductile and infilled RC

moment resisting frames (MRF) and in RC shear-wall structures (see Table 3.5 for non-ductile MRF). The limit states are defined in terms of a damage index, called HRC-damage index (DI_{HRC}), which provides a numerical reference scale for experimental calibration with the structural response parameter of maximum inter-storey drift ratio ($ISD_{max\%}$, expressed in percentage). For non-ductile MRF, the HRC-damage scale is given by Equation (3.11) proposed in [19]. Equation (3.11) was developed based on published experimental results of 25 dynamic tests and validated and updated using the published results of two pseudo-dynamic tests of full-scale frames.

For non-ductile MRF:

$$DI_{HRC} = 34.89Ln(ISD_{\max\%}) + 39.39 \tag{3.11}$$

Table 3.5 – Typical damage expected in non-ductile MRF according to HRC-scale [19].

DI_{HRC}	Damage State	Damage expected
0	**None**	No damage
10	**Slight**	Fine cracks in plaster partitions/infills
20	**Light**	Start of structural damage
30		Hairline cracking in beams and columns near joints (<1mm)
40		
50	**Moderate**	Flexural & shear cracking in most beams & columns
60		Yielding in a limited number of beams & columns
70		Shear cracking & spalling is limited
80	**Extensive**	Loss of bond at lap-splices, bar pull-out, broken ties
90		Main re-bar may buckle or elements fail in shear
100	**Partial Collapse**	Shear failure of many columns or impending soft-storey failure
	Collapse	Complete or soft-storey failure at ground floor

Figure 3.12 shows the HRC-damage index curve for non-ductile MRF obtained by Equation (3.11) and the experimental observations. For each point in the plot, the lower boundary value of the corresponding damage state is taken, because the damage index thresholds are what were used in the calibration of the HRC-scale. Therefore, the HRC-damage index values adopted for the damages observed in the tests such as cracking, cover spalling, buckling of the bars and ultimate points were 20, 60, 80 and 90, respectively.

In generic terms, the DI_{HRC} curve is in good agreement with the experimental observations for RC columns built with plain bars, particularly for the ultimate points. In the tests, cracking in the column was observed for lower drift levels than the values predicted by Equation (3.11), and the cover spalling and bar buckling were observed for

larger drift levels. However, the discrepancy between experimental observations and analytical predictions is not very significant. The average drift of the ultimate point observed for all columns experimentally studied is almost coincident with the analytically predicted value. Therefore, the DI_{HRC} curve can be used to define the limit states in the HRC-scale of this type of elements. According to the HRC-scale for non-ductile MRF: the experimentally observed cracking corresponds to the light damage state; cover spalling corresponds to the moderate damage state; buckling to the extensive damage state; and, the ultimate point corresponds to the partial collapse of the structure associated to the collapse of the columns, i.e. impending soft-storey failure of the structure.

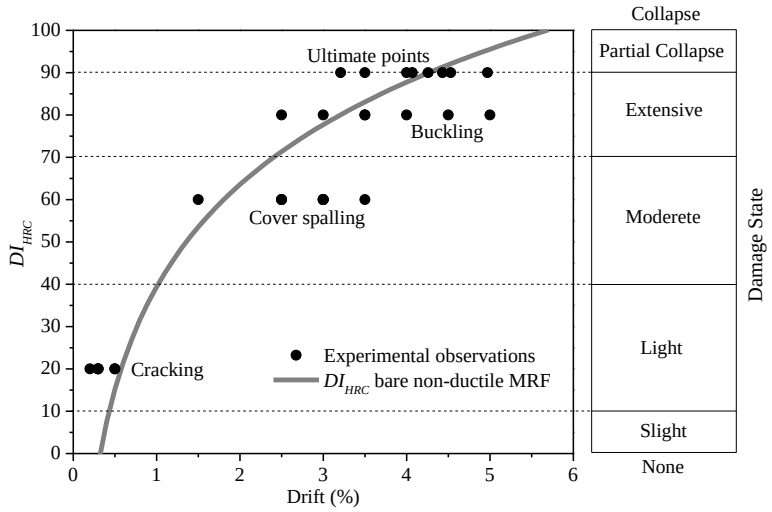

Figure 3.12 – HRC-damage index curve and experimental observations.

3.4.6 Displacement components

While the lateral displacement is imposed at the top of the column, different mechanisms contribute to the displacement of the column, such as: i) bending; ii) shear; and iii) slip. In the analysis here developed, the bending displacement is divided in two components, a) linear elastic and b) non-linear. The bending displacement component called elastic bending is analytically computed with the direct integration method, assuming a linear distribution of moments and curvatures along all the column length. The linear curvature distribution is given by a fitted straight line/function to the curvatures experimentally measured in the portion of the column where no damage is observed (slices 4, 5 and 6 according to Figure 3.2d), and assuming zero curvature at the top of the column. The bending component called "non-linear effects" intends to represent the displacement associated to the damage induced by bending as concrete flexural cracks, concrete spalling

and bars buckling. The lateral displacement component associated to the non-linear bending effects is computed subtracting from the total displacement the components due to shear displacement, elastic bending and slippage.

The shear displacement was computed assuming an elastic shear modulus (G) equal to 7.25GPa (1052ksi) and linear distortion distribution along the length of the column. The elastic shear modulus was computed considering the Young's modulus of the concrete and a Poisson's ratio equal to 0.2. In this study, it is assumed that slippage between the reinforcing bars and surrounding concrete does not occur for the specimen built with deformed bars (specimen CD) until its maximum strength is reached. Until the maximum strength of each column with plain bars, the slip displacement is estimated as the difference of the corresponding top displacement and the value for specimen CD for the same force level (absolute lateral force F_c). As the slip displacement in specimens with plain bars is estimated based on the corresponding experimental results for specimen CD, it was calculated only for columns with the same reinforcing amount, cross-section dimensions and loading history, i.e. specimens CPA-3 and CPB. As in this study the slip deformation is computed assuming no slippage for specimen CD, this means that the real slip deformation for the specimens with plain reinforcing bars may be even larger than shown in Figure 3.13.

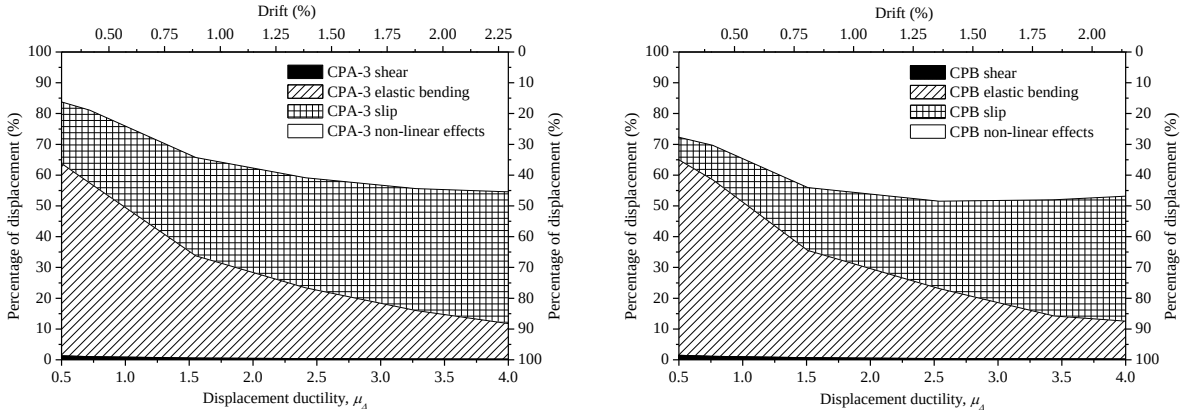

Figure 3.13 – Top displacement components for specimens: a) CPA-3; and b) CPB.

Figure 3.13 presents, for specimens CPA-3 and CPB, the lateral displacement components in terms of shear, elastic bending, slip and non-linear displacement, relative to the total displacement. The relative displacement due to slippage increases with the lateral displacement demand, ranging from 18% to 43% for specimen CPA-3 and from 7% to

40% in specimen CPB. For lower demands, the slippage component is observed to be larger in specimen CPA-3 than in specimen CPB, but for larger displacement demands the slip displacement observed was similar in both specimens. So, with the lap-splice the slippage effect is delayed for lower lateral drift demands. For displacement ductility higher than 1.5, the slip contribution to the total displacement becomes more significant. The elastic bending and shear displacement components were analogous in both specimens. This is expected as the material properties and geometric characteristics of both columns are similar. The shear component of displacement is small, varying from 2.5% at the beginning of the tests to 0.25% at the maximum column strength, presenting an approximately linear variation with the imposed drift. For both cases, the displacement corresponding to the elastic bending component is approximately 62% of the total displacement up to displacement ductility demands of 0.5 (~0.3% drift). It drops to 30% at displacement ductility equal to 1.5 (~0.8% drift) and then decreases until 12% at the column maximum strength (~2.3% drift). The non-linear effects represent 16% and 27% of the total displacement at a 0.25% drift demand for specimens CPA-3 and CPB, respectively. The non-linear effects increases up to approximately 45% of the total displacement at the maximum column strength (~2.3% drift).

3.5 CONCLUSIONS

The experimental campaign developed on full-scale columns confirmed that the cyclic behaviour of RC elements with plain reinforcing bars and poor reinforcing detailing might be poorer than RC elements with deformed reinforcing bars. The reinforcing detailing adopted in the experimental campaign was based in the old Portuguese codes specifications, which are representative of element detailing in existing buildings in European Mediterranean countries until the 1970s. The influence of bond properties, lapping, cold joint, steel reinforcing amount, cross-section dimensions and lateral loading type were investigated. From the analysis of the experimental results, and from the comparison with results from other authors, the following conclusions can be drawn:

- The presence of lap-splices in elements decreased the dissipated energy, increased the damages at the plastic hinge zone and the pinching effect, for the same level of demand. For columns with larger reinforcement amounts and lapping, the concrete

may experience failure in compression in the vicinity of the lapping bar end due to the concentration of stresses transferred by the hook;

- The strength reduction observed in the monotonic test after the peak strength was lower than obtained in the cyclic tests, as expected. In the monotonic test, the conventional ultimate point was not achieved at the end of the test (9% drift). However, in similar tests performed by [5,42], limited strength reduction was observed and the ultimate point was achieved in some specimens for a drift ranging from 6% to 8.5%;
- The maximum strength of the specimens tested, with and without lapping, were reached for a drift demand value 40% and 85% larger than those obtained in similar tests reported in [5], respectively;
- The dissipated energy capacity and the equivalent damping of the specimens with plain bars were lower than the obtained for a similar specimen (CD) with deformed bars;
- The crack pattern observed in the specimen built with deformed bars (maximum crack width was 3.5mm, 0.14in) was spread over a larger portion of the column length than for the other specimen (CPA-3) built with plain bars (maximum crack width was 6.0mm, 0.24in). This conclusion is in agreement with observations made by other authors [2,42];
- Columns with larger cross-section dimensions revealed a more pronounced pinching, and dissipated less energy than other columns with similar reinforcing detailing but with smaller cross-section;
- The flexural strength capacity given by EC2-1-1 expressions estimates the experimental results for the specimen with deformed bars better (difference of 1.9%). For the columns built with plain reinforcing bars, EC2-1-1 in some cases overestimates the flexural strength capacity (15% for specimen CPD) and in other cases underestimates it (9% for specimen CPC);
- The available equations for the equivalent damping estimation of RC elements with deformed bars did not match the experimental results well for the tested elements with plain bars. All of the checked expressions overestimated the equivalent damping. The

expressions derived by other authors [2,23] based on test results carried out on elements and structures built with plain bars are in better agreement with the experimental results obtained in this work;

- The correction coefficient for the expression A.1, presented in Corrigenda to EC8-3, to take into consideration the bond properties in elements with plain reinforcing bars is conservative. Also, a large dispersion of the results was observed. The correction coefficient proposed by Ricci et al. [30] is less conservative than that included in Corrigenda to EC8-3, but the dispersion of the results observed is still large;
- The a_{slip} correction coefficient is proposed in this chapter, which reduces the results' dispersion and does not underestimate the ultimate rotation capacity;
- The HRC-damage index curve, calibrated for RC structures built with deformed reinforcing bars, represents the experimental observations well, and might also be used for RC elements built with plain reinforcing bars;
- The slippage effect on RC columns with plain reinforcing bars can represent up to 43% of the total displacement imposed, compared to similar specimens with deformed bars.

This chapter provides a significant contribution to the state-of-the-art knowledge on the behaviour of RC elements reinforced with plain bars. Firstly it increases the limited available experimental data on RC elements with plain bars. The experiments demonstrated the large slippage contribution to the column drift and confirmed some of the observations made by other authors. Secondly, the chapter proposes a new correction factor for the ultimate rotation capacity computed according to expression A.1 present in Corrigenda to EC8-3 [29].

3.6 REFERENCES

[1] CEB. RC elements under cyclic loading. State-of-the-art report. Thomas Telford Publications (Editor). 1996. ISBN 0727720864.

[2] Fernandes C. Cyclic behaviour of RC elements with plain reinforcing bars. PhD Thesis. University of Aveiro. Aveiro. Portugal, 2012.

[3] Melo J, Fernandes C, Varum H, Rodrigues H, Costa A, and Arêde A. Numerical modelling of the cyclic behaviour of RC elements built with plain reinforcing bars. *Engineering Structures* 2011:33(2):273-286.

[4] Verderame GM, Ricci P, Manfredi G, Cosenza E. Ultimate chord rotation of RC columns with smooth bars: Some considerations about EC8 prescriptions. *Bulletin of Earthquake Engineering* 2010:8(6):1351-1373.

[5] Verderame GM, Fabbrocino G, Manfredi G. Seismic response of RC columns with smooth reinforcement. Part I: monotonic tests. *Engineering Structures* 2008:30(9):2277-2288.

[6] Verderame GM, Fabbrocino G, Manfredi G. Seismic response of RC columns with smooth reinforcement. Part II: cyclic tests. *Engineering Structures* 2008:30(9):2289-2300.

[7] Di Ludovico M, Verderame GM, Prota A, Manfredi G, Cosenza E. Experimental Investigation on Non-Conforming Full Scale RC Columns. Proceedings of the XIII Conference ANIDIS. Bologna. Italy. 2009 Paper S02_09. (CD-ROM).

[8] Fernandes C, Melo J, Varum H, Costa A. Cyclic behaviour of substandard RC beam-column joints with plain bars. *ACI Structural Journal* 2013:110(1):137-148.

[9] Bedirhanoglu I, Ilki A, Pujol S, Kumbasar N. Behavior of Deficient Joints with Plain Bars and Low-Strength Concrete. *ACI Structural Journal* 2010:107(3):300-10.

[10] Liu A, Park R. Seismic Behaviour and Retrofit of Pre-1970's As-Built Exterior Beam-Column Joints Reinforced by Plain Round Bars. *Bulletin of the New Zealand Society for Earthquake Engineering* 2001:34(1):68-81.

[11] Marefat M, Shirazi S, Rostamshirazi R, Khanmohammadi M. Cyclic response of concrete beams reinforced by plain bars. *Journal of Earthquake Engineering* 2009:13:463-481.

[12] Fernandes C, Melo J, Varum H, Costa A. Cyclic behavior of a two-span RC beam built with plain reinforcing bars. *Periodica Polytechnica Civil Engineering* 2011:55(1):21-29.

[13] Verderame GM, Ricci P. Carlo GD, Manfredi G. Cyclic Bond Behavior of Plain Bars. Part I: Experimental Investigation. *Construction and Building Materials* 2009:23(12):3499-3511.

[14] CEN. BS EN 1998-3:2005. Eurocode 8: Design of structures for earthquake resistance. Part 3: Strengthening and repair of buildings. European Committee for Standardization. Brussels. Belgium, 2005.

[15] Governo D. Regulamento do Betão Armado (RBA), Decreto n.º 25948, 16 de Outubro, serie I, num. 240, Lisbon, 1935. (in Portuguese)

[16] Governo D. Regulamento de Estruturas de Betão Armado (REBA), Decreto n.º 47723, 20 de Maio, serie I, num. 119, Lisbon, 1967. (in Portuguese)

[17] CEN. EN ISO 6892-1:2009. Metallic materials – Tensile testing – Part 1: Method of test at ambient temperature. European Committee for Standardization. Brussels. Belgium, 2009.

[18] IPQ. NP EN 12390-3:2011, Ensaios do betão endurecido. Parte 3: Resistência à compressão de provetes. Instituto Português da Qualidade, Caparica, Portugal, 2011. (in Portuguese)

[19] Rossetto T, Elnashai A. Derivation of vulnerability functions for European-type RC structures based on observational data. *Engineering Structures* 2003:25(10):1241-1263.

[20] CEN. NP EN 1992-1-1. Eurocode 2: Design of concrete structures. Part 1-1: General rules and rules for buildings. European Committee for Standardization. Brussels. Belgium, 2010.

[21] Park YJ, Ang AHS, Wen YK. Damage-limiting aseismic design of buildings. *Earthquake Spectra* 1987:3(1):1-26.

[22] Priestley M, Calvi G, Kowalsky M. Displacement-Based Seismic Design of Structures. IUSS PRESS. Italy, 2007.

[23] Varum, H. Seismic assessment, strengthening and repair of existing buildings. PhD Thesis, University of Aveiro. Aveiro. Portugal, 2003.

[24] CEN. EN 1998-1:2004. Eurocode 8: Design of structures for earthquake resistance – Part 1: General rules, seismic actions and rules for buildings. European Committee for Standardization. Brussels, 2004.

[25] Blandon C. Priestley MNJ. Equivalent viscous damping equations for direct displacement based design. *Journal of Earthquake Engineering* 2005:9(2):257-278.

[26] Gulkan P, Sozen MA. Inelastic responses of reinforced concrete structures to earthquakes motions. Proceedings of the ACI 71 (12), 1974.

[27] Kowalsky MJ, Ayers JP. Investigation of equivalent viscous damping for direct displacement-based design. PEER-2002/02. The Third US-Japan Workshop on Performance-Based Earthquake Engineering Methodology for Reinforced Concrete Building Structures. 16-18 August 2001. Seattle. Washington. Berkeley: Pacific Earthquake Engineering Research Center. University of California, 2002. pp. 173-185.

[28] Priestley MJN. Myths and fallacies in earthquake engineering, revisited. The Mallet Milne Lecture. IUSS Press. Pavia. Italy, 2003.

[29] CEN. Corrigenda to EN 1998-3. Document CEN/TC250/SC8/N437A. European Committee for Standardization. Brussels. Belgium, 2009.

[30] Ricci P, Verderame G, Manfredi G. ASCE/SEI 41 Provisions on Deformation Capacity of Older-Type Reinforced Concrete Columns with Plain Bars. *Journal of Structural Engineering* 2013:13(12). doi: 10.1061/(ASCE)ST.1943-541X.0000701.

[31] Bousias S, Spathis AL, Fardis MN. Seismic retrofitting of columns with lap spliced smooth bars through FRP or concrete jackets. *Journal of Earthquake Engineering* 2007:11(5):653-674.

[32] Bournas DA, Lontou PV, Papanicolaou CG, Triantafillou TC. Textile-Reinforced Mortar versus Fiber-Reinforced Polymer confinement in reinforced concrete columns, *ACI Structural Journal* 2007:104(6):740-748.

[33] Faella C, Napoli A, Realfonzo R. Cyclic flexural behavior of FRP-confined concrete columns under high axial loading, Proceedings of the ReLUIS congress Valutazione e riduzione della vulnerabilità sismica di edifici esistenti in c.a.. Rome. Italy. May 29-30, 2008. pp. 510-520.

[34] Marefat MS, Arani KK, Hassanzadeh Shirazi SM, Amrollahi-Biucky A. Seismic behavior and retrofit of concrete columns of old R.C. buildings reinforced with plain bars. Proceedings of Seismic Engineering Conference Commemorating the 1908 *Messina and Reggio Calabria Earthquake* 2008:1020:1554-1562. doi: 10.1063/1.2963783.

[35] Ozcan O, Binici B, Ozcebe G. Improving seismic performance of deficient reinforced concrete columns using carbon fiber-reinforced polymers, *Engineering Structures* 2008:30(6):1632-1646.

[36] Bournas DA, Triantafillou TC. Flexural strengthening of reinforced concrete columns with Near-Surface-Mounted FRP or stainless steel. *ACI Structural Journal* 2009:106(4)495-505.

[37] Arani KK, Marefat MS, Amrollahi-Biucky A, Khanmohammadi M. Experimental seismic evaluation of old concrete columns reinforced by plain bars. *The Structural Design of Tall and Special Buildings* 2010:22:267-290. doi: 10.1002/tal.686.

[38] Ozcan O, Binici B, Ozcebe G. Seismic strengthening of rectangular reinforced concrete columns using fiber reinforced polymers. Engineering Structures 2010;32(4):964-973.

[39] Acun B, Sucuoglu H. Performance of reinforced concrete columns designed for flexure under severe displacement cycles. *ACI Structural Journal* 2010:107(3):364-371.

[40] Ilki A, Tezcan A, Koc V, Kumbasar N. Seismic retrofit of non-ductile rectangular reinforced concrete columns by CFRP jacketing. Proceedings of the 13th World Conference on Earthquake Engineering. Vancouver. B.C. Canada. August 1-6. 2004. Paper No. 2236.

[41] Melo J, Varum H, Rossetto T, Costa A. Cyclic response of RC beam-column joints reinforced with plain bars: An experimental testing campaign. Proceedings of the 15th World Conference on Earthquake Engineering. Lisbon. Portugal. 24-28 September. 2012. Paper No. 4799.

[42] Di Ludovico M, Verderame G, Prota A, Manfredi G, Cosenza E. Cyclic Behavior of Non-Conforming Full Scale RC Columns, *Journal of Structural Engineering* 2014:140(5). doi: 10.1061/(ASCE)ST.1943-541X.0000891.

[43] Rossetto T. Vulnerability curves for the seismic assessment of reinforced concrete building populations. PhD Thesis. Imperial College London. London. UK, 2004.

CHAPTER 4

CYCLIC BEHAVIOUR OF INTERIOR BEAM-COLUMN JOINTS REINFORCED WITH PLAIN BARS

Melo, J., Varum, H., Rossetto, T. (in press) Cyclic behaviour of interior beam-column joints reinforced with plain bars. *Earthquake Engineering and Structural Dynamics*, http://dx.doi.org/10.1002/eqe.2521.

4.1 ABSTRACT

The seismic damages commonly observed on beam-column joints of old reinforced concrete structures, built with plain bars and without proper detailing, justifies the need to further study the behaviour of this type of structures. The response of these structures when loaded cyclically, as occurs during the earthquakes, is partially controlled by the bond properties between the reinforcing bars and the surrounding concrete. This chapter presents the results of an experimental campaign of unidirectional cyclic tests carried out on six full-scale beam-column joints built with plain bars. These joint specimens are representative of existing reinforced concrete structures, i.e. built without adequate reinforcement detailing for seismic demands. For comparison, an additional specimen is built with deformed bars and tested. The seven specimens are designed and detailed so as to allow the investigation of the influence of bond properties, lapping of the longitudinal bars in columns and beams, bent-up bars in the beams, slab contribution and concrete strength. The lateral force-drift relationships, global dissipated energy evolution, contribution of the joint, beams and columns to the global dissipated energy, ductility, equivalent damping, final damage observed, HRC damage index, displacement components, curvature evolutions and Eurocode requirements are presented and discussed.

4.2 INTRODUCTION

Recent earthquakes [1,2] shows that failure of the bond mechanism between concrete and reinforcing bars and the poor confinement of the joints are common causes of severe damage, and even collapse, in existing reinforced concrete (RC) buildings built with plain bars. In RC structures designed and built before the 1970s, using plain reinforcing bars and prior to the enforcement of the modern seismic-oriented designed codes, the bond-slip phenomenon can constrain their seismic performance. The bond mechanism is responsible for the force transfer between reinforcing steel and the surrounding. The cyclic loads, such as those induced by earthquakes, cause progressive concrete-steel bond degradation, which can lead to significant bar slippage. As a consequence, the maximum strength of the structure may not be achieved and the deformation of the elements may increase, leading to the premature partial or total collapse of the structure. Studies available in the literature [3-5] indicate that the bond-slip mechanism has a significant contribution on the fixed-end rotations of RC elements, representing up to 80%~90% of the RC element overall deformability in the case of elements built with plain bars. Apart from the slippage phenomenon, the failure of old RC structures may be precipitated by other factors such as [6]: inadequate reinforcement detailing for seismic demands; lower concrete confinement level; lower compressive concrete strength; and designed only for gravity loads.

In recent, much research has been carried out on the design of new RC structures and the improvement of design codes [7,8,9,10,11,12,13]. Many fewer studies have focussed on the assessment and retrofitting of old RC structures [4,5,14,15,16,17,18,19,20], and knowledge on the cyclic behaviour of existing RC elements is still limited. Therefore, further research on the deformation and softening mechanisms of RC elements under cyclic loading are essential to better estimate the capacity and to develop retrofitting techniques for old RC structures.

In old RC structures, the beam-column joint connections are commonly damaged during earthquake ground motions due to poor confinement of the joint and bar slippage [2,21]. The joint strength and deformability influence the global behaviour of the overall structure when subjected to seismic demands. In order to improve the cyclic behaviour of the beam-column joints, analytical and empirical expressions to estimate their deformation

and strength capacity should be calibrated based on experimental test results on specimens that represent the materials properties, structural constrains and loading conditions.

This chapter presents the results of a series of cyclic tests carried out on six full-scale beam-column joints built with plain reinforcing bars. The specimens represent typical beam-column joints in existing RC buildings that do not conforms to current seismic code provisions and are built with plain reinforcing bars. An additional joint specimen with deformed reinforcing bars was built and tested as a reference. The main findings of this testing campaign, in terms of global and local response, are presented and discussed in the chapter, allowing the study of the influence on the cyclic response of beam-column joints of: bond properties; longitudinal reinforcement lapping on columns and beams; bent-up bars in the beams; slab contribution; and concrete strength.

4.3 SPECIMENS DETAILING, MATERIAL PROPERTIES AND TEST SETUP

4.3.1 Detailing of joint specimens

In the Department of Civil Engineering of the University of Aveiro an experimental campaign was carried out with the aim of characterizing the cyclic behaviour of interior RC beam-column joints in old building structures. Six full-scale beam-column joints built with plain reinforcing bars with different reinforcing detailing and one built with deformed reinforcing bars were tested under unidirectional lateral cyclic load up to rupture. Specimens were designed and detailed to assess the influence of: reinforcing steel surface, reinforcing steel detailing (lapping of longitudinal bars and bent-up bars in the beam), slab contribution and concrete strength. Moreover, the specimens are designed to present a weak column-strong beam mechanism and have inadequate shear transverse reinforcement detailing, in order to represent typical existing RC structures designed only for gravity loads, i.e. neglecting the lateral demands induced by seismic events.

The specimens represent interior beam-column joints at the first floor level of a 4 storey building and connect beams with span of 4.0m (157in) and columns that are 3.0m (118in) in height. In the nomenclature adopted for the specimens: i) the first letter (I) stands for Interior beam-column joint; ii) the second letter (P or D) refers to the reinforcing

steel type (plain, P, or deformed, D); iii) the third letter refers to a specific reinforcing detailing.

Figure 4.1 presents the geometry, dimensions and reinforcing details of the specimens. The reinforcing details of the plain bars were defined according to the first Portuguese codes for reinforced concrete structures, RBA (1935) [22] and REBA (1967) [23]. Thus, the anchorage of the longitudinal plain reinforcing bars consists in 180º end hooks. Also, the mandrel diameter and the straight prolongation after the hook are four times the corresponding bar diameter. For the specimen with deformed reinforcing bars, 90º end hooks with a 0.15m (5.9in) straight prolongation after the hook were adopted. The lap-splice length of the longitudinal plain reinforcing bars were also defined according to the recommendations of the first Portuguese RC codes, which equals 30 times the bar diameter. For all specimens, stirrups were anchored by 90º bends.

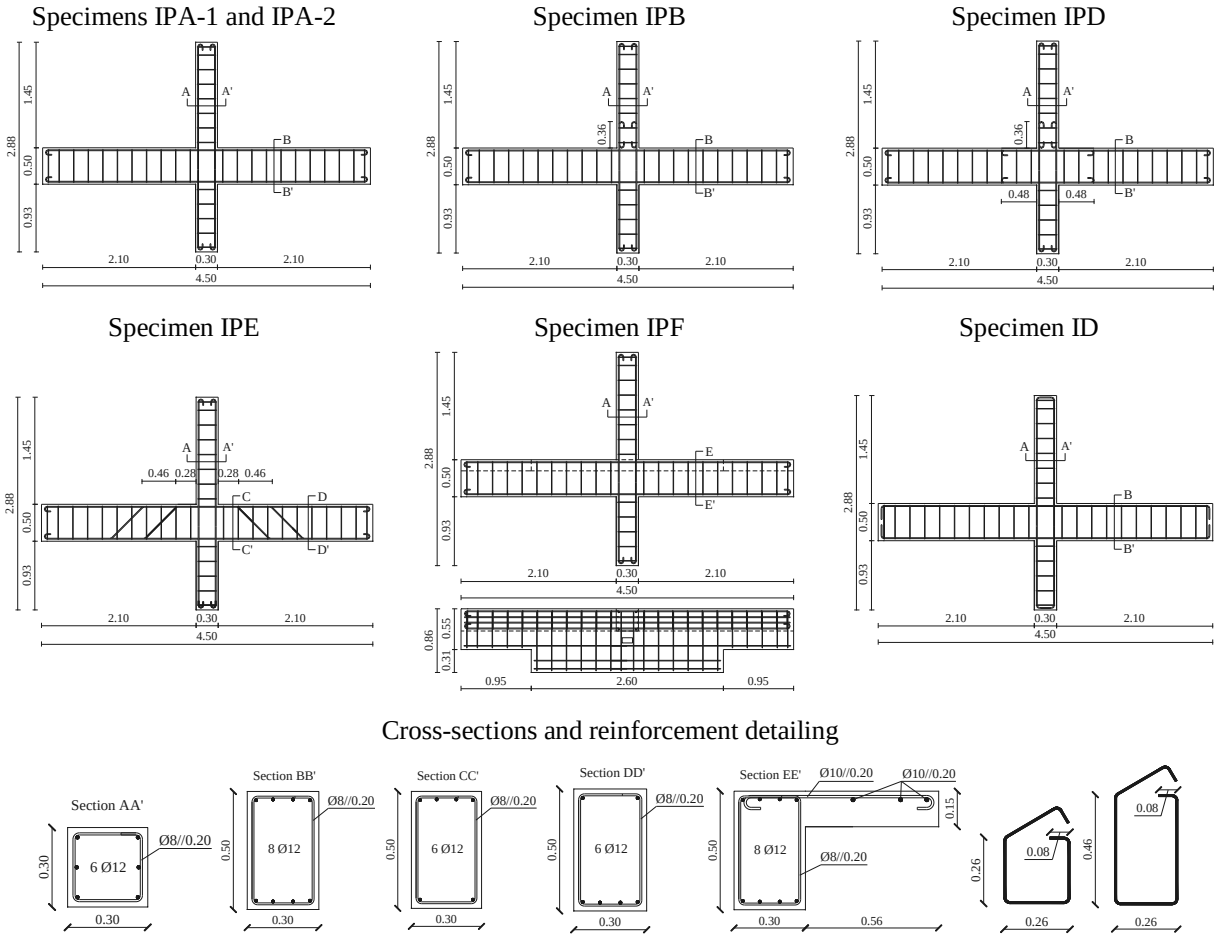

Note: Dimensions in meters (m). 1m=39.4in

Figure 4.1 – Specimens (geometry, dimensions and reinforcement detailing).

Specimens IPA-1 and IPA-2 have continuous longitudinal reinforcing bars, but specimen IPA-2 had a larger concrete strength. IPA-1 was chosen as the reference specimen, for the comparisons developed in this work. Specimens IPB and IPD contain lap-splices in the longitudinal reinforcing bars that are located at the base of the upper column (coincident with regions where plastic hinges may occur). In addition, specimen IPD contains lap-splices in the longitudinal bars of the beams at the hogging zone. The longitudinal reinforcing bars of specimen IPE are continuous, but some bars in the beams bent-up at 45º from the sagging zone to the hogging zone, as was commonly used in the past. Specimen IPF has the same reinforcement detailing as the reference specimen, but a slab was cast monolithically on one side of the beam. Specimen ID is analogous to specimen IPA-1 but was built with deformed reinforcing bars. Specimen IPC was built and tested to validate the test-setup, so the corresponding results are not discussed in the present chapter.

The longitudinal reinforcement of the columns consists of three bars with 12mm (0.47in) diameter in each lateral face. The longitudinal reinforcement of the beams for all specimens, except for specimen IPE, is constituted by four bars with 12mm (0.47in) diameter both in the upper and lower faces. The beams of specimen IPE are constituted by two and four bars with 12mm (0.47in) diameter in the lower and upper faces in the hogging zone, respectively. In the sagging zone, the reinforcement is constituted by four and two bars with 12mm (0.47in) diameter in the lower and upper faces, respectively. The shear reinforcement of the columns and beams is made by stirrups with 8mm (0.32in) diameter, spaced at 0.20m (7.87in) centres. None of the specimens contains stirrups in the core of the joint. Each specimen is casted in the horizontal position at different dates.

Hot-rolled plain and deformed bars are used for the specimen reinforcement, with grades A235 and A400NRSD for plain and deformed bars, respectively. Three tensile tests were performed on reinforcing bar samples following the procedure in standard EN ISO 6892-1 (2009) [24]. Concrete grade C16/20, according to EC-2 classification [25], was specified for the construction of the specimens, but the strength obtained after the compressive tests were lower than should be for C16/2o grade. Compressive tests on concrete cylinder samples were carried out according to the standard NP EN 12390-3 (2011) [26]. All concrete samples were tested simultaneously with the test of the corresponding beam-column joint specimen, and at least after 90 days of curing. Table 4.1 summarises the mean properties of the concrete and steel used in the construction of the

specimens, where f_{cm} is the concrete compressive strength of cylinder samples with dimensions 150mmx300mm (5.9inx11.8in), f_{ctm} is the tensile strength of concrete obtained by split-cylinder tests, f_{ym} is the yield strength of reinforcement steel, f_{um} is the ultimate tensile strength of reinforcement and E_{ym} is the Young's modulus of the reinforcement.

Table 4.1 – Concrete and steel mechanical properties (mean values).

Specimen	Concrete		Bar surface	Steel					
				Ø8 mm			Ø12 mm		
	MPa (ksi)			MPa (ksi)		GPa (ksi)	MPa (ksi)		GPa (ksi)
	f_{cm}	f_{ctm}		f_{ym}	f_{um}	E_{ym}	f_{ym}	f_{um}	E_{ym}
IPA-1	21.5 (3.12)	2.5 (0.36)	Plain	410 (59.5)	495 (71.8)	198 (28717)	405 (58.7)	470 (68.2)	199 (28863)
IPA-2	30.9 (4.48)	3.2 (0.46)							
IPB	24.5 (3.55)	3.5 (0.51)							
IPD	18.5 (2.68)	2.3 (0.33)							
IPE	21.2 (3.07)	2.4 (0.35)							
IPF	22.5 (3.26)	2.3 (0.33)							
ID	20.8 (3.02)	2.4 (0.35)	Deformed	470 (68.2)	605 (87.7)	198 (28717)	465 (67.4)	585 (84.8)	199 (28863)

4.3.2 Test setup, loading conditions and monitoring

General information regarding the loading conditions, lateral displacements history imposed, test-setup adopted and monitoring scheme are illustrated in Figure 4.2. The specimens are tested in the horizontal position. The axial load (N) is imposed by a hydraulic actuator placed at the top of the superior column associated to two tie rods linked to the base of the inferior column. To maintain the tie rods centred with the core joint during the cyclic test, two steel tubes are mounted at the base of the inferior column to extend the tie rods length. Therefore, the length of the tie rods in both sides of the joint (in the superior column and in the inferior column) is similar diminishing the second order effects at the columns' extremities. It is recognised that the axial load level may change the failure mode of the joint and column [27,28]. However, a constant axial load of 450kN (101kip) was applied for all cyclic tests that is a common value for columns at the foundation level for structures with four stories and with the typology present in Section 4.3.1. The cyclic tests are performed under displacement controlled conditions of the imposed lateral displacements. The displacements' history imposed consists in: three cycles applied for each of the following peak drift values (± %): 0.1, 0.2, 0.3 and then 0.5 to 4.0 with 0.5 increments (see Figure 4.2a). The lateral displacements are imposed with a velocity rate ranging from 0.1 for the first cycles to 1.5 mm/second (0.0039 to 0.059 in/second) for the last cycles.

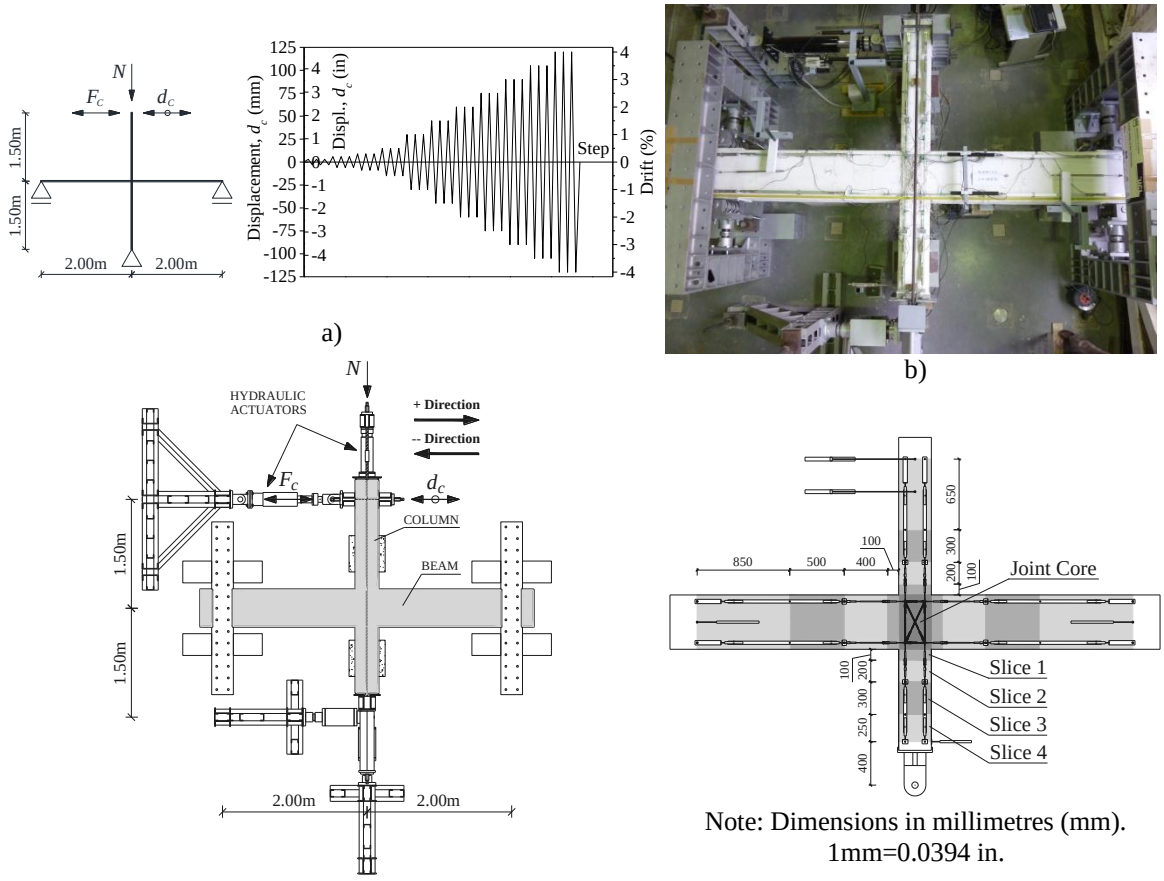

Figure 4.2 – Test setup and monitoring: a) support and loading conditions idealized and imposed lateral displacement history; b) general view; c) test setup schematics; and d) monitoring scheme.

The sensors arrangement is shown in Figure 4.2d. The global displacements evolutions are measured by Linear Variable Displacement Transducers (LVDTs) placed at the top and base of the columns, at the end of the beams and in the core joint. Twenty-two potentiometers (error < 0.05mm) and sixteen LVDTs (error < 0.025mm) are used for monitoring the relative displacements evolution in different points along the span of the elements.

4.4 EXPERIMENTAL RESULTS AND DISCUSSION

In this section are presented and discussed the experimental results in terms of: hysteretic force-drift diagrams, force-drift envelopes, hysteretic dissipated energy evolution, equivalent damping-displacement ductility relationship, damages, HRC damage index, drift components and joint shear strength. Comparisons of the response obtained for the specimens tested are made intending to evaluate the influence of: i) reinforcing steel

surface; ii) lapping of the longitudinal reinforcing steel bars; iii) bent-up bars in the beam; iv) slab contribution; and v) concrete strength. The damage patterns observed at the end of the tests are also compared.

4.4.1 Global force-drift response

The cyclic lateral force-drift response and the force-drift envelopes of the beam-column joints tested are presented in Figure 4.3 and Figure 4.4, respectively. In Figure 4.3, each plot includes the cyclic response of two specimens aiming to highlight the differences for each variable under study, namely: bond properties (IPA-1 versus ID); lap-splice of the column longitudinal reinforcing bars (IPA-1 versus IPB); lap-splice of the column and beam longitudinal reinforcing bars (IPA-1 versus IPD); bent-up of longitudinal reinforcing bars in the beam (IPA-1 versus IPE); slab contribution (IPA-1 versus IPF); and concrete strength influence (IPA-1 versus IPA-2). The onset of each type of damage is also represented in Figure 4.3, namely: cracking on beams, cracking on columns, cracking on the core joint, concrete cover spalling and bar buckling. Table 4.2 presents the values of the experimental response (for loading in the positive direction) corresponding to: maximum force ($F_{c,max}$), drift at maximum force ($Drift_{Fc,max}$), ultimate force ($F_{c,ult}$) and drift at ultimate force ($Drift_{Fc,ult}$). The ultimate point corresponds to a 20% strength reduction relatively to the maximum strength, as adopted by Park and Ang [29] and commonly used by the scientific community. Specimen ID was accidently loaded with a lateral displacement imposed corresponding to 1.5% drift in the positive direction before the imposition of the axial load. Few cracks on the superior columns and on the right beam were observed after this accidental load. Therefore, the initial stiffness of specimen ID was influenced by the initial damage inflicted accidently, but the global response is not significantly affected.

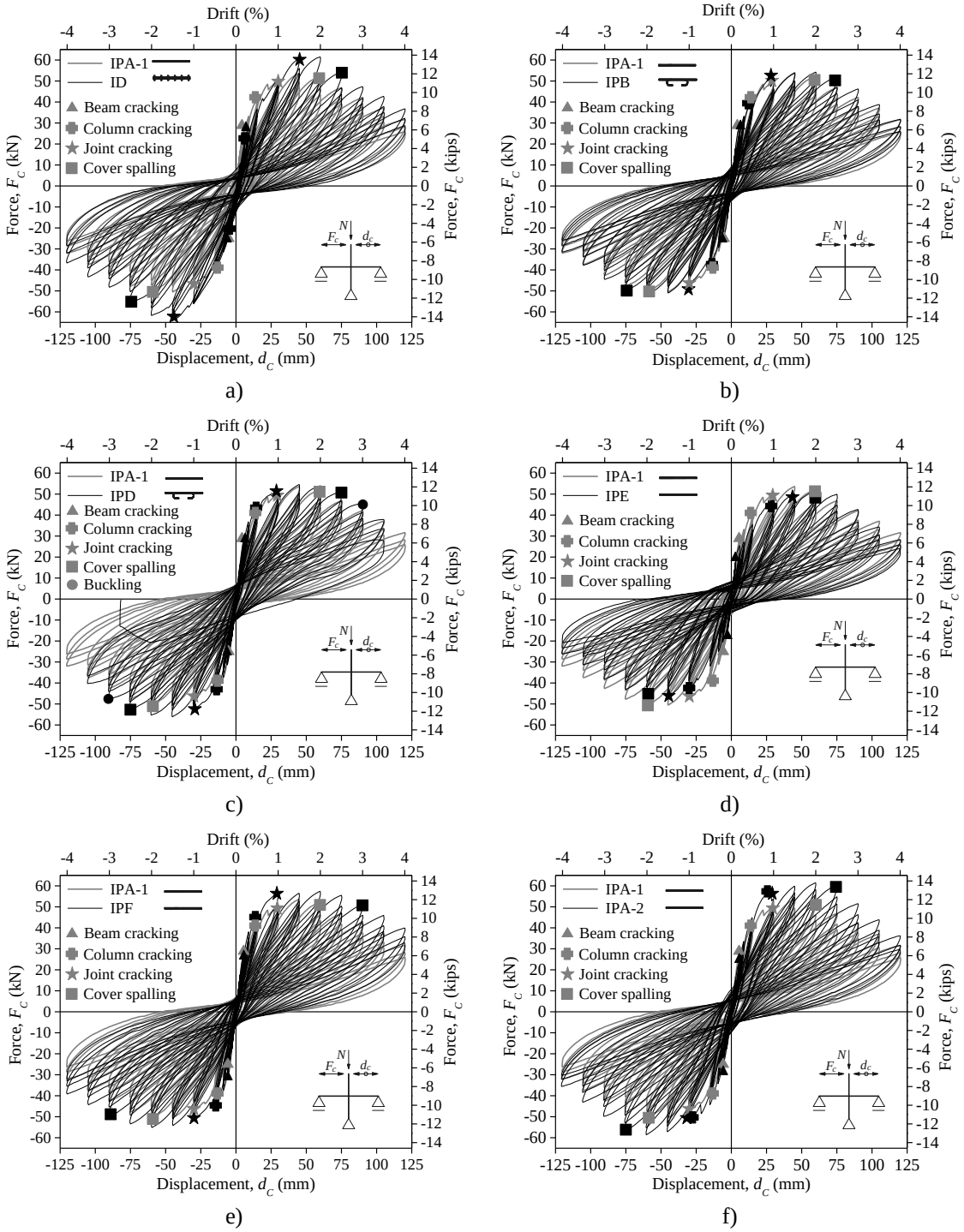

Figure 4.3 – Lateral force-drift relationships: a) IPA-1 versus ID; b) IPA-1 versus IPB; c) IPA-1 versus IPD; d) IPA-1 versus IPE; e) IPA-1 versus IPF; and f) IPA-1 versus IPA-2. (Note: 1mm = 0.0394in)

The cyclic response obtained for all specimens is almost symmetric, as expected due to the symmetry in terms of geometry and reinforcement detailing of the specimens. Among the specimens studied, ID developed the maximum strength due to the larger steel grade of deformed reinforcing bars relatively to the plain bars. The maximum strength of

specimen IPA-2 was larger than the strength obtained for similar specimens (IPA-1, IPB, IPD, IPF) due to its higher concrete grade. The initial stiffness was similar for all specimens and equal in both directions, except for specimen ID. Specimen ID presented larger stiffness in the negative direction than for specimens with plain bars, and smaller stiffness in the positive direction due to the damage induced with the accidental load. All specimens displayed also similar response in terms of unloading and reloading stiffness. Generically, cracking started at the beams for drift levels between 0.1% and 0.2% and then at the columns for drift levels between 0.2% and 1.0% once that the cracking moment in the beams is lower than in the columns due to the axial load. For the majority of the specimens, the core joint cracking started for 1.0% drift and the concrete spalling started for drift levels between 2.0% and 2.5%. Bar buckling was only observed in the inferior column of specimen IPD. The maximum strength was achieved for drift levels between 1.5% and 2.0%. The ultimate force for specimens with plain bars was achieved for a drift ranging from 3.1% to 3.2%, except for the specimen with slab.

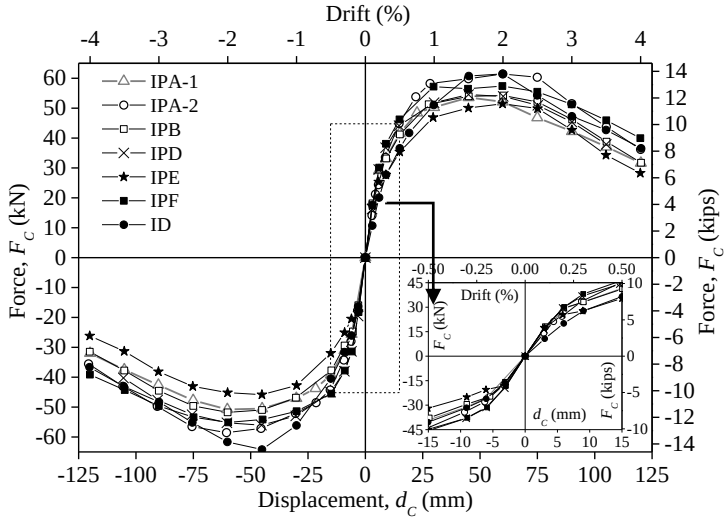

Figure 4.4 – Experimental force-drift envelopes. (Note: 1mm = 0.0394in)

Table 4.2 – Force and drift for the maximum strength and ultimate points.

Specimen	$F_{c,max}$ kN (kip)	$Drift_{Fc,max}$ %	$F_{c,ult}$ kN (kip)	$Drift_{Fc,ult}$ %
IPA-1	53.6 (12.0)	2.0	42.8 (6.9)	3.2
IPA-2	61.4 (13.8)	2.0	49.1 (11.0)	3.2
IPB	54.2 (12.2)	2.0	43.4 (9.7)	3.2
IPD	54.6 (12.3)	1.5	43.6 (9.8)	3.1
IPE	51.4 (11.6)	2.0	41.1 (9.2)	3.1
IPF	57.4 (12.9)	2.0	45.9 (10.3)	3.5
ID	61.5 (13.8)	1.5	49.2 (11.1)	2.8

No significant differences were observed in the strength degradation between the specimens. For all specimens the strength degradation can be defined as constant up to 1.5% drift between the first and the second cycles (8.0% less), and between the first and the third cycle (10.8% less). For drift demands larger than 2.0% the strength degradation can also be defined as constant being 11.5% less between the first and second cycles and 16.8% between the first and third cycles. The maximum flexural capacity of the beams (was achieved around 90% of the total capacity) and columns (was achieved around 80% of the total capacity) was not achieved in the tests, hence the strength of the specimens was controlled by the strength of the core joint. The pinching effect is similar in all specimens as shown in Figure 4.3 and relates to the shear damage inside the joint once the pinching effect starts with the onset of shear cracks in the joint.

4.4.2 Dissipated energy evolution

The hysteretic dissipated energy evolutions, calculated as the area under the experimental lateral force-displacement diagrams, are shown in Figure 4.5. The ultimate point was achieved in all specimens for drift demands up to 3.5%. Foreseen comparing the energy dissipation for all specimens tested, this comparison was made up to 3.5% drift demand, considering the same loading history. Thus, at the end of the third cycle of 3.5% drift demand imposed, all specimens dissipated more energy than the reference specimen, namely: specimen ID dissipated +7%, specimen IPB +8%, specimen IPD +15%, specimen IPE +2%, specimen IPF +7% and specimen IPA-2 +20%.

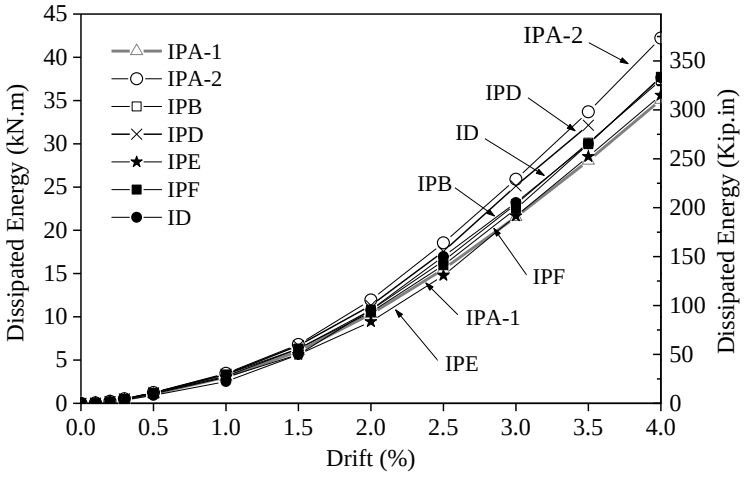

Figure 4.5 – Evolutions of the hysteretic dissipated energy.

Better bond conditions for specimen ID with deformed reinforcing bars lead to larger energy dissipation (more 7%) than the reference specimen (IPA-1) at 3.5% drift demand. The difference observed in this testing campaign in terms of dissipated energy between the specimen with plain and deformed reinforcing bars was inferior than the obtained in other previous works available in the literature (namely: [14]). Specimen with lapping bars only in the superior column (IPB) and specimen with slab (IPF) dissipated similar energy amounts. The lapping in the column for specimen IPB induced larger energy dissipation than the observed in the reference specimen, which is in accordance with the experimental observations for columns tested with and without lapping [30]. Also, the specimen with lapping in beams and superior column (IPD) dissipated 15% more energy than the reference specimen, which emphasise the increase of the energy dissipation when exists lapping of longitudinal reinforcing bars. Specimen IPE, with bent-up bars in the beams, and the reference specimen dissipated similar amount of energy. Specimen IPA-2, with larger concrete strength, dissipated 20% more energy than the similar reference specimen.

The energy dissipated by the joint, beams and columns were also calculated separately. The results evidence the contribution to the total dissipated energy of each element (joint, beams and columns) for each drift demand level.

The energy dissipation in the joint was computed as the area under the lateral shear force versus joint distortion diagrams. The horizontal shear force in the joint (V_{jh}) is calculated by Equation (4.1) according to Hakuto et al. [31], where M_{b1} and M_{b2} are the beam moments at the face of the joint core, j_{d1} and j_{d2} are the lever arms between the tensile forces and the centroids of the compressive forces at the right and left hand sides of the joint respectively (in this study the average values of j_{d1} and j_{d2} are $0.95 \cdot d$, where d is the effective depth), and V'_c is the shear force in the base of the superior column. The joint distortion displacement was calculated according to the methodology presented in [32], i.e. adopting the deformations measured by the potentiometers placed diagonally on the joint core.

$$V_{jh} = \frac{M_{b1}}{j_{d1}} + \frac{M_{b2}}{j_{d2}} - V'_c \tag{4.1}$$

The dissipated energy at the beams and columns was computed integrating along the elements length the moment-curvature experimental results. The dissipated energy at the

beams and columns was computed assuming a linear distribution of curvatures from the elements' extremity to the interface between slice 1 and slice 2 (see Figure 4.2d) and assuming a constant distribution of curvatures in slice 1.

The sum of the dissipated energy of the joint, beams and columns for each drift demand was calculated and compared with the corresponding total energy dissipation obtained from the integration of the lateral force versus drift diagram (Figure 4.5). For drift demands ranging from 0.2% to 4%, the sum of the dissipated energy calculated independently in the components (beams, columns and joint) represents in average 95% of the total dissipated energy (coefficient of variance equals to 6%). Therefore, it is concluded that the methodology adopted to compute the dissipated energy of the components allow to estimate with good accuracy the fraction of dissipated energy per component.

The evolutions of the dissipated energy contribution of the joint, beams and columns to the total dissipated energy for drift demands larger than 0.2% are represented in Figure 4.6. Despite that the total energy dissipation evolutions, as showed in Figure 4.5, are similar in the majority of the specimens, the evolutions of the energy dissipation at each component are quite different between specimens, as shown in Figure 4.6.

For drift demands lower than 0.3%, the beams dissipated more energy than the other components, ranging from 47% (IPF) to 80% (IPB), except for specimen IPD where the columns dissipated 59% of the energy dissipated. Up to the cycle corresponding to 4% drift demands, the joint specimens dissipated more energy than the other elements, ranging from 61% (IPE) to 75% (IPB), except for specimen IPD where the columns dissipated 79%.

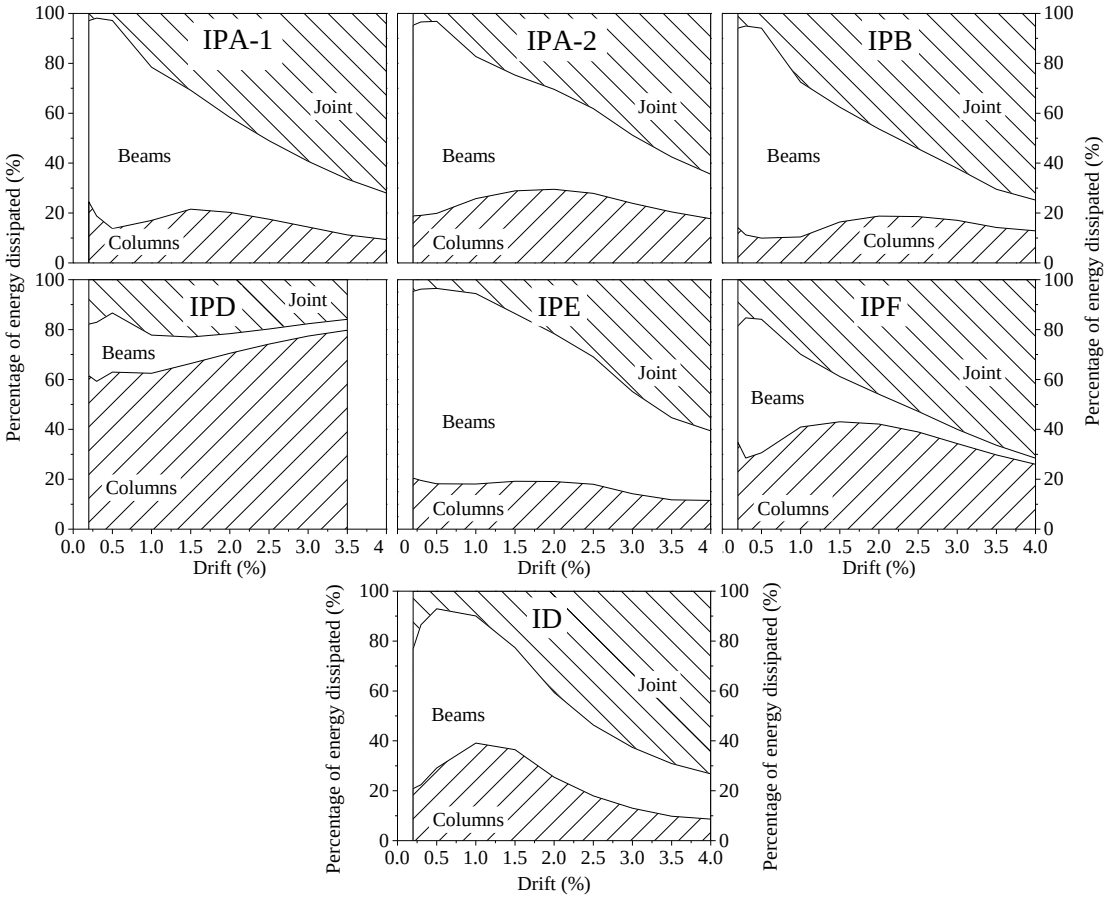

Figure 4.6 – Contribution to the total dissipated energy of different components: joint, beams and columns.

The dissipated energy by the components in specimens IPA-1 and IPB was similar. Therefore, lapping of the longitudinal bars in the superior column did not affected the dissipated energy by the elements. For specimen IPA-2 the dissipated energy of the columns was approximately 50% larger than in the reference specimen.

For the specimen with reinforcement lapping in beams and columns (IPD), the dissipated energy by the columns was significantly larger than for the reference specimen. The lapping of the reinforcing bars in the beam which duplicated the reinforcement amount in the joint increased, and thus the joint shear capacity, apart from the increasing of the flexural capacity of the beams close to the joint. Therefore, the damages mostly occurred in the columns.

For specimen with bent-up bars in the beam (IPE), the dissipated energy by the beams was almost twice than for the reference specimen at 4.0% drift demand, due to the

lower amount of reinforcement in the beams inferior face of specimen IPE, increasing the damages in the beams.

In the specimen with the slab (IPF), the dissipated energy by the columns was almost twice for all drift demands than the reference specimen. As a consequence, the dissipated energy of the beams of specimen IPF was much lower than the observed in the reference specimen. However, the dissipated energy of the joint was similar in both specimens.

For the specimen with deformed bars (ID), the relative contribution of the dissipated energy by the columns achieved its maximum at 1.0% drift, while for the specimen with plain reinforcing bars the maximum value is achieved for drift demands larger than 1.5%. For drift demands superior to 0.5%, the energy dissipated by the joint in specimen ID was similar to the obtained for the reference specimen.

4.4.3 Displacement ductility and equivalent damping

The displacement ductility-equivalent damping relationship are useful information for numerical macro-elements that represent the global behaviour of structural elements such as columns, beam-column joints and beams. In this work, for each specimen tested, the equivalent damping was computed as a function of the displacement ductility (μ_{Δ}) according to Equation (4.2), presented in Varum [6], where $A_{half\text{-}loop}$ is the area within "half" force-displacement cycle and F_{max} and D_{max} are the maximum force and maximum displacement achieved in the respective half cycle. The displacement ductility is defined as the ratio between the maximum imposed displacement in each cycle and the yield displacement (Δ_y).

$$\xi_{eq} = \frac{1}{\pi} \cdot \frac{A_{half-loop}}{F_{\max} \cdot D_{\max}} \tag{4.2}$$

The yield displacement was calculated according to Annex B.3 of EC8-1 [33], being assumed an elastic-perfectly plastic force-displacement relationship. The elastic-perfectly plastic relationship was fitted to the force-displacement envelope of the experimental results up to the ultimate point and taking into account the following requirements: i) the area under and above the experimental envelope curve must be equal; and ii) the area under (or above) the envelope curve is the minimum. Table 4.3 indicates the yield force

($F_{c,y}$), the drift at yield ($Drift_y$) and the displacement ductility at the ultimate point ($\mu_{\Delta,ult}$), for the fitted bi-linear curves.

Table 4.3 – Yield force, yield drift, displacement ductility at ultimate point and equivalent damping.

Specimen	$F_{c,y}$ kN (kip)	$Drift_y$ %	$\mu_{\Delta,ult}$	$\xi_{eq,ult}$ %
IPA-1	48.7 (10.9)	0.52	5.58	9.21
IPA-2	56.0 (12.5)	0.54	5.92	9.32
IPB	49.5 (11.1)	0.50	6.40	9.54
IPD	52.4 (11.8)	0.52	5.96	9.66
IPE	44.8 (10.0)	0.51	6.07	10.18
IPF	53.3 (12.0)	0.50	7.00	8.63
ID	56.6 (12.7)	0.67	4.33	8.69

Marked differences were observed in terms of displacement ductility at the ultimate point, ranging from 4.33 for specimen ID to 7.00 for specimen IPF (see Table 4.3). Specimen ID, with deformed reinforcing bars, has the largest drift yield, and consequently the lower displacement ductility at ultimate point.

Figure 4.7 shows the equivalent damping obtained from the experimental results, as function of the displacement ductility (μ_Δ) and the corresponding best-fit curves defined according to the general expression proposed by Priestley [34] (see Table 4.4). For each specimen studied, the equivalent damping obtained from the best-fit damping curve corresponding to the ultimate point ($\xi_{eq,ult}$) is presented in Table 4.3.

Generically, the fitted equivalent damping-displacement ductility relationships obtained are very similar, except for specimens IPF and ID. Specimen with deformed bars (ID) had an initial damping of ~5% (lower than in specimen IPA-1), and the damping increase with the displacement ductility is more pronounced when compared with other specimens. This result is in agreement with the conclusions obtained in other study [14] carried out on RC beam-column joints built with plain reinforcing bars. However, from tests carried out on columns [30] was observed, for displacement ductility $\mu_\Delta \geq 1.0$, larger equivalent damping (+49% at ultimate point) on the specimen with deformed reinforcing bars than for a similar specimen built with plain bars. This difference can be explained by the noticeable influence of the core joint in the global response of the beam-column joints, as discussed in the following sections. Furthermore, the equivalent damping-displacement ductility relationship is much influenced by the yielding displacement that depends on the approach followed in its calculation [7].

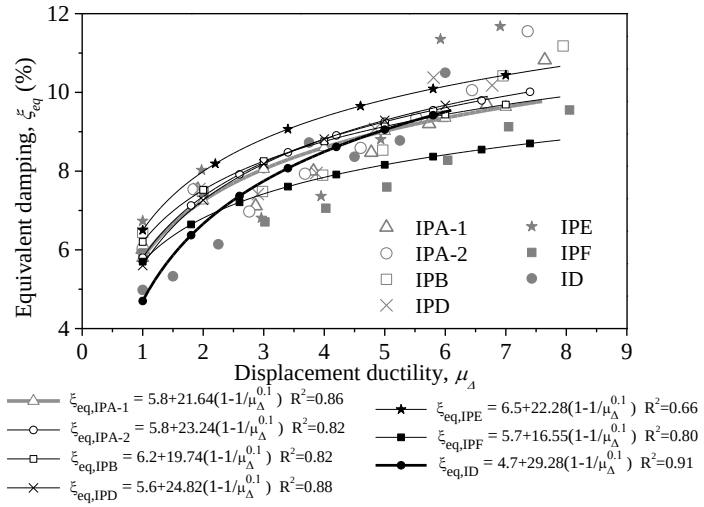

Figure 4.7 – Equivalent damping-displacement ductility diagrams.

Table 4.4 presents the general equivalent damping-displacement ductility Equation proposed by Priestley [34] (Equation 4.3), the expression proposed by Melo et al. [30] (Equation 4.4) based on the experimental results of columns built with plain reinforcing bars, and other three curves (Equations 4.5 to 4.7) that were fitted to the experimental results (of other authors and the ones presented in this work) of elements with plain reinforcing bars [14,6].

Table 4.4 – Equivalent damping-displacement ductility relationships.

Experimental data source	Elements type	Equation		Equation proposed in the literature
	Generic	$\xi_{eq} = \xi_0 + a \cdot \left(1 - \frac{1}{\mu^{\beta}}\right)$	(4.3)	Priestley [34]
	Columns	$\xi_{eq} = 3.8 + \frac{146}{\pi}\left(1 - \frac{1}{\mu^{0.1}}\right)$	(4.4)	Melo et al. [30]
Varum [6]	Structural response governed by column mechanisms	$\xi_{eq} = 3.5 + \frac{173}{\pi}\left(1 - \frac{1}{\mu^{0.1}}\right)$	(4.5)	
Fernandes et al. [14]	Beam-column joints	$\xi_{eq} = 4.8 + \frac{67}{\pi}\left(1 - \frac{1}{\mu^{0.1}}\right)$	(4.6)	
present experimental data	Beam-column joints	$\xi_{eq} = 5.9 + \frac{68}{\pi}\left(1 - \frac{1}{\mu^{0.1}}\right)$	(4.7)	

Equations (4.4) to (4.7) follow the generic form of Equation (4.3), considering β=0.1 and adopting for the parameter a and for the initial damping (ξ_0) the values resulting from the best-fit to the respective experimental results. Equation (4.4), proposed in Melo et al. [30], was derived based on experimental results of RC columns built with plain reinforcing bars. Equation (4.5) was obtained based on experimental results of pseudo-dynamic tests performed on a full-scale RC frame structure built with plain bars, reported in Varum [6]. Although Equation (4.5) was calibrated based on the response of the frame at the storey level (storey shear versus inter-storey drift), and since the response of that frame was mainly governed by the deformation of the columns, it is considered that Equation (4.5) better represents the equivalent damping-displacement ductility for columns.

Equation (4.6) was fitted to the experimental results obtained in the tests performed by Fernandes et al. [14] on beam-column joints built with plain reinforcing bars.

Figure 4.8 compares the experimental results reported in this work with and the curves given by Equations (4.4) to (4.6), all fitted to experimental results of elements built with plain reinforcing bars. In the same figure is represented the curve fitted to the experimental results reported in this work (Equation 4.7).

From the analysis of the plots presented in Figure 4.8, it is noticeable the difference between the curves given by Equations (4.4) and (4.5) obtained from experimental results of structures governed by column mechanisms or columns, and the curves given by Equations (4.6) and (4.7) obtained from experimental results of beam-column joints.

The two curves fitted to beam-column joints' experimental results present a difference of 1.1% in terms of initial damping (ξ_0), but parameters a and β are almost the same in both cases (see Equations 4.6 and 4.7).

For displacement ductility $\mu_\Delta \geq 2.0$, columns (Equations 4.4 and 4.5) showed larger equivalent damping than beam-column joints. For columns the parameter a is almost twice that what was obtained for the beam-column joints. Equations (4.4) to (4.7) are dependent of the definition of the yielding point for columns and beam-column joints and because of that the same method should be followed in the determination of the yielding point in both cases.

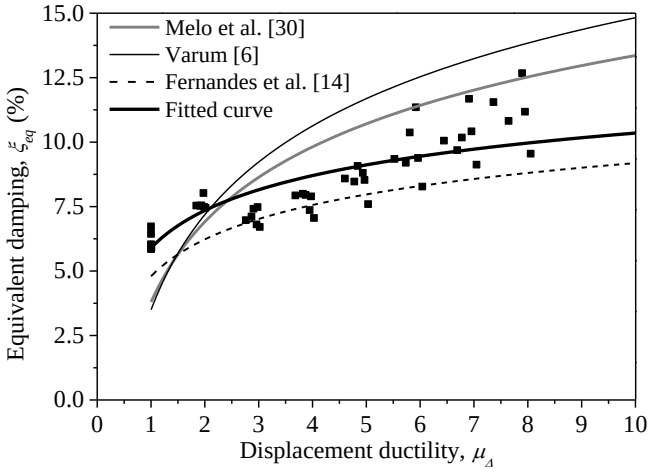

Figure 4.8 – Equivalent damping-displacement ductility diagrams: comparison between all experimental results and curves fitted to experimental results of other authors for elements with plain reinforcing bars [6,14,30].

4.4.4 Final damage pattern

The crack pattern observed at the end of the experimental tests is illustrated in Figure 4.9. The majority of the cracks are located in the stirrups vicinity due to the concrete discontinuity caused by the stirrups. Shear cracks followed by concrete spalling occurred in all specimens at the core joint, except in specimen IPD where only shear cracks were observed. In specimens IPA-1 and IPA-2 were observed similar crack patterns and the concrete spalling occurred in the same location for both specimens. Therefore, the concrete strength did not affect the type of damage. Specimen IPB showed more cracks at the base of the superior column than observed in the reference specimen due to the lapping of the longitudinal reinforcing bars in that region. The lapping of the longitudinal plain bars increased the damage in the concrete surrounding the bars' hooks due to the concentrated forces transferred to the concrete. Specimen IPD presented larger damage level than for the others specimens at the inferior column-joint interface and buckling of the bars was observed there. In fact, the bars' buckling was only observed for this specimen since the lapping of the longitudinal beams' reinforcement in specimen IPD increased the shear capacity of the joint and the flexural capacity of the beams close to the joint, therefore reduced the concrete damage in the joint and beams. As in specimen IPB, specimen IPD also showed more cracks at the base of the superior column than the observed in the reference specimen. In specimen IPE the concrete damage was more concentrated at the joint and beam-joint interface regions and only few cracks were observed in the columns,

due to the lower amount of longitudinal reinforcement in bottom face of the beams. For the specimen with slab (IPF), it was observed higher number of cracks with lower thickness at the superior face of the beam (beam face with slab) than in the opposite side. In fact, the presence of the slab induced a remarkable difference in terms of stiffness and steel amount of the beams when loaded for each bending direction. The concrete damage in specimen ID was more distributed along the elements' span than in all other specimens built with plain bars, which is in accordance with observations made by others authors [14,30]. Two failure modes were observed in the tests, namely concrete cover spalling followed by bar buckling in the column-joint interface for specimen IPD, and shear cracks followed by concrete spalling in the core joint for the other specimens.

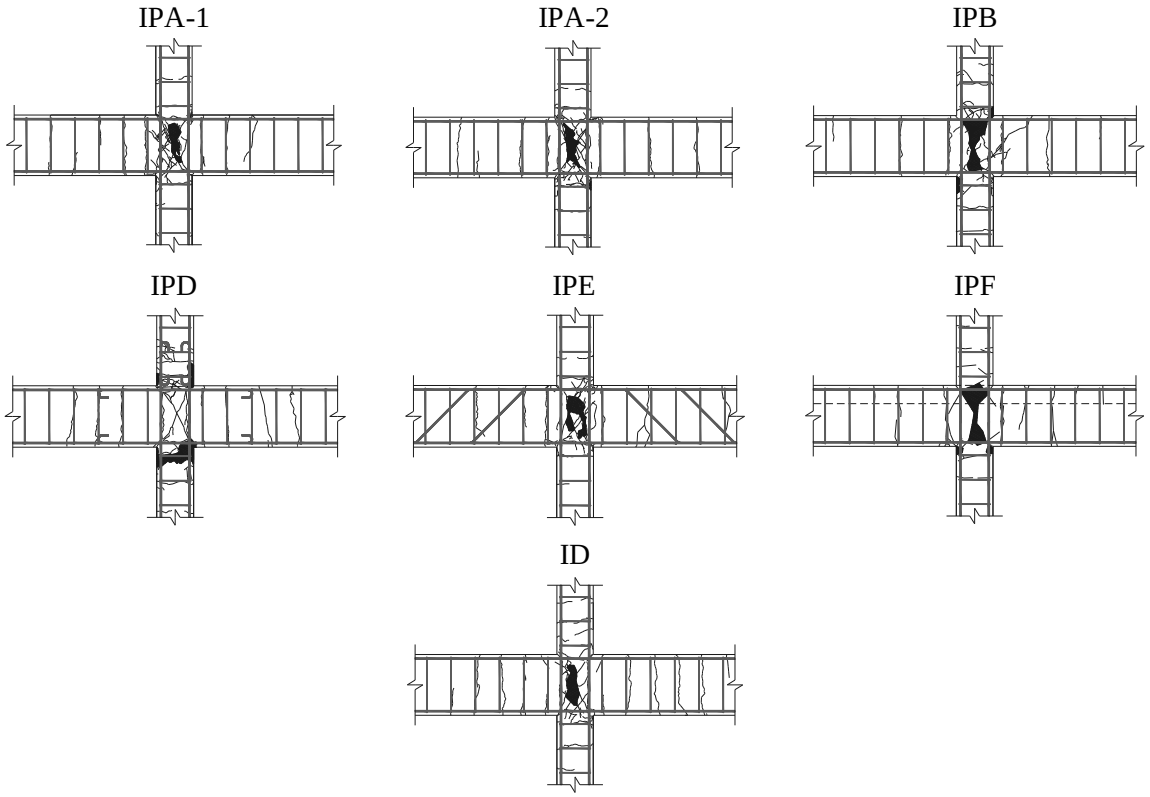

Figure 4.9 – Final damage state for the top face of the specimens.

4.4.5 HRC damage index

The homogenised reinforced concrete damage scale (HRC-scale) is a damage index developed by Rossetto and Elnashai [35] and it is used to generate vulnerability curves. The HRC-scale was calibrated to a large scale experimental data [36] and was subdivided into seven damage states. It was defined according to the typical structural and non-structural damages expected in ductile, non-ductile and infilled RC moment resisting frame

structures (MRF) and in RC shear-wall structures. The limit states are defined in terms of a damage index, identified as HRC-damage index (DIHRC). This damage index provide a numerical reference scale (calibrated with experimental results) based on the maximum inter-storey drift ratio (expressed in percentage), called ISDmax%. Rossetto and Elnashai [35] proposed Equation (4.8) to calculate the HRC damage scale for non-ductile MRF.

$$DI_{HRC} = 34.89 Ln(ISD_{max\%}) + 39.39 \quad (4.8)$$

The experimental observations and the HRC-damage index curve for bare non-ductile MRF, given by Equation (4.8), are presented in Figure 4.10. The limits of the seven damage states, namely: none; slight; light; moderate; extensive; partial collapse; and collapse, are also shown in Figure 4.11. According to Rossetto and Elnashai [35], the damages observed in the tests, namely beams or columns cracking, joint cracking, concrete cover spalling, buckling of the bars and ultimate points correspond to the HRC-damage index values of 20, 40, 60, 80 and 90, respectively. Based on the HRC-scale for bare non-ductile MRF, in the present experimental testing campaign was observed that: beams or columns cracking corresponds to the light damage state; joint cracking and cover spalling correspond to the moderate damage state; buckling to the extensive damage state; and, the ultimate point corresponds to structural partial collapse (corresponding to the collapse of the beam-column joints).

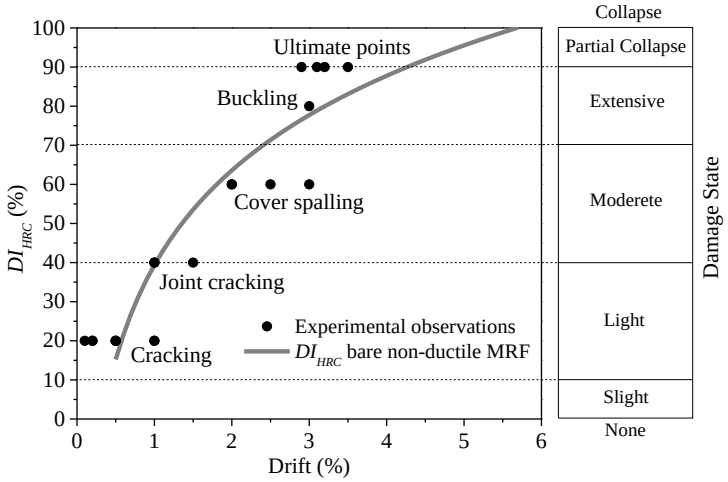

Figure 4.10 – HRC-damage index curve for bare non-ductile MRF and experimental observations.

Comparing the average of the experimental drift values for each type of damage with the corresponding predicted DIHRC values with Equation (4.8), the differences found are:

-34% for beams or columns cracking, +11% for joint cracking, +25% for concrete cover spalling, -7% for bars' buckling and -37% for the ultimate points. Therefore, the small differences between the empirically predicted and the experimental values, allows concluding that the DIHRC curve represents with good agreement the experimental observations for the beam-column joints built with plain bars.

4.4.6 Displacement components

Different deformation mechanisms contribute to the lateral displacement (d_c) when a specific lateral demand is imposed at the top of the superior column, such as: i) shear in columns; ii) bending in beams and columns; iii) joint relative rotation; and iv) joint shear distortion. In this section the lateral displacement at the top of the specimen are calculated analytically as the sum of the different deformation mechanisms presented before. Results obtained are compared with the corresponding experimental values.

The lateral displacement due to shear was calculated considering an elastic shear modulus (G) of 7.25GPa (1052ksi) and a constant distribution along the beams and columns length. The elastic shear modulus was computed considering the Young's modulus of the concrete (estimated from the average concrete strength) and considering a Poisson's ratio equal to 0.2.

In this study, the lateral displacement due to bending in beams and columns was assumed as a sum of two components: a) linear elastic; and b) non-linear bending. The elastic bending component was computed with the direct integration method, assuming a linear distribution of curvatures from the elements' extremity to the beam/column-joint interface [14,15]. The linear curvature distribution in each element (beam or column) was obtained fitting a straight linear function to the curvatures obtained experimentally in the non-damaged element zones (corresponding to slices 2, 3 and 4 according to Figure 4.2d) and assuming zero curvature at the element extremity (end of slice 4). The non-linear bending was calculated by the direct integration method, considering a parabolic variation between the interface of slices 1 and 2 and the element-joint interface (end of slice 1), where occurs the maximum curvature. Therefore, it was assumed that the non-linear bending occurs only in slice 1. The non-linear curvature component in slice 1 was obtained subtracting the elastic curvature to the mean curvature measured in the experimental tests. Then, the non-linear curvature was used to compute the non-linear bending lateral

displacement component [14,15]. This non-linear bending lateral displacement of the specimen intends to represent the damage mechanisms in beams and columns associated to flexure deformation, as concrete flexural cracks, concrete spalling, bars yield and buckling and bar slippage.

The lateral displacement component called "joint relative rotation" represents the displacement due to the deformations in the joint apart from the joint shear distortion, i.e. the contribution of the joint expansion and the relative rotation between the top and bottom joint sections. The joint relative rotation was calculated using the relative displacements measured by both diagonal potentiometers in the core joint. The lateral displacement was obtained multiplying the joint relative rotation by the length of the column.

The displacement component due to joint shear distortion was calculated according to the methodology presented in [32], i.e. adopting the deformations measured by the potentiometers placed diagonally on the joint core.

Using the methodology and assumptions exposed before, in generic terms, a good agreement was found between the experimental and the analytical results, which allows to conclude that the deformation mechanism are well identified and their influence in the response of the joint specimen are well quantified. For drift values ranging from 0.3% to 3.5% the average differences observed between the analytical and the experimental results: IPA-1 8% (CoV=0.06); IPA-2 1% (CoV=0.03); IPB 7% (CoV=0.03); IPD 2% (CoV=0.05); IPE 9% (CoV=0.04); IPF 7% (CoV=0.06); and ID 2% (CoV=0.07). Even being small the differences (less than 9%), for all cases the total analytical lateral displacement underestimated the corresponding experimental result.

Figure 4.11 shows the contribution for the lateral displacement of the different deformation mechanisms: columns shear, linear elastic bending in beams and columns, non-linear bending in beams and columns, joint relative rotation and joint shear distortion, for drift demands between 0.1% and 3.5%. For lower drift demand values (up to 0.2%), the relative displacements measured in certain potentiometer locations are close to their sensibility and, therefore, these results were excluded in this analysis. The comparisons done in this section are developed up to the ultimate point, which for all specimens is reached for a drift demand inferior to 3.5%.

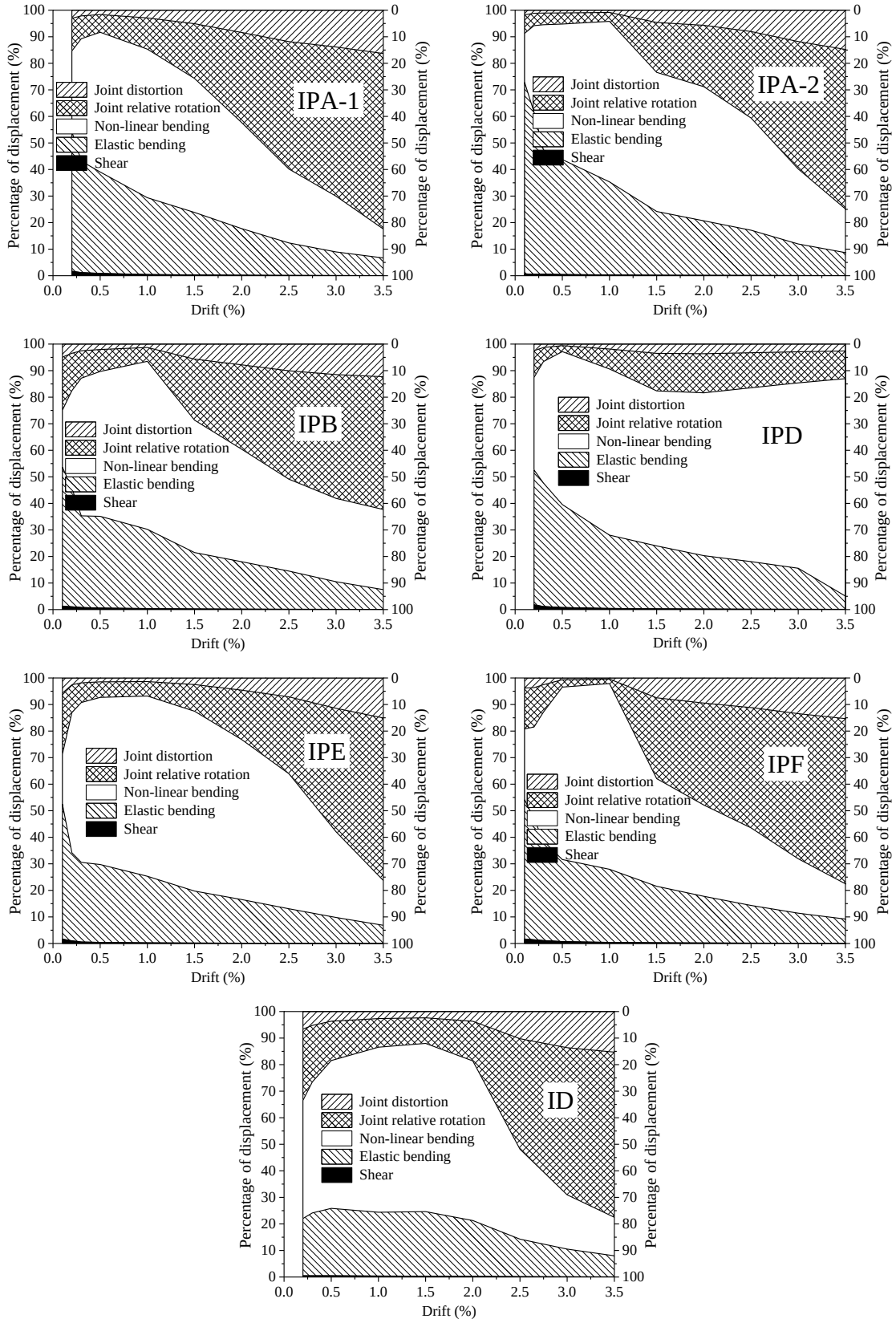

Figure 4.11 – Contribution to the total lateral displacement of the different deformation mechanisms: columns shear, linear elastic bending in beams and columns, non-linear bending in beams and columns, joint relative rotation and joint shear distortion.

The relative contribution of the shear deformation in columns to the lateral displacement of the specimen was small for all specimens, representing around 2.0% of the lateral displacement for 0.2% drift demand and 0.2% for 3.5% drift.

As expected, for all specimens, the relative contribution of the elastic bending in beams and columns to the lateral displacement of the specimens always decreases with the increase of the drift demands. For specimens with plain bars, an approximately linear variation was observed, ranging from 30-43% (for drift of 0.5%) to 5-9% (for drift of 3.5%). Between 0.1% and 0.5% drift demands, the relative contribution had a pointed drop due to the onset of flexural cracks. For the specimen with deformed bars (ID), the elastic bending component was almost constant (~25%) up to 1.5% drift and then decrease linearly to 8% at 3.5% drift.

The evolution of the relative contribution of the non-linear bending in beams and columns in function of the drift demand varies significantly between the specimens studied. In fact, this deformation mechanism is strongly related to the curvatures distribution along the elements. Different levels of damage and corresponding curvature demand was observed at slice 1 for the different specimens. This aspect will be further discussed in the next section.

The contribution of the joint relative rotation to the total lateral displacement increases with the damages in the joint core for drift demands larger than 0.5% and represented up to 66% of the total displacement for 3.5% drift. For drift demands between 0.1% and 0.5%, the joint relative rotation contribution decrease, since it corresponds to an elastic deformation (was not observed damage in the concrete of the joint core).

The contribution of the joint shear distortion to the lateral displacement increases approximately linearly with the drift demands, varying from 1.5-5.0% to 3.0-16.0%, for 0.3% and 3.5% drift, respectively.

4.4.7 Joint shear capacity

Some authors [37,38,39] state that the maximum strength of the specimens is controlled by the failure mechanism of the joints, where shear strength of the joint is one of the possible failure mechanism. In the literature, the shear stress in the core beam-column joint is

normally expressed in terms of nominal shear stress, or in terms of principal compression/tensile stresses.

The nominal horizontal shear stress (v_{jh}) in the core joint can be computed by Equation (4.9), where: V_{jh} is the horizontal shear force in the joint, calculated by Equation (4.1); b_j is the effective width of the core joint, which for all the columns and beams in the specimens here studied is equal to 0.30m (11.8in); h_c is the depth of the columns, i.e. 0.30m (11.8in).

$$\nu_{jh} = \frac{V_{jh}}{b_j \cdot h_c} \tag{4.9}$$

Based on the Mohr's circle, the principal stresses (p_t) at the mid-depth of the core joint is given by Equation (4.10), where f_a is the nominal axial compressive stress on the column calculated by Equation (4.11), and compressive stresses are taken as negative.

$$p_t = \frac{-f_a}{2} \pm \sqrt{\left(\frac{f_a}{2}\right)^2 + \nu_{jh}^2} \tag{4.10}$$

$$f_a = \frac{N}{b_j \cdot h_c} \tag{4.11}$$

According to Hakuto et al. [31], the prediction of the principal compression stresses by Equation (4.10) are acceptable up to the diagonal tension cracks occur. Hakuto et al. [31] also state that one approach for the assessment of the shear strength of interior beam-column joints without shear reinforcement is to assume that the shear strength is reached at the point of initial diagonal tension cracking of the joint core. However, this criterion for joint core failure may be too conservative since the joint core may be capable of transferring significantly higher shear after diagonal tension cracking by means of the diagonal compression strut mechanism. In that case, the joint failure occurs as a consequence of the diagonal compression failure.

According to Eurocode 8 (EC8-1) [33], the diagonal compression induced in the joint by the diagonal strut mechanism shall not exceed the compressive strength of the concrete (f_c) in the presence of transverse tensile strains. For interior joints, in the absence of a more precise model, the requirement may be satisfied if Equation (4.12) is fulfilled, i.e. if the

horizontal shear force in the joint does not exceed $\overline{V}_{jh}^{EC8}$. In Equation (4.12), v is the normalized axial load in the column above the joint, h_{jc} is the distance between extreme layers of column reinforcement and η is given by Equation (4.13), where f_{ck} is the characteristic compressive concrete strength in MPa.

$$V_{jh} \le \eta \cdot fc \cdot \sqrt{1-\frac{\nu}{\eta}} \cdot b_j \cdot h_{jc} = \overline{V}_{jh}^{EC8} \tag{4.12}$$

$$\eta = 0.6 \cdot \left(1 - f_{ck}/250\right) \tag{4.13}$$

Hwang and Lee [40] propose a model called the softened strut-and-tie model to that is capable of predicting the shear strength of interior beam-column joints for seismic resistance. This model is based on the concept of struts and ties and derived to satisfy equilibrium, compatibility, and the constitutive laws of cracked reinforced concrete.

Table 4.5 presents: i) the maximum horizontal shear force in the joint ($V_{jh,max}$) and the corresponding drift ($\Delta_{Vjh,max}$), ii) the ratio between the maximum experimental horizontal shear force and the EC8-1 [33] limit ($\overline{V}_{jh}^{EC8}$), iii) the ratio between the maximum experimental horizontal shear force and the predicted strength according to Hwang and Lee [40] model ($\overline{V}_{jh}^{Hwang\&Lee}$), iv) the maximum principal tensile stress in the joint ($p_{t,max}$), and v) the ratio between the maximum principal tensile stress in the joint and the average concrete tensile strength (f_{ctm}).

Table 4.5 – Maximum shear forces and maximum principal tensile stress in the joint.

Specimen	**Horizontal shear force**				**Principal tensile stress**	
	$\Delta_{Vjh,max}$ **%**	$V_{jh,max}$ **kN (kip)**	$V_{jh,max}/\overline{V}_{jh}^{EC8}$	$V_{jh,max}/\overline{V}_{jh}^{Hwang\&Lee}$	$p_{t,max}$ **MPa (ksi)**	$p_{t,max}/f_{ctm}$
IPA-1	1.5	370.4 (83.3)	1.17	1.24	2.2 (0.32)	0.87
IPA-2	2.0	399.4 (89.8)	0.60	1.09	2.4 (0.35)	0.76
IPB	2.0	401.2 (90.2)	0.97	1.25	2.4 (0.35)	0.70
IPD	1.5	415.5 (93.4)	1.55	1.49	2.4 (0.35)	1.04
IPE	2.0	334.4 (75.2)	1.12	1.13	2.0 (0.29)	0.85
IPF	2.0	401.9 (90.4)	1.13	1.31	2.4 (0.35)	1.05
ID	2.0	468.2 (105.3)	1.67	1.59	2.9 (0.42)	1.20

The joints failure in shear mainly due to the horizontal shear forces which exceed the EC8-1 limit $\overline{V}_{jh}^{EC8}$, except for specimen IPA-2. The experimental horizontal shear forces also exceed the Hwang and Lee [40] prediction for all specimens. In specimens IPD, IPF

and ID the principal tensile stresses observed also exceed the concrete tensile strength. For specimen IPA-2 the EC8-1 formulation overestimated the shear capacity once that shear cracks were observed in the joint. On the other hand, the specimen with lapping of the reinforcement in the beams and superior column (IPD), presented the largest $V_{jh,max}/\overline{V}_{jh}^{EC8}$ and $V_{jh,max}/\overline{V}_{jh}^{Hwang\&Lee}$ ratios among the specimens with plain reinforcing bars, but for this specimen the shear cracks were less expressive than for the other specimens. This occurrence was related with the double amount of longitudinal reinforcement in the beam at the joint region, which increased the joint capacity. Therefore, the influence of the longitudinal steel amount should be considered in Equation (4.12). For specimen ID was obtained the largest $V_{jh,max}/\overline{V}_{jh}^{EC8}$ and $V_{jh,max}/\overline{V}_{jh}^{Hwang\&Lee}$ ratios. The principal tensile stress reach the tensile concrete strength for specimens IPD, IPF and ID. The observed maximum principal tensile stress are around 50% lower than the ones present in Chalioris et al. 2008 [41] for exterior beam-column joints.

4.5 CONCLUSIONS

The experimental campaign described in this study was carried out for assessing the cyclic behaviour of full-scale RC interior beam-column joints built with plain reinforcing bars and without seismic reinforcement detailing. Six specimens with plain reinforcing bars and one with deformed reinforcing were designed according to old Portuguese RC code specifications, which represent the typical elements detailing in existing buildings in European Mediterranean countries until the 1970s. The influence of reinforcing steel surface, lapping of the longitudinal reinforcing steel bars, bent-up bars in the beam, slab contribution and concrete strength were investigated.

The differences between the specimens (surface and detailing of the reinforcement, slab or concrete compressive strength) did not affected largely their global response. However, considerable differences were found regarding the local behaviour, i.e. section curvatures; component dissipated energy and damage at the plastic hinges.

The methodology adopted to compute the energy dissipated by the components (joint, beams and columns) represents on average 95% of the total hysteretic energy obtained experimentally. Therefore, the methodology adopted allows obtain the evolution of the dissipated energy by each component with accuracy. Generically, the results have

shown that the dissipated energy of the joints increased and of the beams dropped when the drift demands increase.

Shear joint failure was observed for all specimens, except for specimen IPD where flexural failure in the inferior column occurred. The shear joints failure occurred because there were no stirrups in the joint and as a consequence the concrete confinement was poor. The shear failure is also intensified by the reinforcing slippage that occurred inside the joint.

The DIHRC curve developed by Rossetto and Elnashai [33] for non-ductile moment resisting frame represented with good agreement the experimental observations for the beam-column joints studied.

The contributions to the total lateral displacement due to the shear in columns, elastic bending, non-linear bending, joint relative rotation and joint distortion were calculated for all specimens. The maximum difference found between the imposed displacement and the sum of all contributions computed was 9% with a coefficient of variance equals to 4%. Therefore, the methodology and assumptions considered to calculate the contribution of each deformation mechanism give a good approach to the imposed lateral displacements. The displacement due to the columns shear represented in maximum 2.0% of the total displacement. The relative percentage of the elastic bending decrease almost linearly when the displacements demands increase. The relative percentage of the total displacement due to the non-linear bending and joint relative rotation represent the largest relative percentages and play between one each other, i.e. if one increase the other decrease. The joint distortion can represent up to 16% of the total displacement.

For large concrete compressive strength, the EC8-1 [31] formulation overestimated the horizontal shear capacity of the joint. However, for specimens with larger longitudinal reinforcement on the beams in the joint region, the EC8-1 formulation may underestimate the horizontal shear capacity of the joint. Therefore, the reinforcement ratio should be considered in the EC8-1 formulation to compute the horizontal shear capacity. The model proposed by Hwang and Lee [40] underestimated (less 25%) the shear strength.

4.6 REFERENCES

[1] Ioannou I, Borg R, Novelli V, Melo J, Alexander D, Kongar I, Verrucci E, Cachill B, Rossetto T. The 29th May 2012 Emilia Romagna Earthquake – EPICentre Field Observation Report. No. EPI-FO-290512 2012. University College London, Depart. of Civil, Environmental and Geom. Eng., 2012.

[2] Rosseto T, Peiris N, Alarcon J, So E, Sargeant S, Sword-Daniels V, Libberton C, Verrucci E, Re D, Free M. The L'Aquila, Italy Earthquake of 6 April 2009 – A Preliminary Field Report by EEFIT. *The Earthquake Engineering Field Investigation Team*, University College London, 2009.

[3] Melo J, Fernandes C, Varum H, Rodrigues H, Costa A, Arêde A. Numerical modelling of the cyclic behaviour of RC elements built with plain reinforcing bars. *Engineering Structures* 2011:33(2):273-286. doi: 10.1016/j.engstruct.2010.11.005.

[4] Verderame GM, Fabbrocino G, Manfredi G. Seismic response of RC columns with smooth reinforcement. Part I: monotonic tests. *Engineering Structures* 2008:30(9):2277-2288. doi: 10.1016/j.engstruct.2008.01.025.

[5] Verderame GM, Fabbrocino G, Manfredi G. Seismic response of RC columns with smooth reinforcement. Part II: cyclic tests. *Engineering Structures* 2008:30(9):2289–2300. doi: 10.1016/j.engstruct.2008.01.024

[6] Varum H. Seismic assessment, strengthening and repair of existing buildings. PhD Thesis, University of Aveiro, Portugal, 2003.

[7] Rodrigues H, Arêde A, Varum H, Costa AG. Experimental evaluation of rectangular reinforced concrete column behaviour under biaxial cyclic loading. *Earthquake Engineering & Structural Dynamics* 2013:42(2)239-259. DOI: 10.1002/eqe.2205.

[8] Rodrigues H, Varum H, Arêde A, Costa AG. A comparative analysis of energy dissipation and equivalent viscous damping of RC columns subjected to uniaxial and biaxial loading. *Engineering Structures* 2012:35,149-164. doi: 10.1016/j.engstruct.2011.11.014.

[9] Fardis M. Seismic Design, Assessment and Retrofitting of Concrete Buildings, based on EN-Eurocode 8. *Geotechnical, Geological, and Earthquake Engineering, Springer* 2009:8:744 pages.

[10] IUSS Press. Guidelines for Displacement-based Design of Buildings and Bridges. Risk Mitigation for Earthquakes and Landslides. LESSLOSS Report No. 2007/05, Pavia, Italy, 2007.

[11] Li L, Mander J, Dhakal R. Bidirectional Cyclic Loading Experiment on a 3D Beam-Column Joint Designed for Damage Avoidance. *Journal of Structural Engineering* 2008:134(11)1733-1742. doi: 10.1061/(ASCE)0733-9445(2008)134:11(1733).

[12] Bae S, Bayrak O. Drift Capacity of Reinforced Concrete Columns. *ACI Structural Journal* 2009:106(4)405-415. doi: 10.14359/56606.

[13] Delgado R, Delgado P, Vila Pouca N, Arêde A, Rocha P, Costa A. Shear effects on hollow section piers under seismic action: experimental and numerical analysis. *Bull Earthquake engineering* 2009:7,1733-1742. doi: 10.1007/s10518-008-9098-x.

[14] Fernandes C, Melo J, Varum H, Costa A. Cyclic behaviour of substandard RC beam-column joints with plain bars. *ACI Structural Journal* 2013:110(1)137-148. doi: 10.14359/51684337.

[15] Fernandes, C. Cyclic behaviour of RC elements with plain reinforcing bars. PhD Thesis, University of Aveiro, Portugal, 2012.

[16] Liu A, Park R. Seismic Behaviour and Retrofit of Pre-1970's As-Built Exterior Beam-Column Joints Reinforced by Plain Round Bars. *Bulletin of the New Zealand Society for Earthquake Engineering* 2001:34(1)68-81.

[17] Fernandes C, Melo J, Varum H, Costa AG. Cyclic behavior of a two-span RC beam built with plain reinforcing bars. *Periodica Polytechnica Civil Engineering* 2011:55(1)21-29. doi: 10.3311/pp.ci.2011-1.03.

[18] Bousias S, Spathis AL, Fardis MN. Seismic retrofitting of columns with lap spliced smooth bars through FRP or concrete jackets. *Journal of Earthquake Engineering* 2007:11(5)653-674. doi: 10.1080/13632460601125714.

[19] Di Ludovico M, Verderame G, Prota A, Manfredi G, Cosenza E. Cyclic Behavior of Non-Conforming Full Scale RC Columns. *Journal of Structural Engineering* 2014:140(5). doi: 10.1061/(ASCE)ST.1943-541X.0000891.

[20] Braga F, Gigliotti R, Laterza M. R/C Existing Structures with Smooth Reinforcing Bars: Experimental Behaviour of Beam-Column Joints Subject to Cyclic Lateral Loads. *The Open Construction & Building Technology Journal* 2009:3,52-67. doi: 10.2174/1874836800903010052

[21] PEER. Pacific Earthquake Engineering Research Center: Structural Engineering Reconnaissance of the August 17, 1999, Kocaeli (Izmit), Turkey, Earthquake. Report No. 2000/09, Berkeley, University of California, 2000.

[22] Governo D. Regulamento do Betão Armado (RBA), Decreto n.º 25948, 16 de Outubro, serie I, num. 240, Lisbon, 1935. (in Portuguese)

[23] Governo D. Regulamento de Estruturas de Betão Armado (REBA), Decreto n.º 47723, 20 de Maio, serie I, num. 119, Lisbon, 1967. (in Portuguese)

[24] CEN. EN ISO 6892-1:2009, Metallic materials – Tensile testing – Part 1: Method of test at ambient temperature. European Committee for Standardization, Brussels, Belgium, 2009.

[25] CEN, NP EN 1992-1-1, Eurocode 2, Design of concrete structures. Part 1-1: General rules and rules for buildings. European Committee for Standardization, Brussels, Belgium, 2010.

[26] IPQ. NP EN 12390-3:2011, Ensaios do betão endurecido. Parte 3: Resistência à compressão de provetes. Instituto Português da Qualidade, Caparica, Portugal, 2011. (in Portuguese)

[27] Karayannis CG, Chalioris KE, Sirkelis GM. Local retrofit of exterior RC beam-column joints using thin RC jackets – An Experimental study. *Earthquake Engineering and Structural Dynamics* 2008; 37:727-746.

[28] Antonopoulos CP, Triantafillou TC. Experimental investigation of FRP-strengthened RC beam-column joints. *Composites for Construction (ASCE)* 2003:7(1)39-49.

[29] Park YJ, Ang AHS, Wen YK. Damage-limiting aseismic design of buildings. *Earthquake Spectra* 1987:3(1)1-26. doi: 10.1193/1.1585416.

[30] Melo J, Varum H, Rossetto T, Costa AG. Cyclic response of RC beam-column joints reinforced with plain bars: An experimental testing campaign. In: Proceedings of the 15th World Conference on Earthquake Engineering. Lisbon, Portugal, 24-28 September, 2012. Paper No. 4799.

[31] Hakuto S, Park R, Tanaka H. Effect of deterioration of bond of beam bars passing through interior beam-column joints on flexural strength and ductility. *ACI Structural Journal* 1999:96(5)858-864. doi: 10.14359/740.

[32] Shiohara H. New Model for Shear Failure of RC Interior Beam-Column Connections. *Journal of Structural Engineering* 2001:127(2)152-160.

[33] CEN, NP EN 1998-1, Eurocode 8, Design of structures for earthquake resistance - Part 1: General rules, seismic actions and rules for buildings. European Committee for Standardization, Brussels, Belgium, 2010.

[34] Priestley MJN. Myths and fallacies in earthquake engineering, revisited, *The Mallet Milne Lecture*. IUSS Press, Pavia, Italy, 2003.

[35] Rossetto T, Elnashai A. Derivation of vulnerability functions for European-type RC structures based on observational data. *Engineering Structures* 2003:25(10)1241-1263. doi: 10.1016/S0141-0296(03)00060-9.

[36] Rossetto T. Vulnerability curves for the seismic assessment of reinforced concrete building populations. PhD Thesis, Imperial College London, UK, 2004.

[37] Karayannis CG, Sirkelis GM. Strengthening and rehabilitation of RC beam-column joints using carbon – FRP jacketing and epoxy resin injection. *Earthquake Engineering and Structural Dynamics* 2008:37:769-790.

[38] Favvata MJ, Izzuddin BA, Karayannis CG. Modelling exterior beam-column joints for seismic analysis of RC frame structures. *Earthquake Engineering and Structural Dynamics* 2008:37(13)1527-1548.

[39] Favvata MJ, Karayannis CG. Influence of pinching effect of exterior joints on the seismic behavior of RC frames. *Earthquakes and Structures* 2014:6(1):89-110.

[40] Hwang, SJ, Lee, HJ. Analytical model for predicting shear-strengths of interior reinforced concrete beam-column joints for seismic resistance. *ACI Structural Journal* 2000:97(1)35-44.

[41] Chalioris CE, Favvata MJ, Karayannis CG. Reinforced concrete beam-column joints with crossed inclined bars under cyclic deformations. *Earthquake Engineering and Structural Dynamics* 2008:37(6)881-897.

CHAPTER 5

CYCLIC TESTS ON EXTERIOR BEAM-COLUMN JOINTS NON-SEISMICALLY DESIGNED

Melo, J., Varum, H., Rossetto, T. Cyclic tests on exterior beam-column joints non-seismically designed. *ACI Structural Journal*, to be submitted in December 2014.

5.1 ABSTRACT

The reinforced concrete structures built in the past with plain reinforcing bars are commonly found in seismic regions. The seismic behaviour of these structures is sometimes limited by the slippage between the reinforcing bars and the surrounding concrete in elements as exterior beam-column joints. The anchorage of the beam reinforcing bars in the core joint with weak concrete confinement, inappropriate reinforcement detailing for seismic loads and poor bond properties is the reason for collapse of a larger number of structures. This chapter presents the results of four unidirectional cyclic tests and two unidirectional monotonic tests carried out on full-scale exterior beam-column joints built with plain and deformed reinforcing bars. These specimens are representative of reinforced concrete structures built without adequate reinforcement detailing for seismic loads. The influence of bond properties, lapping of the longitudinal bars, anchorage of the beam reinforcing bars and loading on the beam-column joints response are investigated.

5.2 INTRODUCTION

Recent earthquakes have showed the vulnerability of the existing reinforced concrete (RC) structures to seismic loading, particularly the beam-column joints. Inappropriate joint reinforcement detailing may lead the structural elements to a premature failure, especially for the case of exterior beam-column joints. Typically the failure mode in exterior joints with insufficient transverse reinforcement is concrete shear in the form of diagonal tension [1]. Slippage of the reinforcing bars can be another mechanism that may conditioned the seismic behaviour of the joints, especially in structures built with plain reinforcing bars and prior to the enforcement of the modern seismic-oriented designed codes. Cyclic loads such as those induced by earthquakes, cause progressive concrete-steel bond degradation, which can lead to significant bar slippage. As a result, the maximum strength capacity of the structure may not be reached and the elements' deformation might enlarge, leading to the premature collapse of the structure. The failure of old RC structures may be anticipated by other factors apart from bar slippage and lower concrete joint confinement, such as [2]: inadequate reinforcement detailing for seismic demands; lower compressive concrete strength; and designed only for gravity loads.

A significant part of the research has been performed on the design of new RC structures and improvement of design codes (for example [3,4,5,6]) and a lower amount of studies have been focus on the assessment and retrofitting of old RC structures [7,8,9,10,11,12,13,14,15,16], and the cyclic behaviour of existing RC elements is not yet fully understood.

This chapter presents the results of a series of monotonic and cyclic tests carried out on five full-scale exterior beam-column joints built with plain reinforced bars. The specimens were designed according to old RC codes and without seismic detailing in order to represent the typical exterior beam-column joint in existing RC buildings. Different reinforcement detailing was adopted in the specimens design. An additional joint specimen built with deformed reinforcing bars was cyclically tested and the results were compared with an analogous specimen built with plain bars. The main results in terms of global and local response of this testing campaign are presented and discussed, allowing the study of the influence on the response of exterior beam-column joints of: bond properties; lapping

of the longitudinal reinforcing bars on column; anchorage of the longitudinal beam reinforcing bars in the core joint; and lateral loading (monotonic and cyclic).

5.3 SPECIMENS DETAILING, MATERIAL PROPERTIES AND TEST SETUP

5.3.1 Detailing of joint specimens

An experimental campaign was performed in the Department of Civil Engineering at the University of Aveiro to describe the behaviour of existing exterior beam-column joints built with plain reinforcing bars under monotonic and cyclic loading. Five full-scale exterior beam-column joints were built with plain reinforcing bars and tested under lateral monotonic and cyclic loading until reach the rupture. Four specimens were design and detailed according to the first Portuguese codes for reinforcing concrete structures, RBA (1935) [17] and REBA (1967) [18]. Another specimen was built with poor anchorage (180º hooks) of the beam longitudinal reinforcement. An extra specimen was built with deformed reinforcing bars to study the influence of the bar surface on the response of the exterior beam-column specimens. All the specimens have inadequate shear transverse reinforcement detailing in the joint region in order to represent the typical existing RC structures designed only for gravity loads.

The specimens represent exterior beam-column joints at the first floor level of a four storey building and connect beams with 4.0m (157in) span and columns with 3.0m (118in) height. In the specimen's nomenclature adopted: i) the first letter (T) stands for exterior beam-column joint; ii) the second letter (P or D) refers to the reinforcing steel type (plain, P, or deformed, D); iii) the third letter refers to a specific reinforcing detailing.

The geometry, dimensions and reinforcing details of the specimens is presented in Figure 2.1. The cross-section dimensions are the same for all specimens being 0.25x0.25m^2 (9.84x9.84in^2) for columns and 0.25x0.40m^2 (9.84x15.75in^2) for beams. The anchorage of the longitudinal plain reinforcing bars consists in 180º end hooks except for specimens type TPA and TPB where the anchorage of the longitudinal reinforcing bars of the beam in the core joint consists in 90º bend followed by a straight length of 0.25m (9.84in) and ends with a 180º hook. The mandrel diameter and the straight prolongation after the hook are four times the bar diameter. In the specimen with deformed reinforcing bars 90º end hooks

with a 0.15m (5.9in) and 0.30m (11.8in) straight prolongation after the hook were adopted for columns and beam, respectively. The lapping length of the longitudinal plain reinforcing bars is equal to 30 times the bar diameter and it was defined according to the recommendations of the first Portuguese RC codes. The stirrups were anchored by 90º bends in all specimens and the core joint did not have stirrups.

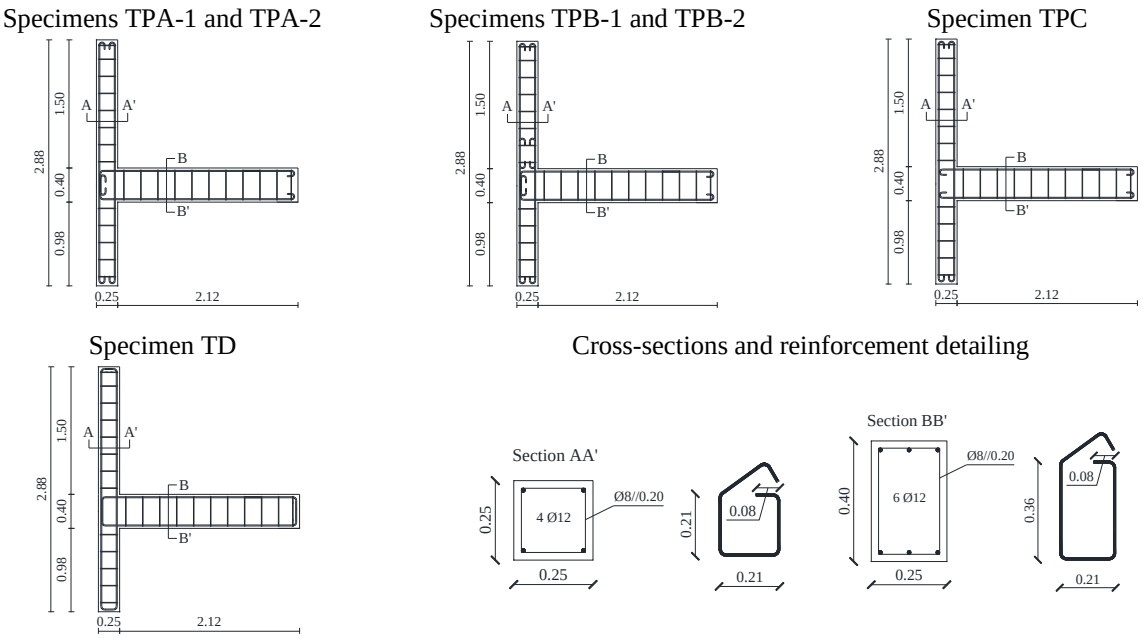

Note: Dimensions in meters (m). 1m=39.4in

Figure 5.1 – Specimens (geometry, dimensions and reinforcement detailing).

Specimens TPA-1 and TPA-2 have continuous longitudinal plain reinforcing bars and anchorage of the longitudinal reinforcing bars of the beam in the joint is made according to the first Portuguese RC codes. Specimen TPA-2 is assumed as reference specimen. Specimens TPB-1 and TPB-2 are similar to specimens TPA-1 and TPA-2 but with lap-splices in the longitudinal reinforcing bars located at the base of the superior column. Specimen TPC has continuous longitudinal plain reinforcing bars, but the longitudinal anchorage reinforcing bars of the beam in the joint is made with 180º end hooks, i.e. without the 90º bend followed by a straight length of 0.25m (9.84in) and 180º end hook as in specimens type TPA and TPB. Specimen TD is equivalent to specimens type TPA but was built with deformed reinforcing bars.

The longitudinal reinforcement of the columns consists of two bars with 12mm (0.47in) diameter in each lateral face. For beams the longitudinal reinforcement is constituted by three bars with 12mm (0.47in) diameter in the lower and upper faces. The

shear reinforcement of the columns and beams consists in stirrups with 8mm (0.32in) diameter, spaced at 0.20m (7.87in) centres. The core joint do not contains stirrups. The specimens were casted in the horizontal position and in different dates.

Hot-rolled plain and deformed bars with grades A235 and A400NRSD are used as reinforcement of the specimens with plain and deformed bars, respectively. Three tensile tests were performed on samples of each bar diameter according to the procedure in standard EN ISO 6892-1 (2009) [19] to characterize the mechanical properties. Concrete grade C16/20, according to EC-2 classification [20], was specified for the construction of the specimens. Compressive tests on concrete cylinder samples with dimensions 150mmx300mm (5.9inx11.8in) were carried out according to the standard NP EN 12390-3 (2011) [21]. All concrete samples were tested simultaneously with the test of the corresponding beam-column joint specimen, and at least after 90 days of curing. Table 5.1 summarises the mean properties of the concrete and steel used to build the specimens, where f_{cm} is the concrete compressive strength of cylinder samples, f_{ctm} is the tensile strength of concrete, f_{ym} is the yield strength of reinforcement steel, f_{um} is the ultimate tensile strength of reinforcement and E_{ym} is the Young's modulus of the reinforcement.

Table 5.1 – Concrete and steel mechanical properties (mean values).

Specimen	Concrete		Bar surface	Steel					
				Ø8 mm			Ø12 mm		
	MPa (ksi)			MPa (ksi)		GPa (ksi)	MPa (ksi)		GPa (ksi)
	f_{cm}	f_{ctm}		f_{ym}	f_{um}	E_{ym}	f_{ym}	f_{um}	E_{ym}
TPA-1	24.5 (3.55)	2.3 (0.33)	Plain	410 (59.5)	495 (71.8)	198 (28717)	405 (58.7)	470 (68.2)	199 (28863)
TPA-2	25.8 (3.74)	2.5 (0.36)							
TPB-1	15.8 (2.29)	2.0 (0.29)							
TPB-2	27.3 (3.95)	2.9 (0.42)							
TPC	23.8 (3.45)	2.6 (0.38)							
TD	21.5 (3.12)	2.4 (0.35)	Deformed	470 (68.2)	605 (87.7)	198 (28717)	465 (67.4)	585 (84.8)	199 (28863)

5.3.2 Test setup, loading conditions and monitoring

Figure 5.2 presents the loading conditions, lateral displacements history imposed, test-setup and monitoring scheme adopted in the tests. The specimens are tested in the horizontal position. Devices with reduced-friction characteristics are placed between the specimen and three concrete blocks, allowing the transfer of the weight of the specimen to the concrete blocks. The axial load (N) is imposed by a hydraulic actuator placed at the top

of the superior column associated to two tie rods linked to the base of the inferior column. To maintain the tie rods centred with the core joint during the test, two steel tubes are mounted at the base of the inferior column to extend the tie rods length. Therefore, the length of the tie rods in both sides of the joint (in the superior column and in the inferior column) is similar diminishing the second order effects at the columns' extremities. A constant axial load of 200kN (45 kip) is applied for all tests. The monotonic tests (specimens TPA-1 and TPB-1) consist in apply an increasing displacement at the top of the superior column in the negative direction up to 6% of drift. The cyclic tests are also carried out under displacement controlled conditions of the imposed lateral displacements. The displacements' history imposed consists in: three cycles applied for each of the following peak drift values (± %): 0.1, 0.2, 0.3 and then 0.5 to 3.5 with 0.5 increments (see Figure 5.2a). The lateral displacements are imposed with a velocity rate ranging from 0.1 for the first cycles to 1.5 mm/second (0.0039 to 0.059 in/second) for the last cycles.

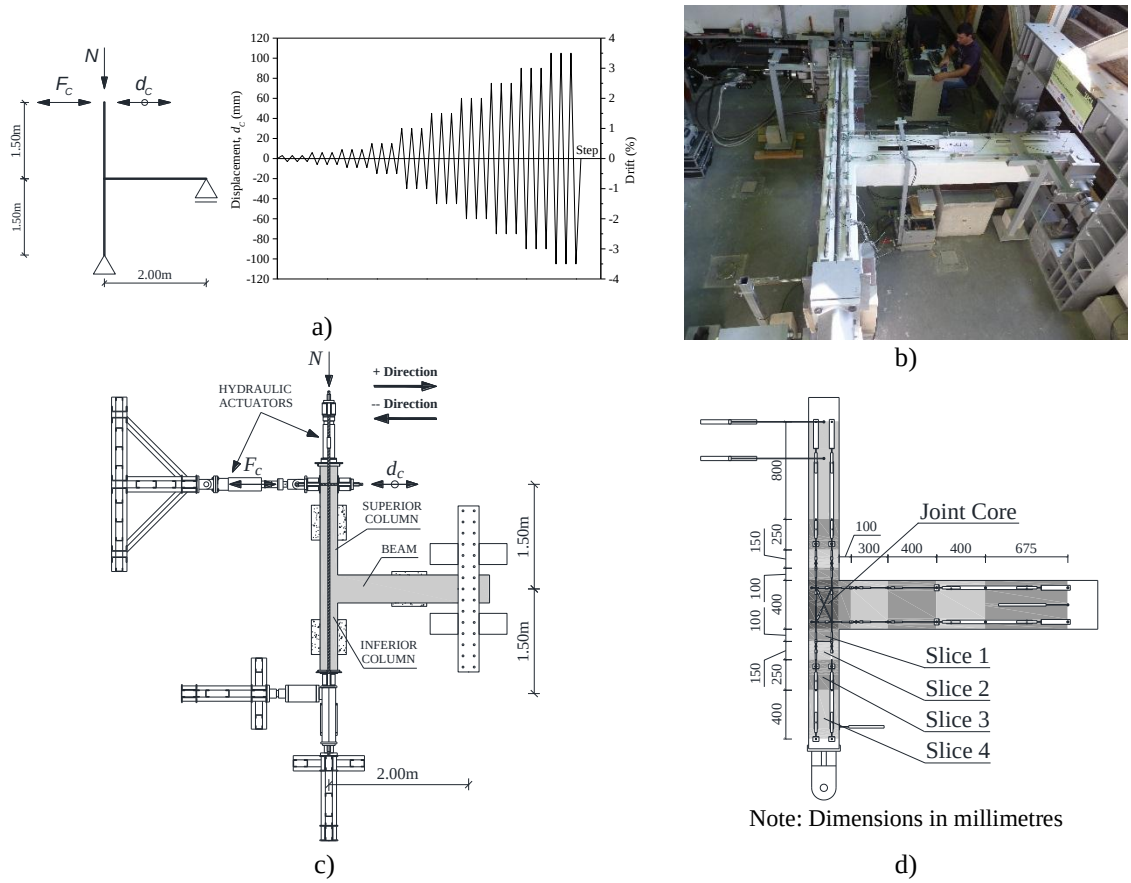

Note: 1mm = 0.001m = 0.0394 in.

Figure 5.2 – Test-setup and monitoring: a) support and loading conditions idealized and imposed lateral displacement history; b) general view; c) test setup schematics; and d) monitoring scheme.

Six Linear Variable Displacement Transducers (LVDTs) are placed at the top and base columns, at the end of the beam and in the core joint to measure the global displacements evolutions. For monitoring the relative displacements evolution in different points along the span of the elements are used twenty potentiometers and twelve LVDTs. The arrangement of the sensors is shown in Figure 5.2d. Each pair of parallel displacement sensors located in each column or beam allows the computation of the axial deformation and the relative rotation, from which is calculated the mean curvature in the slice.

5.4 EXPERIMENTAL RESULTS AND DISCUSSION

The experimental results are presented and discussed in this section, namely: hysteretic force-drift diagrams, force-drift envelopes, strength degradation, hysteretic dissipated energy evolution, equivalent damping-displacement ductility relationship, damages, HRC damage index, drift components and joint shear strength. Comparisons of the response obtained for the specimens are made in order to show the response differences due to: i) reinforcing steel surface; ii) lapping of the longitudinal reinforcing steel bars; iii) anchorage of the beam longitudinal reinforcement in the joint. The damage patterns observed at the end of the tests are also compared.

5.4.1 Global force-drift response and strength degradation

The cyclic lateral force-drift response and the force-drift envelopes of the specimens tested are presented in Figure 5.3 and Figure 5.4, respectively. Each plot of Figure 5.3 includes the response of two specimens aiming to highlight the differences for each variable under study, namely: bond properties (TPA-2 versus TD); lap-splice of the column longitudinal reinforcing bars (TPA-1 versus TPB-1 and TPA-2 versus TPB-2); and anchorage of the beam longitudinal reinforcing bars in the joint (TPA-2 versus TPC). In Figure 5.4 is also compared the force-drift envelopes of the cyclic tests with the monotonic test results to show the difference between cyclic and monotonic loading (TPA-1 versus TPA-2 and TPB-1 versus TPB-2). Figure 5.3 shows also the onset of each type of damage, namely: cracking on beam, cracking on columns, cracking on the core joint, concrete cover spalling and bar buckling.

Table 5.2 summarises the main values of the experimental response (for loading in positive direction) corresponding to: maximum force ($F_{c,max}$), drift at maximum force

($Drift_{Fc,max}$), ultimate force ($F_{c,ult}$) and drift at ultimate force ($Drift_{Fc,ult}$). The ultimate force was defined according to Park and Ang [22], i.e. when was observed a 20% strength reduction relatively to the maximum force.

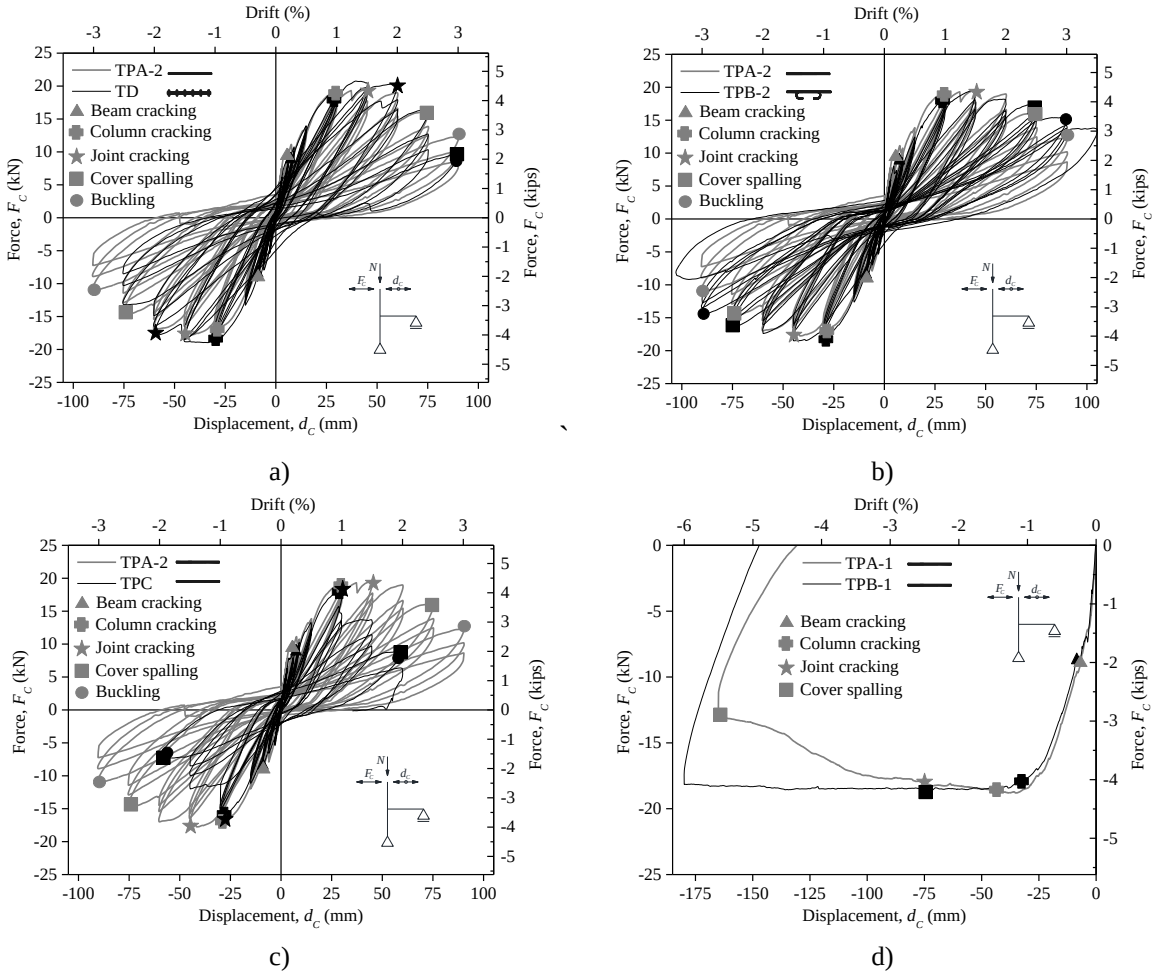

Figure 5.3 – Lateral force-drift relationships: a) TPA-2 versus TD; b) TPA-2 versus TPB-2; c) TPA-2 versus TPC; and d) TPA-1 versus TPB-1. (Note: 1mm = 0.0394in)

Generically, the cyclic response obtained was symmetric and the maximum strength and initial stiffness (in the positive direction) are similar for all specimens once that the material properties, cross-sections, load conditions and steel amount were similar in all specimens. However, considerable differences were observed on the response of the specimens in terms of damages, softening and strength degradation. The initial stiffness in the negative direction was around 20% lower than in the positive direction for all specimens loaded cyclically. In global terms, the cracking started at the beam for drift level of 0.2% and then at the columns for drift level of 1.0%, except in specimen TPA-1 that was 1.5%. None shear cracks were observed in specimens type TPB, but in the other specimens were observed shear cracks for drift levels ranging between 1.0% (specimen TPC) and

2.5% (specimen TPA-1). The cover spalling started for drift levels between 2.0% (specimen CPC) and 5.5% (specimen TPA-1). Bar buckling was observed in the core joint region for drift levels ranging from 2.0% (specimen TPC) and 3.0% (specimens TPA-2, TPB-2 and TD). In the monotonic tests was not observed bar buckling.

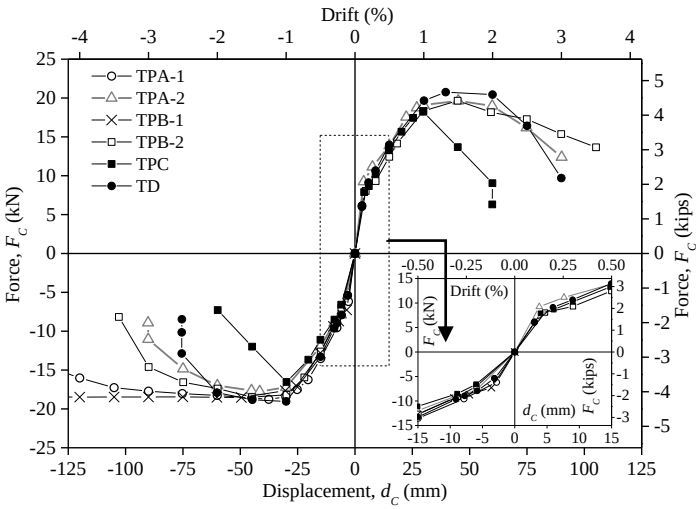

Figure 5.4 – Experimental force-drift envelopes. (Note: 1mm = 0.0394in)

Table 5.2 – Force and drift for the maximum strength and ultimate points.

Specimen	$F_{c,max}$ kN (kip)	$Drift_{Fc,max}$ %	$F_{c,ult}$ kN (kip)	$Drift_{Fc,ult}$ %
TPA-1	18.8 (4.23)	1.3	15.0 (3.37)	4.3
TPA-2	19.6 (4.41)	1.5	15.7 (3.53)	2.6
TPB-1	18.5 (4.16)	1.7	-	-
TPB-2	19.7 (4.43)	1.5	15.8 (3.55)	2.9
TPC	18.2 (4.09)	1.0	14.6 (3.28)	1.4
TD	20.8 (4.68)	1.3	16.6 (3.73)	2.5

The differences in the hysteretic response of specimens TPA-2 and TD (Figure 5.3a) were minor up to 2.5% drift once that the rupture of the specimens was mainly associated with the joint shear mechanism and not related with the bond properties. Therefore, was not evident that the bond properties have influenced the global cyclic response of the exterior beam-column joint with plain reinforcing bars. The lap-splice in the superior column of specimen TPB-2 did practically not influenced the hysteretic response when compared to specimen TPA-2, as well. However, the hysteretic response of specimen TPC showed larger softening and strength degradation than the reference specimen. Moreover, specimen TPC achieved the ultimate force for a drift demand of 1.4% while for the reference specimen was 2.6%. The weak anchorage of the beam longitudinal bars in the joint of specimen TPC lead to larger strength degradation and softening and the ultimate force was

reach for drift level that was almost half of the one for specimens with a proper anchorage detailing (TPA-2 and TPB-2). The specimens monotonically tested showed similar behaviour up to 2.0% drift and then softening was observed in specimen TPA-1 while in specimen TPB-1 a plateau was observed. Therefore, specimen TPA-1 reach the ultimate force for 4.3% drift and specimen TPB-1 did not achieved the ultimate force up to 6.0% drift. The response of specimens tested monotonically match with the force-drift envelopes of the corresponding specimens tested under cyclic loading up to achieve the maximum strength.

The strength degradation (SD) evolution (from 0.3% drift) between the first and second and between the first and third cycles of each drift peak is shown in Figure 5.5. In this figure is also present the best linear fitting curves and corresponding equations. In the equations the strength degradation and drift levels are expressed in percentage. For specimens TPA-2, TPB-2 and TD the strength degradation between the second and third cycles corresponds to 55% of the strength degradation between the first and second cycles. For specimen TPC this percentage is 74%. The fitted curves of specimens TPC and TD have the largest slopes, therefore the strength degradation for high drift levels was larger than in specimen CPA-2. In specimen CPB-2 the strength degradation was almost the same for all drift peaks.

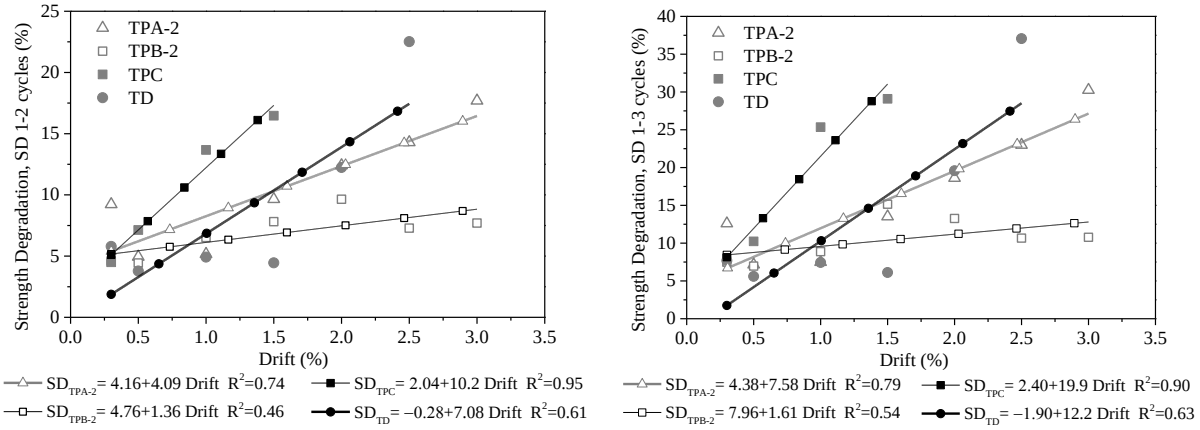

a) b)

Figure 5.5 – Strength degradation: a) between the first and second cycles; and b) between the first and third cycles.

5.4.2 Dissipated energy evolution

The hysteretic dissipated energy is a parameter that evaluate the capacity of the element to dissipate energy under cyclic loading. The structures well design for seismic loading

generically have larger capacity to dissipate energy than the others designed only for gravity loads. The hysteretic dissipated energy evolutions, calculated as the area under the experimental lateral force-displacement diagrams, are shown in Figure 5.6.

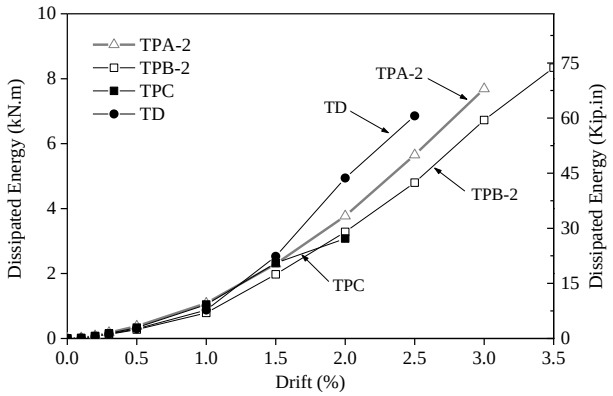

Figure 5.6 – Evolutions of the hysteretic dissipated energy.

The dissipated energy evolutions were similar for all specimens up to 1.5% drift, i.e. until reach the maximum strength. Then specimen TD had started dissipate more energy than the others specimens due to the better bond properties. At the end of the third cycle of 2.5% drift demand imposed, specimen TD dissipated more 21% and 43% than the reference specimen (TPA-2) and specimen TPB-2, respectively. Similar conclusions were observed by other authors for interior beam-column joints [8] and columns [23]. Specimen TPC had dissipated less 18% energy than the reference specimen at the end of the third cycle of 2.0% drift and was the specimen that had lower capacity to dissipate energy. Specimen TPB-2 dissipated less 13% energy than specimen TPA-2 for 3.0% drift which shows that the lap-splice of the longitudinal bars in the superior column may reduce the energy dissipation capacity.

The dissipated energy was also quantified by components (joint, beam and columns) for each drift demand level. Therefore, the results evidence the contribution of each component for the total energy. The dissipated energy is commonly associated with the damage in the RC elements, thereby elements with larger damage usually dissipate more energy than elements with lower damage level, i.e. elements without plastic hinge. The results here present are in agreement with the damages observed during the cyclic tests.

The dissipated energy at the joint was computed as the area under the lateral shear force versus joint distortion diagram. The horizontal shear force in the joint (V_{jh}) was calculated by Equation (5.1), where M_b is the beam moment at the face of the joint core,

j_d is the lever arm between the tensile forces and the centroid of the compressive force at the joint-beam interface (in this study the average value of j_d is $0.95 \cdot d$, where d is the effective depth), and V'_c is the shear force in the base of the superior column.

$$V_{jh} = \frac{M_b}{j_d} - V'_c \tag{5.1}$$

The dissipated energy at the beam and columns was computed integrating along the elements length the experimental moment-curvature results and assuming a linear distribution of the curvatures from the elements' extremity to the interface between slice 1 and slice 2 (see Figure 5.2d) and assuming a constant distribution of curvatures in slice 1.

The total dissipated energy calculated as the sum of the dissipated energy of the joint, beam and columns for each drift demand was compared with the corresponding experimental total energy dissipation (Figure 5.6). For drift levels between 0.2% and 3.5%, the sum of the dissipated energy computed independently (joint, beam and columns) represents in average 94% of the total experimental dissipated energy (coefficient of variance equals to 16%). Thus, the methodology adopted to compute the dissipated energy at the components give an estimative with good accuracy of the fraction of dissipated energy per component.

The evolutions of the dissipated energy contribution of the joint, beam and columns to the total dissipated energy are represented in Figure 5.7. The dissipate energy showed in Figure 5.6 is similar up to 1.5% drift for all specimens, but looking for each component (Figure 5.7) it had considerable differences between the specimens.

The relative dissipated energy percentage at the columns decreased up to 0.5% drift and then became constant or increased (TPB-2). The relative percentage of the beam increase up to 0.5% drift and then decreased. At the joint the relative percentage decreased up to 1.5% drift and then increased or became constant (TPB-2). At the end of the tests, the dissipated energy at the columns represented a percentage ranging from 10% (TPC) to 45% (TPB-2) of the total energy. For the beam the percentage varies between 45% (TPC) and 60% (TD). In global terms, the beam is the component that dissipated more energy when compared with joint and columns. The joint in specimen TPB-2 dissipated less energy than the joints of the other specimens because was not detected damage inside the joint as observed for the other specimens.

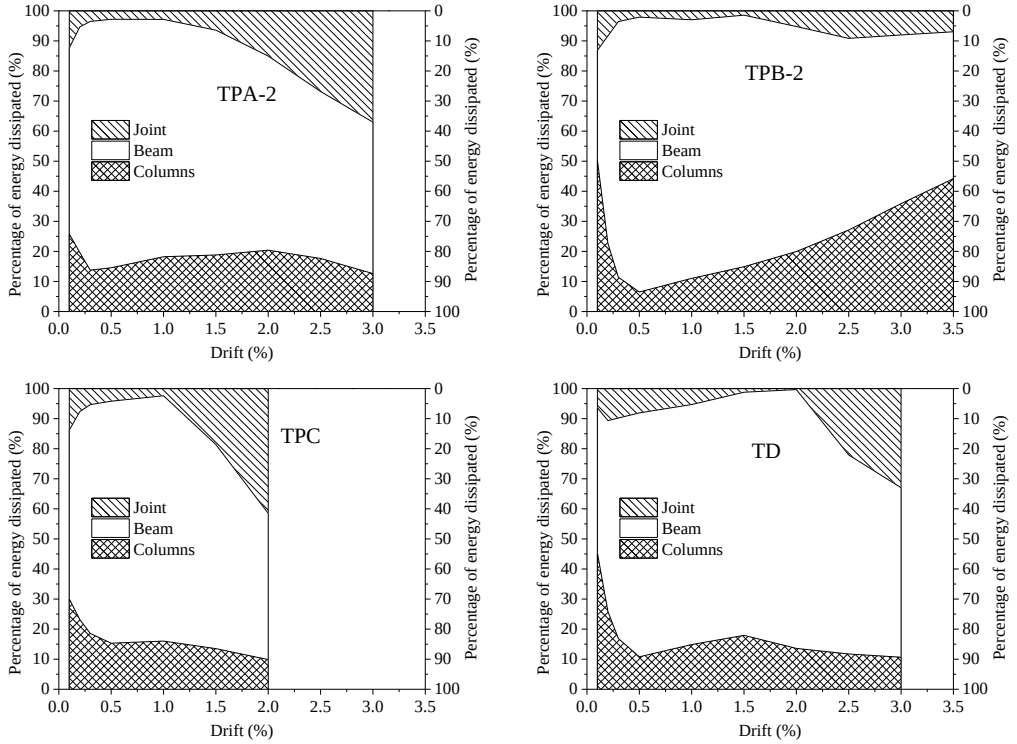

Figure 5.7 – Contribution to the total dissipated energy of different components: joint, beams and columns.

5.4.3 Displacement ductility and equivalent damping

The equivalent damping is commonly used to calibrate numerical macro-elements that represent the global behaviour of structural elements such as columns, beam-column joints and beams. The equivalent damping was calculated according to the methodology present in Varum [2]. Equation (5.2) was used to compute the equivalent damping, where $A_{half\text{-}loop}$ is the area within "half" force-displacement cycle and F_{max} and D_{max} are the maximum force and maximum displacement achieved in the respective half cycle.

$$\xi_{eq} = \frac{1}{\pi} \cdot \frac{A_{half-loop}}{F_{\max} \cdot D_{\max}} \tag{5.2}$$

The equivalent damping is presented in this work as a function of the displacement ductility. The displacement ductility was defined as the ratio between the maximum imposed displacement in each cycle and the yield displacement (Δ_y) that was calculated according to Annex B.3 of EC8-1 [24], being assumed an elastic-perfectly plastic force-displacement relationship. For each specimen, an elastic-perfectly plastic relationship was fitted to the experimental results up to the ultimate force of the force-displacement envelopes. For the fitting process, two requirements were satisfied (see Figure 5.8): i) the

areas under (A_1) and above (A_2) the experimental envelope curve must be equals; and ii) the area under or above the envelope curve is the minimum.

Table 5.3 resumes the yield force ($F_{c,y}$), the drift at yield ($Drift_y$), the displacement ductility at the ultimate force ($\mu_{\Delta,ult}$), of the fitted bi-linear curves. Table 5.3 also presents the equivalent damping value at the ultimate force ($\xi_{eq,ult}$) obtained from the best-fit curves (see Figure 5.9).

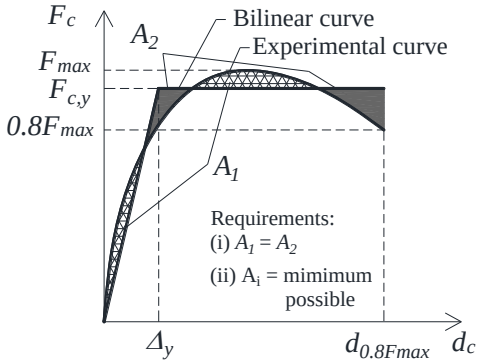

Figure 5.8 – Bilinear approach method adopted to find the yield displacement.

Table 5.3 – Yield force, yield drift, displacement ductility and equivalent damping at ultimate force.

Specimen	$F_{c,y}$ kN (kip)	$Drift_y$ %	$\mu_{\Delta,ult}$	$\xi_{eq,ult}$ %
TPA-1	17.7 (3.98)	0.58	7.47	-
TPA-2	17.6 (3.96)	0.59	4.30	9.96
TPB-1	18.3 (4.11)	0.66	-	-
TPB-2	17.4 (3.91)	0.60	4.86	9.49
TPC	16.0 (3.60)	0.58	2.40	12.57
TD	18.7 (4.20)	0.60	4.17	11.85

The yield drift was similar for all specimens, except specimen TPB-1 (see Table 5.3). However, the displacement ductility at ultimate force was almost 2 times less in specimen TPC than in the other specimens cyclically tested. The displacement ductility values at the ultimate force were in average 37% lower than the corresponding values obtained for interior beam-column joints built with plain reinforcing bars and tested in the same test setup [25]. This notable difference was related with the weaker concrete confinement and with the beam anchorage of the longitudinal reinforcing bars in the core of the exterior joints. Specimen TPC was the one with larger equivalent damping at ultimate force as a consequence of the simplify anchorage of the beam longitudinal reinforcing bars.

Specimen TD also had considerable larger (19% more) equivalent damping at ultimate force than the reference specimen.

The equivalent damping obtained from the experimental results, as function of the displacement ductility (μ_Δ) and the corresponding best-fit curves defined according to the general expression proposed by Priestley [26] (see Table 5.4) is presented in Figure 5.9. Specimens TPA-2 and TPB-2 had similar evolution of the equivalent damping with the increase of displacement demands. In specimen TPC, the increase of the equivalent damping with the displacement demands was more evident due to the early damage observed in the joint. In the specimen TD the initial damping of 4.4% (lower than in specimen TPA-2) and the larger damping increase with the displacement ductility than the reference specimen is in agreement with the conclusions other studies [8,25] performed on interior RC beam-column joints built with plain reinforcing bars.

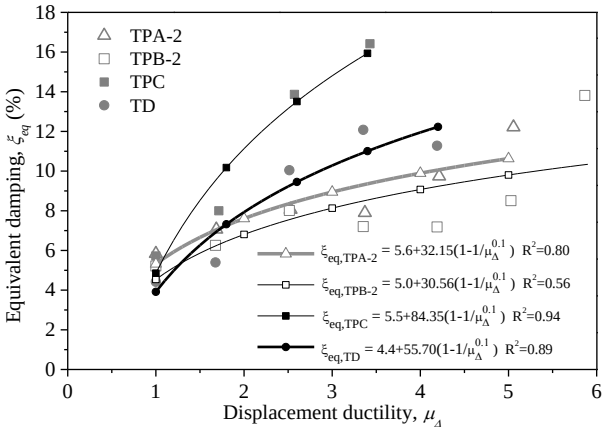

Figure 5.9 – Equivalent damping-displacement ductility diagrams.

Table 5.4 presents the general equivalent damping-displacement ductility equation proposed by Priestley [26] (Equation 5.3), the expression proposed by Melo et al. [23] (Equation 5.4) based on the experimental results of columns, the expression proposed by Melo et al. [25] based on experimental results of beam-column joints and other three curves (Equations (5.6) to (5.8)) that were fitted to the experimental results here presented and to experimental results of other authors [2,8]. Equations (5.4) to (5.8) are referenced to RC elements built with plain reinforcing bars. Equations (5.4) to (5.8) follow the generic form of Equation (5.3), considering β=0.1 and adopting for the parameter a and for the initial damping (ξ_0) the values resulting from the best-fit to the respective experimental results.

Table 5.4 – Equivalent damping-displacement ductility relationships.

Experimental data source	Elements type	Equation		Equation proposed in the literature
	Generic	$\xi_{eq} = \xi_0 + a \cdot \left(1 - \frac{1}{\mu^{\beta}}\right)$	(5.3)	Priestley [26]
	Columns	$\xi_{eq} = 3.8 + \frac{146}{\pi}\left(1 - \frac{1}{\mu^{0.1}}\right)$	(5.4)	Melo et al. [23]
	Interior beam-column joints	$\xi_{eq} = 5.9 + \frac{68}{\pi}\left(1 - \frac{1}{\mu^{0.1}}\right)$	(5.5)	Melo et al. [25]
Varum [2]	Structural response governed by column mechanisms	$\xi_{eq} = 3.5 + \frac{173}{\pi}\left(1 - \frac{1}{\mu^{0.1}}\right)$	(5.6)	
Fernandes et al. [8]	Interior beam-column joints	$\xi_{eq} = 4.8 + \frac{67}{\pi}\left(1 - \frac{1}{\mu^{0.1}}\right)$	(5.7)	
present experimental data	Exterior beam-column joints	$\xi_{eq} = 5.2 + \frac{134}{\pi}\left(1 - \frac{1}{\mu^{0.1}}\right)$	(5.8)	

Figure 5.10 compares the experimental results reported in this work with and the curves given by Equations (5.4) to (5.7). In the same figure is represented the curve fitted to the experimental results here reported (Equation 5.8). The best-fit curve given by Equation (5.8) better match with the curves obtained from experimental results of structures governed by column mechanisms or columns, Equations (5.4) and (5.6), than the curves obtained from experimental results of interior beam-column joints, Equations (5.5) and (5.7).

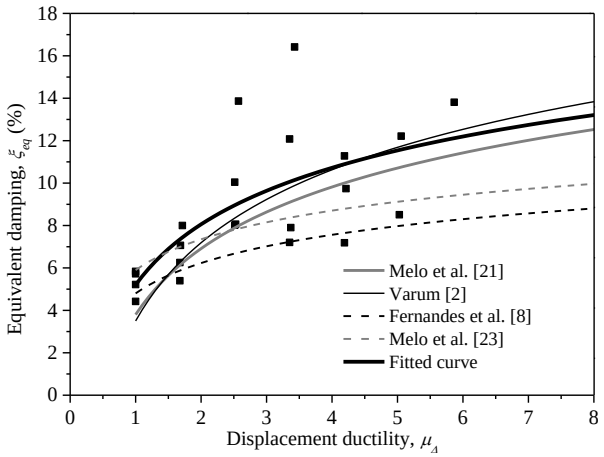

Figure 5.10 – Equivalent damping-displacement ductility diagrams: comparison between all experimental results and curves fitted to experimental results of other authors for elements with plain reinforcing bars [2,8,23,25].

5.4.4 Final damage state

The crack pattern observed on the top surface of the specimens at the end of the experimental tests is shown in Figure 5.11. For the cyclic tests two different failure modes were observed: i) shear failure of the core joint followed by concrete spalling and buckling of the exterior longitudinal reinforcing bars of the columns in the core joint (specimens TPA-2, TPC and TD); and ii) concrete spalling followed by buckling of the exterior longitudinal reinforcing bars of the columns in the core joint (specimen TPB-2). Buckling occurred due to the poor confinement in the joint as a consequence of no transverse reinforcement in this zone. The majority of the flexure cracks were located in the stirrups area due to the concrete discontinuity caused by the stirrups.

In specimen TPA-1 was observed some flexural cracks in the beam and shear cracks in the joint and in the other specimen monotonically loaded (TPB-1) flexural cracks in the beam and columns were observed at the end of the test. In specimen TPA-2 was registered flexural cracks in the beam and shear cracks in the joint. The crack pattern in the beam of specimen TPB-2 was similar to specimen TPA-2. However, in specimen TPB-2 no shear cracks were observed in the joint and larger cracks were recorded in the lap-splice zone of the longitudinal reinforcing bars of the superior column. In specimen TPC a large concrete spalling area (concrete wedge mechanism) was observed in the core joint due to the tension forces that the anchorage hook of the longitudinal rebars of the beam induce on the concrete and also because of the buckling of the external longitudinal rebars of columns in the core joint. Moreover, less amount of shear cracks were registered in the joint of specimen TPC when compared to specimens TPA-2 and TPB-2. In specimen TD, the concrete damage was more distributed along the beam' span than in the other specimens built with plain reinforcing bars, that is in agreement with observations made by other authors [8,23,25] as a consequence of the better bond conditions on the specimens built with deformed reinforcing bars.

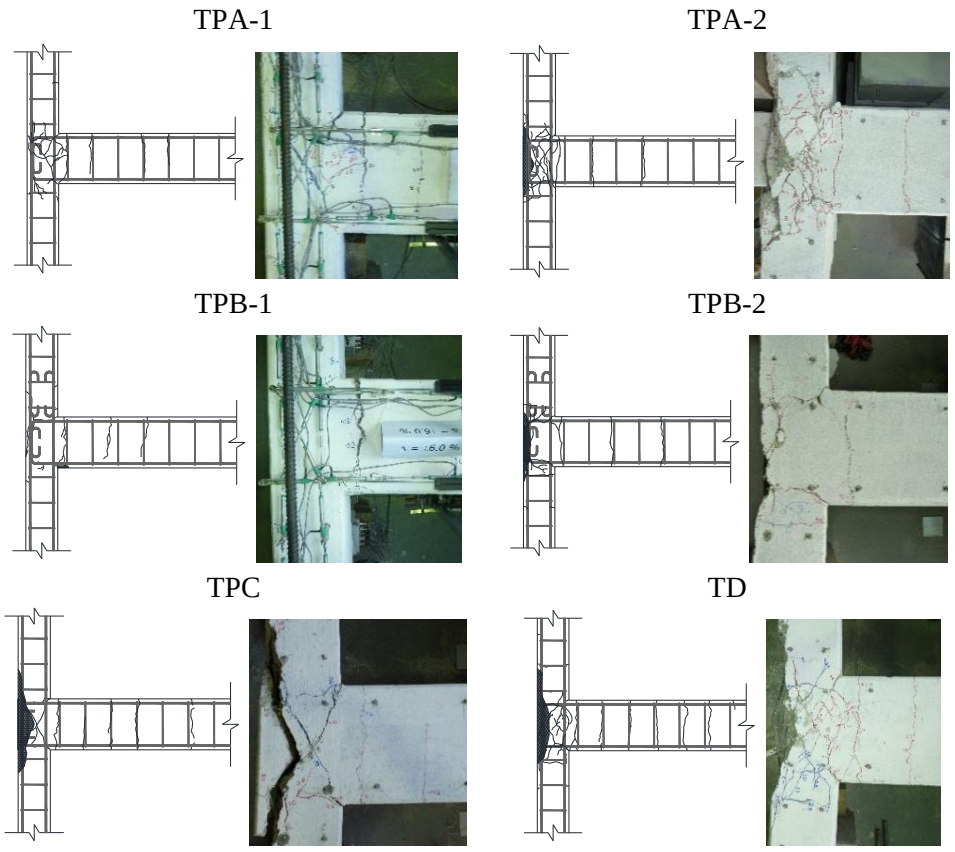

Figure 5.11 – Final damage state for the top face of the specimens.

5.4.5 HRC damage index

Rossetto and Elnashai [27] have developed the homogenised reinforced concrete damage scale (HRC-scale) that is a damage index used to generate vulnerability curves. This scale was calibrated to large scale experimental data [28] and was subdivided into seven damage states for non-ductile RC moment resisting frame structures (MRF) and other type of structures. The limit states are defined in terms of damage index and it is called HRC-damage index (DIHRC). This damage index provide a numerical reference scale (calibrated with experimental results) based on the maximum inter-storey drift ratio (called ISDmax% and in percentage). Equation (5.9) was proposed by Rossetto and Elnashai [27] to compute the HRC damage scale for non-ductile MRF.

$$DI_{HRC} = 34.89 Ln(ISD_{max\%}) + 39.39 \quad (5.9)$$

Figure 5.12 presents the experimental observations (cracking on the columns or beam, cracking on the joint, concrete cover spalling, bar buckling and ultimate force) and the HRC-damage scale index curve for non-ductile MRF given by Equation (5.9). The limits

of the seven damage states, namely: none; slight; light; moderate; extensive; partial collapse; and collapse are shown in Figure 5.12 as well. According to Rossetto and Elnashai [27], the damage registered in the tests, namely: columns or beam cracking, joint cracking, concrete cover spalling, bars buckling and ultimate point/force correspond to the HRC-damage index values of 20, 40, 60, 80 and 90, respectively. According to the HRC-scale, for bare non-ductile MRF, in this experimental campaign: the columns and beam cracking corresponds to the light damage state; the joint cracking and cover spalling correspond to the moderate damage state; buckling to the extensive damage state; and the ultimate point corresponds to structural partial collapse that corresponds to the collapse of the RC beam-column joints.

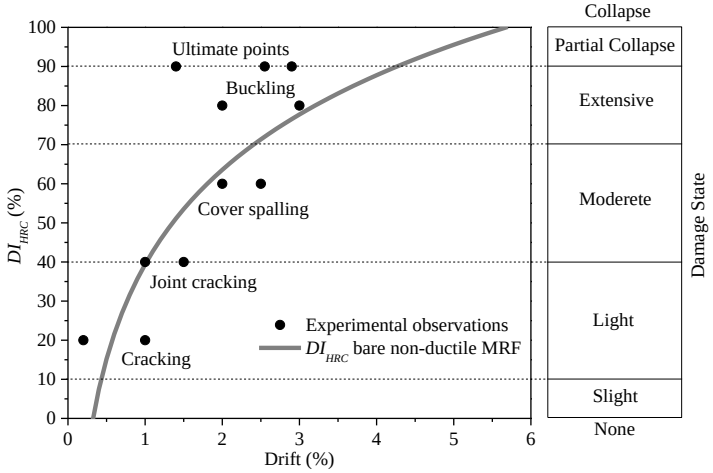

Figure 5.12 – HRC-damage index curve for bare non-ductile MRF and experimental observations.

The cracking, joint cracking and cover spalling experimental observations match well the corresponding predicted DIHRC values with Equation (5.9). However, bar buckling and the ultimate points were registered for smaller drift levels than the corresponding predicted DIHRC values. Therefore, the empirical DIHRC curve predicts with good agreement the experimental observations cracking (columns or beams and core joint) and concrete spalling, but does not predict well the bar buckling and ultimate force for exterior beam-column joints built with plain reinforcing bars and without stirrups in the core joint.

5.4.6 Displacement components

Several deformation mechanisms contribute to the lateral displacement (d_c) when it is imposed at the top of the superior column, namely: i) shear in columns; ii) bending in columns and beam; iii) joint relative rotation; and iv) joint shear distortion. The lateral

displacement at the top of the specimen was assumed in this section as the sum of the different deformation mechanisms above mentioned.

An elastic shear modulus (*G*) of 7.25GPa (1052ksi) and a constant shear distribution along the columns length were considering to compute the lateral displacement due to shear. The elastic shear modulus was calculated taking into account the Young's modulus of the concrete (estimated from the average concrete compressive strength) and considering a Poisson's ratio equal to 0.2.

The lateral displacement due to bending in columns and beam in this work was divided into components: a) linear elastic; and b) non-linear bending. The lateral displacement of each bending component was calculated according to the methodology present in [25] for interior beam-column joints built with plain reinforcing bars.

The "joint relative rotation" component represents the lateral displacement caused by the deformations in the core joint apart from the joint shear distortion, i.e. the contribution of the joint expansion and the relative rotation between the top and bottom joint sections. The lateral displacement of this component was calculated using the relative displacements measured by the diagonal potentiometers in the core joint to compute the relative joint rotation and then it was multiplied by the length of the column.

The displacement component due to joint shear distortion was determined based on the deformations measured by the potentiometers placed diagonally on the core joint and according to the methodology present in [29].

In general terms, a good agreement was found between the experimental and the analytical results (lateral experimental displacement versus analytical sum of each displacement mechanism), which permits to conclude that the methodology used allows well identify the deformation mechanism and their influence in the response of specimen. For drift values ranging from 0.3% to 3.0% the average difference observed between the analytical and the experimental results was 16% with a coefficient of variance equals to 0.11.

The contribution for the lateral displacement of the different deformation mechanisms: columns shear, linear elastic bending in columns and beam, non-linear bending in columns and beam, joint relative rotation and joint shear distortion, for drift demands ranging from 0.2% to the drift of the end of each test, is shown in Figure 5.13.

For small drift demands (up to 0,2%) the relative displacements measured in some potentiometers are close to their sensibility and thereby these results were excluded in this analysis.

The relative contribution of the shear deformation in columns to the lateral displacement was small for all specimens, signifying around 2.0% of the lateral displacement for 0.2% drift demand and 0.2% for 3.0% drift. These results are in accordance with observations made in similar tests carried out on interior beam-column joints [25].

For all specimens, the relative contribution of the elastic bending in columns and beam to the lateral displacement always decreased with the increased of the drift demands. For drift demands of 0.2% the elastic bending contribution represented between 70% (TPB-2) and 85% (TPA-2) of the total lateral displacement and then decreased almost linearly (except in specimens TPA-1 and TPB-1 where it decreased with a parabolic shape) until the end of the tests where it represented between 9% and 13% of the total displacement.

The relative contribution of the non-linear bending in columns and beam had different evolutions for each specimen. This deformation mechanism was directly related to the curvatures distribution along the elements, i.e. related with the different damages observed in columns and beam. Higher damages levels or larger crack opening means larger curvatures and as a consequence larger contribution for the lateral displacement. The specimens monotonically tested showed larger contribution of the non-linear bending, as a consequence of large width bending cracks in the beams, than the corresponding specimens cyclically tested.

The contribution of the joint relative rotation to the total lateral displacement increased with the damages in the core joint for drift demands larger than 1.0% for specimen TPC and 1.5% for the other specimens (onset of the shear cracks in the core joint) and may represents up to 70% (TPC) of the total displacement at the end of the test.

The contribution of the joint shear distortion to the lateral displacement also increased with the damage level in the core joint being almost zero at 0.2% drift and varying between 0.2% and 13% at the end of the tests.

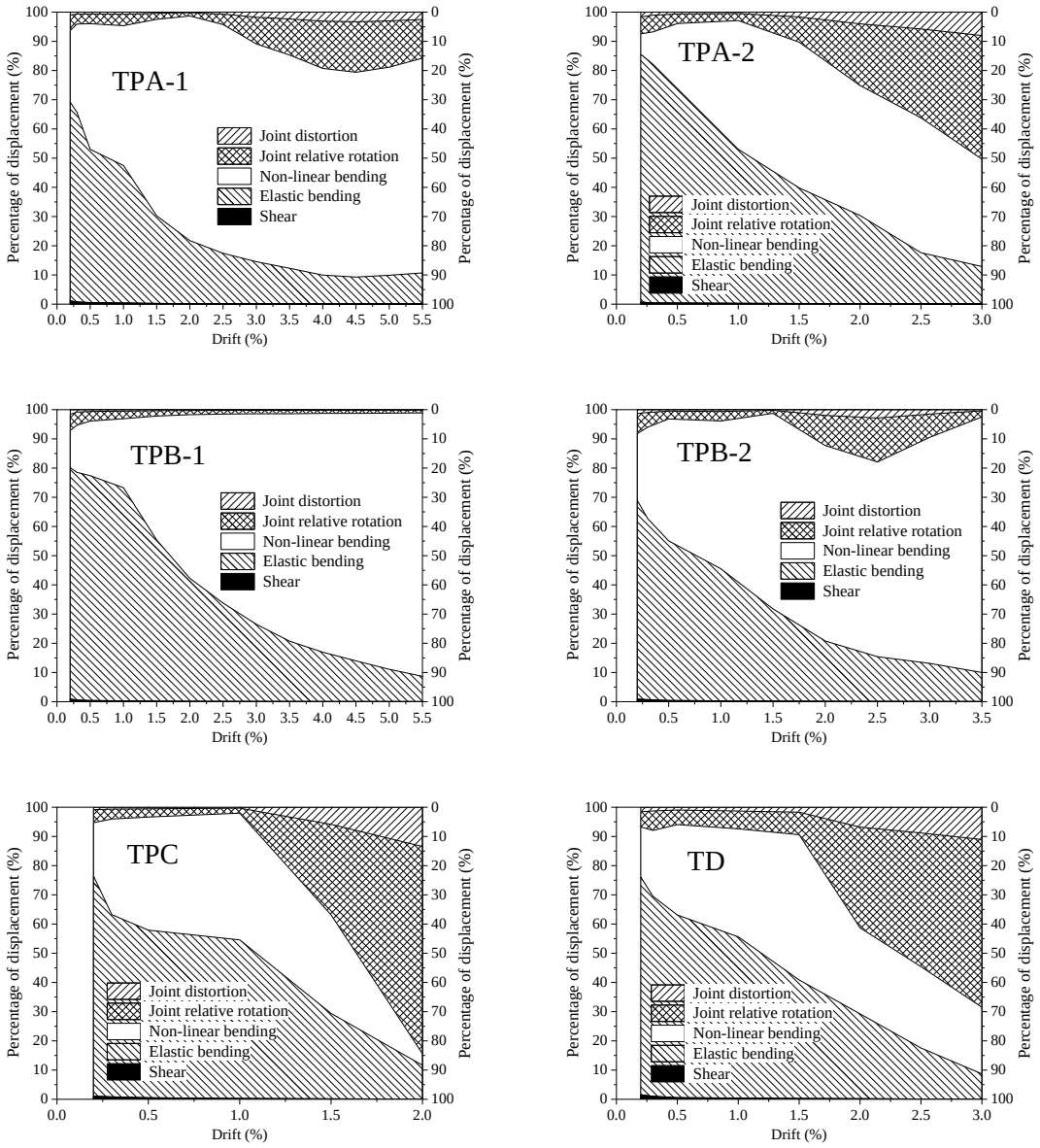

Figure 5.13 – Contribution to the total lateral displacement of the different deformation mechanisms: columns shear, linear elastic bending in columns and beam, non-linear bending in columns and beam, joint relative rotation and joint shear distortion.

Comparing the relative contributions to lateral displacement of the different deformation mechanisms of all specimens, there are evident differences between the results of the monotonic tests and the cyclic tests and also between the results of specimens TPB-2, TPC and TD when compared with the reference specimen. In specimen TPB-2 the contribution of the non-linear bending was larger than in the specimen TPA-2 and in specimen TPC the contribution of the joint relative rotation to the total lateral displacement was much more evident at the end of the test than in specimen TPA-2 due to the high damage level observed in the core joint of specimen TPC. In specimen TD the lateral displacement due

to joint relative rotation was larger (in opposition to the non-linear bending contribution) than in the reference specimen (TPA-2).

5.4.7 Joint shear strength

The shear stress in the core joint is commonly expressed as nominal shear stress or as principal compression/tensile stresses. The horizontal shear stress (v_{jh}) in the core joint can be calculated by Equation (5.10) [30], where V_{jh} is the horizontal shear force in the joint, calculated by Equation (5.1); b_c is the columns width; and h_c is the depth of the columns. Based on the Mohr's circle, the principal tensile stresses (p_t) at the mid-depth of the core joint is given by Equation (5.11), where f_a is the nominal axial compressive stress on the column calculated by Equation (5.12), and compressive stresses are taken as negative.

$$v_{jh} = \frac{V_{jh}}{b_c \cdot h_c} \tag{5.10}$$

$$p_t = \frac{f_a}{2} + \sqrt{\left(\frac{f_a}{2}\right)^2 + v_{jh}^2} \tag{5.11}$$

$$f_a = \frac{N}{b_c \cdot h_c} \tag{5.12}$$

Tsonos [30] proposed a formulation to predict the beam-column joint ultimate shear strength based on the strut-and-tie mechanism. This model assume biaxial concrete strength curve as a fifth-degree polynomial and solve this fifth-order polynomial equation. The normalized joint shear strength (γ) is determined by solving Equation (5.13), where x and ψ are terms expressed by the single variable γ given the aspect ratio between the column depth and the beam depth.

$$(x+\psi)^5 + 10 \cdot \psi - 10 \cdot x = 1 \tag{5.13}$$

Hwang and Lee [31] developed a joint strength model to satisfy equilibrium, compatibility and constitutive laws of cracked reinforced concrete. This model assumes that the joint shear resisting mechanisms are composed of three mechanisms: i) diagonal strut mechanism; ii) horizontal mechanism; and iii) vertical mechanism. The shear strength of the joint is defined when the compressive stress and strain of the concrete diagonal strut

reach a limit calculated in the calculating process. The stress and strain values are dependent on each other and an iterative procedure is needed to compute the joint shear strength.

In accordance with Eurocode 8 (EC8-1) [24], the diagonal compression induced in the joint by the diagonal strut mechanism shall not exceed the compressive strength of the concrete (f_c) in the presence of transverse tensile strains. For exterior joints, in the absence of a more precise model, the requirement may be satisfied if Equation (5.14) is fulfilled, i.e. if the horizontal shear force in the joint does not exceed $\overline{V}_{jh}^{EC8}$. In Equation (5.14), ν is the normalized axial load in the column above the joint, h_{jc} is the distance between extreme layers of column reinforcement and η is given by Equation (5.15), where f_{ck} is the characteristic compressive concrete strength in MPa.

$$V_{jh} \le 0.8 \cdot \eta \cdot fc \cdot \sqrt{1 - \frac{\nu}{\eta}} \cdot b_j \cdot h_{jc} = \overline{V}_{jh}^{EC8} \tag{5.14}$$

$$\eta = 0.6 \cdot \left(1 - f_{ck}/250\right) \tag{5.15}$$

ACI 318-11 [32] code express the shear strength of concrete in terms of square root of the concrete cylinder compressive strength (f_c). According to this code the nominal horizontal joint shear stress for exterior beam-column joint shall not exceed $1.0\sqrt{f_c}$ (f_c in MPa). The New Zealand code 3101-1 2006 [33] specifies that the horizontal shear stress should not exceed 0.2 f_c to avoid the diagonal compression failure by crushing.

Table 5.5 presents the maximum horizontal shear force in the joint ($V_{jh,max}$) and the corresponding drift ($\Delta_{Vjh,max}$), and the ratios between the maximum horizontal shear force in the joint and the: Tsonos prediction [30] ($\overline{V}_{jh}^{Tsonos}$); Hwang and Lee prediction [31] ($\overline{V}_{jh}^{Hwang\&Lee}$); EC8-1 [24] limit ($\overline{V}_{jh}^{EC8}$); ACI 318 [32] limit ($\overline{V}_{jh}^{ACI318}$); and NZS 3101-1 limit [31] ($\overline{V}_{jh}^{NZS3101}$). Equation (5.10) was used to transform the nominal horizontal joint shear stress limits present in ACI 318 and NZS 3101-1 to horizontal shear force. The maximum shear capacity predicted by both models as well as the codes limits are significantly larger than the experimental maximum horizontal shear force. Considering that in all specimens, except specimens type TPB, were observed shear cracks in the core joint, meaning that the maximum shear capacity was reached, the models and the codes overestimated the shear

capacity of the joints. The mean values (see Table 5.5) of the ratios between the experimental maximum shear force of the specimens with plain bars and the predicted values by the models and codes show that the best prediction was given by Hwang and Lee model, followed by EC8-1 limit, NZS 3101 limit, Tsonos prediction and ACI 318 limit. The two formulations and the codes did not take into account the bond and the anchorage characteristics of the reinforcement to predict the maximum shear strength and it may explain the overestimation of the shear strength.

For specimen TPB-1 the predictions were better than for the other specimens once that this specimen had lower compressive concrete strength than the other specimens and it was an important input in the considered models. For specimen TD the models and codes also overestimate the maximum shear capacity, but the difference between the experimental value and the analytical values was lower.

Table 5.5 – Maximum shear force ratios.

Specimen	$\Delta_{Vjh,max}$ **%**	$V_{jh,max}$ **kN (kip)**	$\frac{V_{jh,max}}{\overline{V}_{jh}^{Tsonos}}$	$\frac{V_{jh,max}}{\overline{V}_{jh}^{Hwang\&Lee}}$	$\frac{V_{jh,max}}{\overline{V}_{jh}^{EC8}}$	$\frac{V_{jh,max}}{\overline{V}_{jh}^{ACI318}}$	$\frac{V_{jh,max}}{\overline{V}_{jh}^{NZS3101}}$
TPA-1	-1.2	-131.7 (-29.6)	0.42	0.75	0.45	0.43	0.43
TPA-2	1.5	137.5 (30.9)	0.41	0.76	0.43	0.43	0.43
TPB-1	-2.4	-130.3 (-29.3)	0.61	0.97	0.94	0.52	0.66
TPB-2	1.5	137.7 (31.0)	0.39	0.73	0.40	0.42	0.40
TPC	1.0	126.6 (28.5)	0.41	0.74	0.46	0.42	0.43
Mean value			0.45	0.79	0.53	0.44	0.47
TD	1.3	145.4 (32.7)	0.62	0.90	0.62	0.50	0.54

The envelopes of the nominal principal tensile stresses – drift relationship are displayed in Figure 5.14. Based on the test observations, joint cracking starts when the maximum nominal principal tensile stress was achieved. The asymmetry of the plot present in Figure 5.7 was related to the difference of the axial load between the superior and inferior columns due to the beam reaction. For drift demands in the positive direction the axial load was lower in the inferior column than in superior column, but for the negative direction it reverses. For 1.5% drift the difference of the axial load in the inferior column between the positive and negative directions may represents 17% of the axial load imposed at the top of the superior column. The observed maximum principal tensile stresses were around three times lower than the ones present in Chalioris et al. 2008 [34] for exterior beam-column joints with X-bars in the core joint. In general terms, the nominal principal tensile stress was similar for all specimens up to reach the maximum stress and it increased linearly. In

specimen TPC was observed a significant drop after peak while in the other specimens the slope of the envelope curves was smaller.

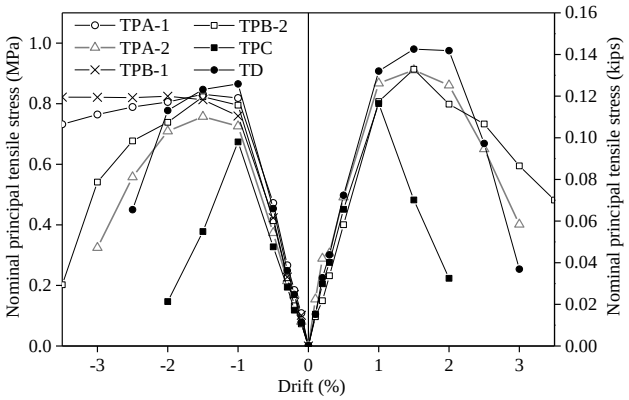

Figure 5.14 – Nominal principal tensile stresses.

5.5 CONCLUSIONS

This chapter describes an experimental campaign carried out for assessment the monotonic and cyclic behaviour of full-scale RC exterior beam-column joints built with plain bars and without seismic reinforcement detailing. Five specimens built with plain reinforcing bars and one with deformed reinforcing which represent the typical exterior beam-column joints in existing RC structures in the European Mediterranean countries until the 1970s were tested. The influence of reinforcing steel surface, lapping of the longitudinal reinforcing bars in the column, anchorage of the beam longitudinal reinforcing bars in the core joint and lateral loading history (monotonic or cyclic) on the response were investigated.

The global behaviour of specimen types TPA, TPB and TD was similar in terms of maximum strength, ductility, dissipated energy and equivalent damping. However, in specimen TPC the results were different than the other specimens. In this specimen was observed a premature failure as a consequence of the poor anchorage detailing of the beam reinforcing bars in the core joint that induced the concrete wedge mechanism. Therefore, the detailing of the anchorage has an important role on the joint cyclic behaviour and it may compromise the response of the RC structure.

The methodology adopted to compute the energy dissipated by the components (joint, columns and beam) represents in average 94% of the total experimental dissipated energy (coefficient of variance equals to 16%). Therefore, the methodology developed can estimate the dissipated energy of each component with accuracy. The beam had dissipated

more energy than the sum of columns and joint. The joint was the element that dissipate less energy.

Shear joint failure was observed for all specimens, except for specimens with lapping of the longitudinal bars in the superior column. The shear failure was a consequence of none transversal reinforcement in the core joint and it justify the important of improve the joint concrete confinement during the strengthening interventions in RC structures.

The nominal horizontal joint shear stress and corresponding horizontal shear force limits of EC8-1 [24], ACI 318 [32] and NZS 3101-1 [33] were not adequate for the exterior beam-column joints here studied. The limit of the codes was more than the double maximum horizontal shear force observed in the tests. Therefore, the formulations present in these codes may be reconsidered for the case of exterior beam-column joints without transverse reinforcement.

5.6 REFERENCES

[1] Antonopoulos CP, Triantafillou TC. Experimental investigation of FRP-strengthened RC beam-column joints. *Composites for Construction (ASCE)* 2003:7(1)39-49.

[2] Varum H. Seismic assessment, strengthening and repair of existing buildings. PhD Thesis, University of Aveiro, Portugal, 2003.

[3] Rodrigues H, Arêde A, Varum H, Costa AG. Experimental evaluation of rectangular reinforced concrete column behaviour under biaxial cyclic loading. *Earthquake Engineering & Structural Dynamics* 2013:42(2):239-259. DOI: 10.1002/eqe.2205.

[4] Rodrigues H, Varum H, Arêde A, Costa AG. A comparative analysis of energy dissipation and equivalent viscous damping of RC columns subjected to uniaxial and biaxial loading," *Engineering Structures* 2012:35:49-164. doi: 10.1016/j.engstruct.2011.11.014.

[5] Fardis M. Seismic Design, Assessment and Retrofitting of Concrete Buildings, based on EN-Eurocode 8. *Geotechnical, Geological, and Earthquake Engineering, Springer* 2009:8:744.

[6] IUSS Press. Guidelines for Displacement-based Design of Buildings and Bridges. Risk Mitigation for Earthquakes and Landslides. LESSLOSS Report No. 2007/05, Pavia, Italy, 2007.

[7] Melo J, Fernandes C, Varum H, Rodrigues H, Costa AG, Arêde A. Numerical modelling of the cyclic behaviour of RC elements built with plain reinforcing bars. *Engineering Structures* 2011:33:2:273-286. doi: 10.1016/j.engstruct.2010.11.005.

[8] Fernandes C, Melo J, Varum H, Costa AG. Cyclic behaviour of substandard RC beam-column joints with plain bars. *ACI Structural Journal* 2013:110:1:137-148. doi: 10.14359/51684337.

[9] Fernandes C. Cyclic behaviour of RC elements with plain reinforcing bars. PhD Thesis, University of Aveiro, Portugal, 2012.

[10] Liu A, and Park R. Seismic Behaviour and Retrofit of Pre-1970's As-Built Exterior Beam-Column Joints Reinforced by Plain Round Bars. *Bulletin of the New Zealand Society for Earthquake Engineering* 2001:34:1:68-81.

[11] Fernandes C, Melo J, Varum H, Costa AG. Cyclic behavior of a two-span RC beam built with plain reinforcing bars. *Periodica Polytechnica Civil Engineering* 2011:55:1:21-29. doi: 10.3311/pp.ci.2011-1.03.

[12] Bousias S, Spathis AL, Fardis MN. Seismic retrofitting of columns with lap spliced smooth bars through FRP or concrete jackets. *Journal of Earthquake Engineering* 2007:11:5:653-674. doi: 10.1080/13632460601125714.

[13] Di Ludovico M, Verderame G, Prota A, Manfredi G, Cosenza E. Cyclic Behavior of Non-Conforming Full Scale RC Columns. *Journal of Structural Engineering* 2014:140:5. doi: 10.1061/(ASCE)ST.1943-541X.0000891.

[14] Esmaeeli E, Barros J, Sena-Cruz J, Varum H, Melo J. Assessment of the Efficiency of Prefabricated Hybrid Composite Plates (HCPs) for Retrofitting of Damaged Interior RC Beam-Column Joints. *Composite Structures* 2015:119:24-27. doi: 10.1016/j.compstruct.2014.08.024

[15] Russo G, Pauletta M. Seismic behavior of exterior beam-column connections with plain bars and effects of upgrade. *ACI Structural Journal* 2012:109:2:225-233.

[16] Braga F, Gigliotti R, Laterza M. R/C existing structures with smooth bars reinforcing bars: experimental behaviour of beam-columnn joints subject to cyclic lateral loads. *The Open Construction & Building Technology Journal* 2009:3:52-67.

[17] Governo D. Regulamento do Betão Armado (RBA), Decreto n.º 25948, 16 de Outubro, serie I, num. 240, Lisbon, 1935. (in Portuguese)

[18] Governo D. Regulamento de Estruturas de Betão Armado (REBA), Decreto n.º 47723, 20 de Maio, serie I, num. 119, Lisbon, 1967. (in Portuguese)

[19] CEN. EN ISO 6892-1:2009. Metallic materials – Tensile testing – Part 1: Method of test at ambient temperature. European Committee for Standardization, Brussels, Belgium, 2009.

[20] CEN, NP EN 1992-1-1, Eurocode 2, Design of concrete structures. Part 1-1: General rules and rules for buildings. European Committee for Standardization, Brussels, Belgium, 2010.

[21] IPQ. NP EN 12390-3:2011, Ensaios do betão endurecido. Parte 3: Resistência à compressão de provetes. Instituto Português da Qualidade, Caparica, Portugal, 2011. (in Portuguese)

[22] Park YJ, Ang AH, Wen YK. Damage-limiting aseismic design of buildings," Earthquake Spectra 1987:3:1:1-26. doi: 10.1193/1.1585416

[23] Melo J, Varum H, Rossetto T. Experimental Cyclic Behaviour of RC Columns With Plain Bars And Proposal For Eurocode 8 Formula Improvement. *Engineering Structures* 2014. Resubmitted after revision by authors; under review.

[24] CEN. NP EN 1998-1. Eurocode 8, Design of structures for earthquake resistance - Part 1: General rules, seismic actions and rules for buildings. European Committee for Standardization, Brussels, Belgium, 2010.

[25] Melo J, Varum H, Rossetto T. Cyclic Behaviour of Interior Beam-Column Joints Reinforced With Plain Bars. *Earthquake Engineering and Structural Dynamics* 2014. doi: 10.1002/eqe.2521.

[26] Priestley MJ. Myths and fallacies in earthquake engineering, revisited. The Mallet Milne Lecture. IUSS Press, Pavia, Italy, 2003.

[27] Rossetto T, Elnashai A. Derivation of vulnerability functions for European-type RC structures based on observational data. *Engineering Structures* 2003:25:10:1241-1263. doi: 10.1016/S0141-0296(03)00060-9.

[28] Rossetto T. Vulnerability curves for the seismic assessment of reinforced concrete building populations. PhD Thesis, Imperial College London, UK, 2004.

[29] Shiohara H. New Model for Shear Failure of RC Interior Beam-Column Connections. *Journal of Structural Engineering* 2001:127:2:152-160.

[30] Tsonos AG. Cyclic Load Behavior of RC Beam-Column Subassemblages of Modern Structures. *ACI Structural Journal* 2007:104:4:468-478.

[31] Hwang SJ, Lee HJ. Analytical Model for Predicting Shear Strength of Exterior RC Beam-Column Joints for Seismic Resistance. *ACI Structural Journal* 1999:96:5:846-857.

[32] ACI Committee 318. Building Code Requirements for Structural Concrete (ACI 318-11) and Commentary (318-11). American Concrete Institute, Farmington Hills, 2011.

[33] NZS Committee P3101. Concrete Structures Standard, Part 1 – The design of Concrete Structures, NZS 3101-1:2006. New Zealand Standard, 2006.

[34] Chalioris CE, Favvata MJ, Karayannis CG. Reinforced concrete beam-column joints with crossed inclined bars under cyclic deformations. *Earthquake Engineering and Structural Dynamics* 2008:37:6:881-897.

CHAPTER 6

NUMERICAL MODELLING OF RC COLUMNS AND A NEW STEEL MODEL FOR ELEMENTS WITH PLAIN BARS

Melo, J., Varum, H., Rossetto, T. Numerical modelling of RC columns and a new steel model for elements reinforced with plain bars. *Eng. Structures*, submitted in December 2014.

This chapter presents the non-linear modelling models of two RC columns (CPA-3 and CD) presented in Chapter 3.

6.1 ABSTRACT

Cyclic load reversals (like those induced by earthquakes) result in accelerated bond degradation, leading to significant bar slippage. The bond-slip mechanism is reported to be one of the most common causes of damage and even collapse of existing RC structures subjected to earthquake loading. RC structures with plain reinforcing bars, designed and built prior to the enforcement of the modern seismic-oriented design philosophies, are particularly sensitive to bond degradation. However, currently perfect bond conditions are typically assumed in the numerical analysis of RC structures.

This chapter describes the numerical modelling of the cyclic response of two RC columns, one built with deformed bars and the other with plain bars, both with structural detailing similar to that typically adopted in pre-1970s structures. For each column, different software and modelling strategies to simulate the cyclic response were adopted. Numerical models were developed using the OpenSees and the SeismoStruct platforms,

and calibrated with the available tests results, reported in Chapter 3. Bond-slip effects were included in the models developed in OpenSees resorting to a simple modelling strategy. Basically, a new tri-linear steel material is proposed and adopted to take into account the slippage of plain reinforcing bars by reducing the steel Young modulus. The parameters that define the tri-linear steel model were empirically obtained, based on the experimental results.

6.2 INTRODUCTION

The hysteretic behaviour of reinforced concrete (RC) structures is highly dependent on the interaction between concrete and steel. Cyclic load reversals (like those induced by earthquakes) result in accelerated bond degradation, which may lead to significant relative slippage between the reinforcing bars and the surrounding concrete. Plain reinforcing bars, which are present in a large number of existing RC structures that were designed and built before the 1970s, thus prior to the enforcement of the modern seismic-oriented design philosophies, have poor bond properties between concrete and steel. Therefore, RC elements containing this type of steel reinforcement are particularly sensitive to the effects of bar slippage, as reported in Ioannou et al. [1] and Rossetto et al. [2].

In the analysis of RC structures, perfect bond is usually assumed, i.e. considering compatibility between concrete and reinforcement strains at each structural member point. However, this assumption is only correct for early loading stages and low strain levels. For large loads, cracking and bond failure will occur and bar slippage takes place in the structural elements [3,4]. Considering the assumption of perfect bond conditions may lead to predicted lateral deformation significantly smaller than the real element deformation or to predicted lateral stiffness larger than the existing element stiffness [5]. Bond-slip effects should therefore be included in the numerical models of structural analysis in order to represent more accurately the elements response as stated [6-8].

This chapter describes the numerical modelling of the cyclic response of two analogous RC columns, one with deformed bars and the other with plain bars, both with structural detailing similar to that typically found in RC structures designed and built before the 1970s (that is, without specific details for seismic demands). For each column, different models were built with the OpenSees and the SeismoStruct platforms, and within each platform different types of column elements were used to represent the column.

Particular attention was given to the effects of bar slippage, which were incorporated in the OpenSees models resorting to a simple modelling strategy. The results of the cyclic tests previously conducted on the columns were used to calibrate the adopted models. After describing the models, comparisons are established between the numerical and experimental results in order to conclude about their adequacy to simulate the columns response, and about the importance of including the effects of bar slippage.

A new tri-linear steel material is also proposed to take into account the slippage of plain reinforcing bars. The experimental results of tests carried out on columns [9] were used to calibrate the monotonic tri-linear steel model. The results obtained from the numerical models with and without considering the tri-linear steel model are compared with experimental results.

6.3 NUMERICAL MODELLING OF RC COLUMNS UNDER CYCLIC LOADING

This section presents the specimens detailing, material properties and loading conditions of two reinforced concrete columns, one built with deformed reinforcing bars and another built with plain reinforcing bars. A numerical parametric study of the columns is also here presented. OpenSees and SeismoStruct platforms were used to develop the numerical models. Different strategies were adopted to simulate the bond-slip mechanism in the model of the specimen with plain reinforcing bars.

6.3.1 Specimens detailing, material properties and loading conditions

The two columns under study are part of a larger experimental campaign carried out in the Department of Civil Engineering at the University of Aveiro and presented in Melo et al. [9]. Figure 6.1 shows the geometrical characteristics and reinforcement detailing of both specimens. Specimen CPA-3 and specimen CD were built with plain and deformed reinforcing bars, respectively. Both specimens have the same geometry dimensions and amount of steel reinforcement and were built in full-scale. Each specimen consisted of a column with 0.30x0.30m^2 square cross-section and length equal to 2.17m, and of a foundation made by a stiff RC block with 0.30x0.60m^2 cross-section and length equal to 1.5m. It should be noted that the columns' foundation was not considered in the numerical models developed.

Table 6.1 presents the mean values of the material properties of the concrete and steel reinforcement used in the specimens, where f_{cm} is the concrete compressive strength of cylinder samples with dimensions of 150mmx300mm (5.9inx11.8in), f_{ctm} is the axial tensile strength of concrete, f_{ym} is the yield strength of reinforcement, f_{um} is the ultimate tensile strength of reinforcement and E_{ym} is the Young's modulus of the reinforcing steel.

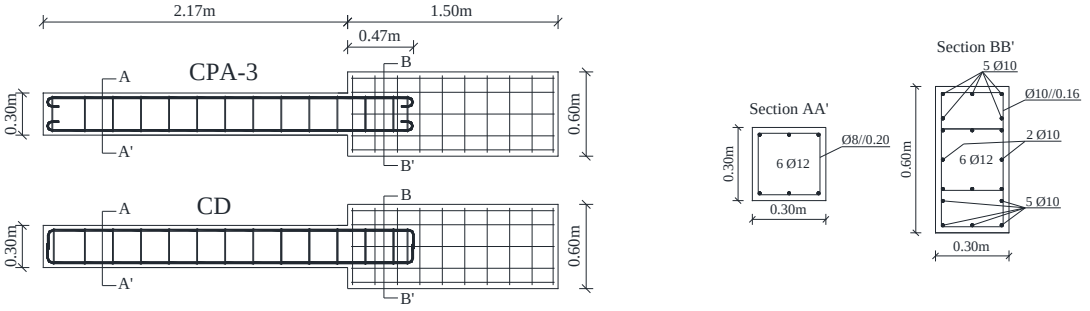

Figure 6.1 – Column specimens: a) dimensions and reinforcement detailing; b) cross-sections.

Table 6.1 – Mean values of the materials (concrete and steel) mechanical properties.

Column Specimen	Concrete		Bar surface	Steel					
				Ø8 mm			Ø12 mm		
	MPa			MPa		GPa	MPa		GPa
	f_{cm}	f_{ctm}		f_{ym}	f_{um}	E_{ym}	f_{ym}	f_{um}	E_{ym}
CPA-3	17.4	2.1	Plain	410	495	198	405	470	199
CD	17.1	2.0	Deformed	470	605	198	465	585	199

The imposed loading conditions and the lateral displacement history (d_c) are shown in Figure 6.2. The experimental tests were performed under displacement-control conditions. The lateral displacements were imposed at 1.7m from the column base (see Figure 6.2a). The axial load (N) was kept constant during the tests and equal to 305kN (axial load ratio, v, equals 19.5%). The axial load imposed by the testing setup is centred at the column' base. Therefore, P-delta effects are not considered in the numerical models.

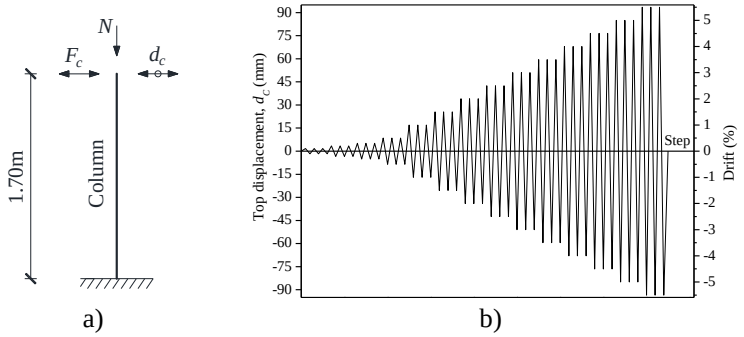

Figure 6.2 – a) Support and loading conditions idealized; b) imposed lateral displacement history.

6.3.2 Numerical modelling with OpenSees

The Open System for Earthquake Engineering (OpenSees) is an open source software framework for finite element analysis. It was developed to simulate the response of structural and geotechnical systems subjected to earthquakes. For frame structural members OpenSees performs common fibre-based analysis. The flexural member is represented by unidirectional steel and concrete fibres which are assumed to be characterized by the selected material stress-strain relationship as adopted by Spacone et al. [10] in numerical models of RC columns subjected to uniaxial and biaxial loading. The member stiffness and forces are obtained by numerically integrating the stiffness and forces of sections along the member length. The section deformation is used to obtain the strain in each fibre, based on the plane section assumption. The fibre stress and stiffness are updated according to the corresponding material models, followed by upgrading of the section force resultant and the corresponding stiffness [11].

For each column specimen, four nonlinear models were developed, namely: i) with *nonlinearBeamColumn element*, i.e. with distributed plasticity; ii) with *BeamWithHinges element*, in which the plasticity is considered to be concentrated over specified hinge lengths at the element ends; iii) with *nonlinearBeamColumn element* and *zero-length section element*; and, iv) with *BeamWithHinges element* and *zero-length section element*. The *zero-length section element* was incorporated to simulate the bar slippage effects associated with the strain penetration and the bond-slip mechanism.

6.3.2.1 NonlinearBeamColumn element

The *nonlinearBeamColumn element* is based on the non-iterative (or iterative) force formulation and considers the spread of plasticity along the element [11]. The integration along the element is based on Gauss-Lobatto quadrature rule. The element is prismatic and it is represented by fibre sections at each integration point (see Figure 6.3). In this study, five integration points were adopted for the column element.

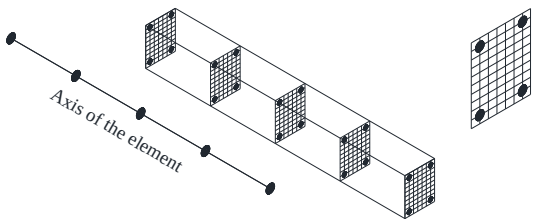

Figure 6.3 – *NonlinearBeamColumn element* with spread plasticity and five integration points.

6.3.2.2 BeamWithHinges element

The *BeamWithHinges element* is based on the non-iterative (or iterative) flexibility formulation [12]. The element considers plasticity to be concentrated over specified hinge lengths at the elements ends (plastic hinges). This element is divided into three parts: two hinges at the ends and a linear-elastic region in the middle. The Gauss integration points are located in the hinge regions.

In the models under investigation, the length adopted for the plastic hinges correspond to the values observed in the cyclic tests (as discussed in Chapter 3), that is, 0.30m for the column specimen with plain reinforcing bars and 0.35m for the specimen with deformed reinforcing bars.

6.3.2.3 Zero-length section element

The *zero-length section element* available in OpenSees has a unit-length such that the element deformations are the same that the section deformations. The unit length assumption also implies that the material model for the steel fibres in the *zero-length section element* represents the bar slip instead of strain for a given bar stress. Therefore, a specific material model, defined by a bar stress-slip relationship, should be assigned to the steel fibres of the *zero-length section element*. If placed at the end of a column element, this element can be used to incorporate the fixed-end rotation caused by strain penetration and bond-slip to the column element [12]. A duplicate node (two nodes with the same coordinates) is required to define the *zero-length section element*. Because the shear resistance is not included in the element, the relative translational degree-of-freedom of these nodes should be constrained to each other to prevent sliding of the column element under lateral loads.

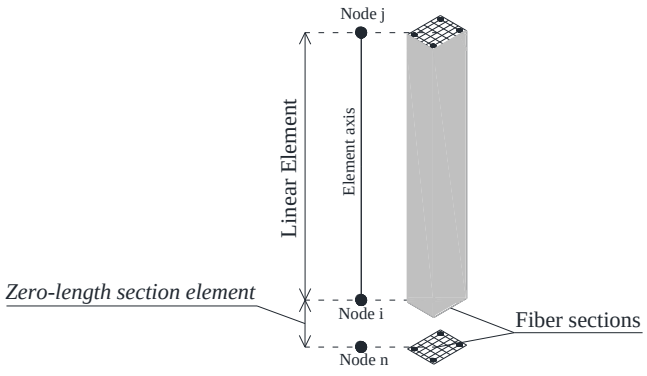

Figure 6.4 – Linear element and *zero-length section element*.

In the models under investigation, the *zero-length section element* was placed at the base of the column element (Figure 6.4), coincident with the node to which were assigned the restraints that simulate the columns' support conditions adopted in the cyclic test.

6.3.2.4 Material models adopted

In the numerical models, the *Concrete02* model and *Steel02* model were adopted for the concrete and steel reinforcement, respectively. It should be noted that the elastic part of the *BeamWithHinges element* was modelled using an elastic material with the same elastic modulus of the concrete. The *Concrete02* model was also assigned to the concrete fibres of the *zero-length section element*. The concrete model considers the concrete tensile strength, and takes into account the confinement effect due to the longitudinal bars and the stirrups based on the law proposed by Hognestad [13] and adapted by Guedes [14]. For each column specimen, the parameter values adopted for the *Concrete02* model were the same in all models. The adopted values are presented in Table 6.2, where f_{cm}, f_{cum}, and f_{ctm} are the mean values of compressive strength, residual compressive strength (20% of the maximum compressive strength) and tensile strength, respectively. The parameters ε_0, ε_u, and ε_{0t} are the strain corresponding to the compressive, residual and tensile strengths, respectively.

The *Steel02* model is based on the Giuffré-Pinto formulation, implemented later by Menegotto and Pinto [15]. For each column specimen, the values adopted for the *Steel02* model parameters were the same in the four models. The steel mechanical properties are those previously presented in Table 6.1. The values adopted for the other model parameters are presented in Table 6.3, where *bst* is the ratio between post-yield tangent and initial elastic tangent, and *R0* is the parameter that controls the transition from elastic to plastic branches.

The bar-stress slip model *Bond_SP01* model available in OpenSees was only assigned to the steel fibres in the zero-length section element. This generic model was proposed by Zhao and Sritharan [11] based on the results from pull-out tests of deformed steel reinforcing bars anchored in concrete footings with sufficient embedment length, loaded at the free end zone, specifically on the measured bar stress and loaded end slip evolutions [11]. The values adopted for the model parameters are indicated in Table 6.3, where α is a tuning parameter used for adjusting the local bond stress-slip relationship, b is

a stiffness reduction, and R is a pinching factor for the cyclic relationship between bar stress and slip. As stated above, the model was calibrated for elements with deformed bars. To take into account the presence of plain bars, parameter α was made equal to 0.5 in the model of specimen CPA-3, as recommended in [16]. For specimen CD, parameter α was made equal to 0.4, as in the model proposed by Zhao and Sritharan [11] and also as recommended in [16]. The slip values corresponding to the yielding strength (S_y) and ultimate strength (S_u) were computed using the equations proposed by Zhao and Sritharan [11].

Table 6.2 – Values adopted for the *Concrete02* model parameters.

Specimen	Concrete	f_{cm} (MPa)	ε_0 (‰)	f_{cum} (MPa)	ε_u (‰)	f_{ctm} (MPa)	ε_{0t} (‰)
CPA-3	Unconfined	17.4	2.1	3.5	10.0	2.0	0.24
	Confined	18.2	2.2	3.6	33.0	2.5	0.30
CD	Unconfined	17.1	2.1	3.4	10.0	2.0	0.24
	Confined	18.1	2.4	3.6	33.0	2.5	0.30

Table 6.3 – Values adopted for the *Steel02* and *Bond_SP01* model parameters.

Material model	Parameter	CPA-3	CD
Steel02	*bst*	0.037	0.044
	R0	12.0	15.5
Bond_SP01	α	0.50	0.40
	b	0.30	0.40
	s_y (mm)	0.46	0.44
	s_u (mm)	$40s_y$	$40s_y$
	R	0.30	0.80

6.3.3 Numerical modelling with SeismoStruct

The SeismoStruct is a finite element package capable of predicting the large displacements behaviour of space frames under static or dynamic loading, taking into account geometric nonlinearities and material inelasticity [17]. Several numerical models are available for concrete and steel materials as well as for the frame elements.

For each column specimen, two nonlinear models were built to simulate the columns response. Similarly to what was adopted for the OpenSees analysis, one model was built with inelastic frame elements with distributed plasticity (*infrmFB element*), whereas another model was built with inelastic plastic hinge frame elements (*infrmFBPH element*) with the nonlinearity concentrated within a fixed length of the element (plastic hinge). Both elements have a force-based formulation and the cross-sections are idealized through

fibre modelling. The effects of bar slippage were not incorporated in the SeismoStruct models here discussed.

With regard to the material models, the *con_ma* model and the *stl_mp* model available in SeismoStruct were adopted for the concrete and steel reinforcement, respectively.

The *con_ma* concrete model is an uniaxial nonlinear constant confinement model that follows the constitutive relationship proposed by Mander et al. [18]. The values adopted for the *Concrete02* model parameters in OpenSees (Table 6.2) were also adopted for the *con_ma* model parameters.

The *stl_mp* steel model is based on the stress-strain relationship proposed by Menegotto and Pinto [15], coupled with the isotropic hardening rules proposed by Filippou *et al.* [19]. The steel mechanical properties adopted are those previously presented in Table 6.1. Regarding the other model parameters, the default values indicated by SeismoStruct were adopted, except for R_0, which was made equal to 19.5 instead of 20.0 (default value). This parameter controls the shape of the transition curve between initial and post-yield stiffness.

6.4 NUMERICAL RESULTS

In this section are presented and discussed the results of the numerical analyses carried out to simulate the experimental response of two RC columns tested (presented in Chapter 3). Comparison is established between the numerical and experimental results, namely in terms of force-drift diagrams and energy dissipation. The drift values correspond to the column top lateral displacement divided by the height of the column (1.7m). The dissipated energy is the cumulative sum of the energy dissipation associated to each cycle, corresponding to the interior area of the loops in the force-drift diagrams.

It is recalled that the response of specimen CD is analysed only up to 3.5% drift, and not until 5% (maximum imposed drift), due to problems with the data acquisition system during the experiment.

6.4.1 Numerical results of the specimen with plain reinforcing bars

The comparison of the experimental force-drift diagrams for the column with plain reinforcing bars with those obtained from the numerical models under investigation is shown in Figure 6.5. The software platform used to conduct the numerical analysis, and the type of column element used to represent the column specimen are identified in the graphics.

The SeismoStruct models, with distributed plasticity or concentrated plasticity, provide a relatively better simulation of the column response when compared to the corresponding OpenSees models. A better approximation to the experimental results was attained namely in terms of the maximum strength and ultimate strength (force at maximum drift). The initial stiffness is however relatively better reproduced in the OpenSees models. Within the same software, a better fit to the experimental results was obtained by considering the plasticity concentrated in the plastic hinge regions, instead of distributed along the column' length. This aspect was particularly relevant in the OpenSees models. Thus, the differences in terms of maximum strength and ultimate strength were reduced from 2.7% to 0.5% and from 36.6% to 18.2%, respectively. Including the effects of bar slippage in the OpenSees models enhanced the numerical response namely in terms of stiffness of the unloading branches.

The best-fit to the experimental results was obtained by the OpenSees model with concentrated plasticity (*BeamWithHinges element*) and considering bar slippage (*zero-length section element*). Conversely, the worst simulation of the response of the column with plain reinforcing bars was provided by the OpenSees model with distributed plasticity. However, it should be noted that more of the models under investigation was able to properly capture the stiffness of the reloading branches, nor the strength degradation, nor the pinching effect.

The evolutions of dissipated energy determined from the experimental and numerical results are presented in Figure 6.6. Table 6.4 shows the ratio between the experimental and numerical values of cumulative dissipated energy at different imposed drift values. All the studied models overestimate the experimental values in terms of energy dissipation, particularly after 1% drift. The model that led to the best agreement between the numerical and experimental results was also the OpenSees model (OS) with concentrated plasticity

BeamWithHinges elements and *zero-length section element* (that is, considering the effects of bar slippage). At the maximum imposed drift, the corresponding dissipated energy is 38% higher than the obtained from the experimental results.

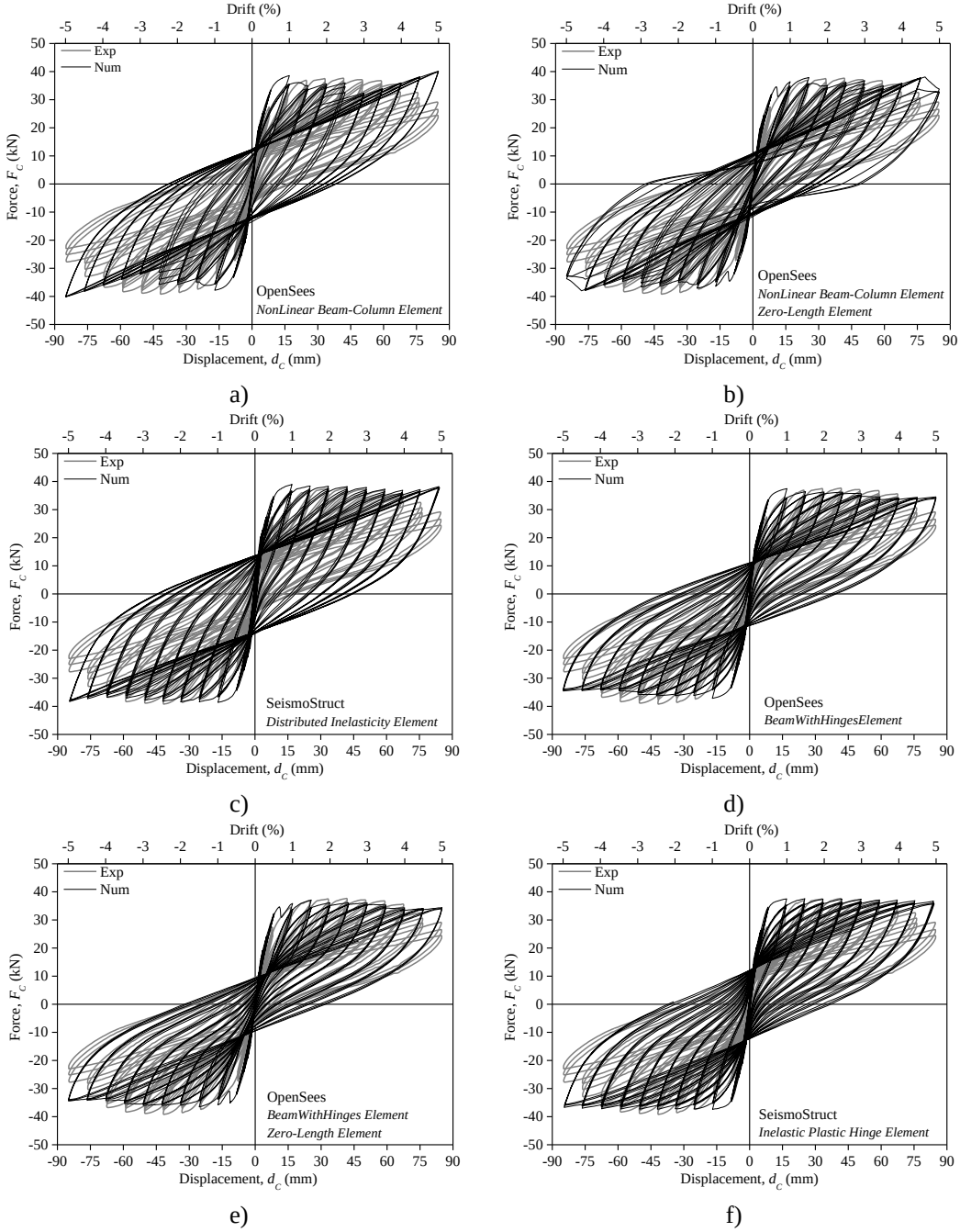

Figure 6.5 – Comparison between the experimental and numerical force-drift diagrams of specimen CPA-3: a), b) and c) numerical results considering elements with distributed plasticity; d), e) and f) numerical results considering elements with plastic hinges.

The results obtained with the SeismoStruct model (SS) with distributed plasticity elements gives larger differences. In this case, the dissipated energy obtained by the

numerical simulations at the maximum drift is about 2 times the obtained from the experimental results. Also, in accordance with what was previously concluded from the analysis of the force-drift diagrams, considering the plasticity concentrated in the plastic hinge regions instead of distributed along the column length led to a better reproduction of the dissipated energy evolution. By considering the effects of bar slippage, the differences in dissipated energy at the maximum drift between the numerical and experimental results are reduced in about 30%.

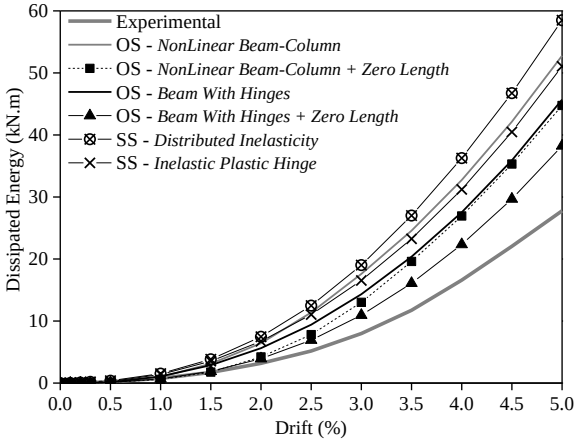

Figure 6.6 – Numerical and experimental dissipated energy evolutions of specimen CPA-3.

Table 6.4 – Numerical to experimental dissipated energy ratio for different levels of imposed drift in specimen CPA-3.

Element model	**Dissipated energy ratio**			
	Drift 1.0%	**Drift 2.0%**	**Drift 3.5%**	**Drift 5.0%**
OS – *NonLinear Beam-Column*	1.30	2.02	2.09	1.90
OS – *NonLinear Beam-Column + Zero Length*	0.79	1.32	1.67	1.61
OS – *Beam With Hinges*	1.43	1.77	1.74	1.65
OS – *Beam With Hinges + Zero Length*	0.91	1.24	1.37	1.38
SS – *Distributed Inelasticity*	2.02	2.35	2.30	2.11
SS – *Inelastic Plastic Hinge*	1.84	2.12	1.98	1.84

6.4.2 Numerical results of the specimen with deformed reinforcing bars

Figure 6.7 compares the experimental force-drift diagrams with those obtained from the numerical models under investigation. In the graphics, the software platform used to conduct the numerical analysis, and the type of column element used to represent the column specimen are identified.

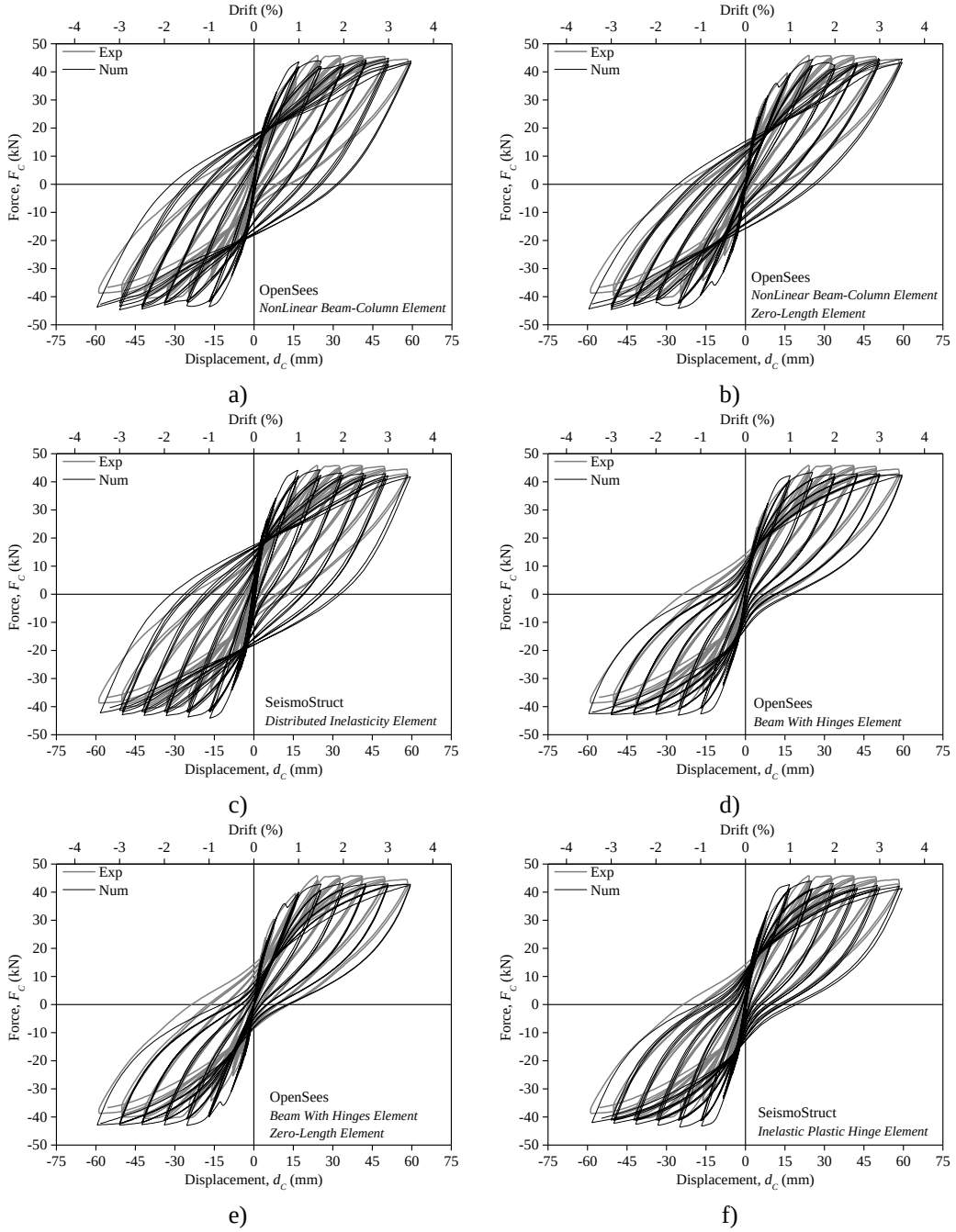

Figure 6.7 – Comparison between the experimental and numerical force-drift diagrams of specimen CD: a), b) and c) numerical results considering elements with distributed plasticity; d), e) and f) numerical results considering elements with plastic hinges.

The differences between the numerical results provided by the SeismoStruct models, with distributed plasticity or concentrated plasticity, and those provided by the corresponding OpenSees models are minor, in terms of both force and stiffness. Similarly to what was concluded for the column specimen with plain reinforcing bars, a better fit to the experimental results of the column specimen with deformed bars was obtained by considering the plasticity concentrated in the plastic hinge regions instead of distributed

along the column' length. In particular, the stiffness reduction evolution is significantly better simulated. The initial stiffness is, however, better simulated in the models with distributed plasticity. Adding the *zero-length section element* in the OpenSees models led to an enhancement of the results obtained in the numerical simulation in terms of the force-drift envelope.

As concluded for the column specimen with plain bars, the best-fit to the experimental force-drift response (namely to the corresponding peak envelope) was obtained by the OpenSees model with *BeamWithHinges element* and *zero-length section element*. However, as expected, the influence of the bars slippage effects in the numerical simulation of the column response, by adopting the *zero-length section element*, for the column with deformed bars is no as relevant as for the column specimen with plain bars.

Figure 6.8 depicts the numerical and experimental evolutions of dissipated energy. Table 6.5 gives the ratio between the experimental and numerical values of cumulative dissipated energy at different values of drift. All the tested models overestimate the experimental values in terms of energy dissipation, namely after 1% drift. The best-fit to experimental results was provided by the OpenSees (OS) model with *BeamWithHinges element* and *zero-length section element*. At the maximum drift, the corresponding dissipated energy obtained from those numerical results is 10% higher than the obtained from the experimental results. Conversely, the SeismoStruct (SS) model with *Distributed Inelasticity* element overestimated in 65% the energy at the maximum drift. By considering the effects of bar slippage, the differences in terms of dissipated energy (at the maximum drift) between the numerical and experimental results were reduced in 37% and 28%, relatively to the results obtained with the models with distributed plasticity and concentrated plasticity, respectively. For the column specimen with plain bars, the corresponding reductions (at 3.5% drift) are equal to 42% and 37%. Therefore, evidencing the importance of considering the effects of bar slippage in the simulation of the energy dissipation evolution for the specimen with plain bars. Comparing results in Table 6.4 and Table 6.5, it is shown that the evolution of dissipated energy was generally better reproduced for the specimen with deformed reinforcing bars than for the specimen with plain bars.

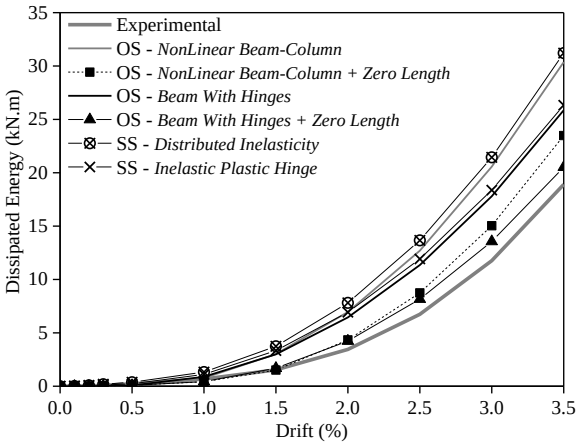

Figure 6.8 –Dissipated energy evolutions of specimen CD (numerical and experimental results).

Table 6.5 – Numerical to experimental dissipated energy ratio for different levels of imposed drift in specimen CD.

Element model	**Dissipated energy ratio**		
	Drift 1.0%	**Drift 2.0%**	**Drift 3.5%**
OS – NonLinear Beam-Column	1.13	2.02	1.61
OS – NonLinear Beam-Column + Zero Length	0.62	1.25	1.24
OS – Beam With Hinges	1.31	1.86	1.36
OS – Beam With Hinges + Zero Length	0.64	1.23	1.08
SS – Distributed Inelasticity	1.97	2.26	1.65
SS – Inelastic Plastic Hinge	1.64	2.01	1.39

6.5 A NEW SIMPLIFIED TRI-LINEAR REINFORCING STEEL MODEL FOR PLAIN BARS INCLUDING THE SLIPPAGE

A new empirical monotonic tri-linear model for the reinforcing plain bars including the slippage effects is here proposed. This simplified model was calibrated against the experimental results of eight columns. The methodology adopted in the model and the comparisons between the experimental and numerical results are presented.

6.5.1 Assumptions and calibration of the proposed simplified model

In the numerical models, the bond-slip effects can be introduced by adopting different strategies. One is considering a *zero-length section*, as adopted in the analyses discussed in the previous section. Another possible strategy is based on the inclusion of springs along the reinforcing steel bars, or in specific sections in order to simulate the slippage concentrated at particular regions. However, the bar slippage phenomenon develops along the reinforcing bar and cannot be precisely reproduced considering as concentrated in some

points. A simple strategy to consider the bond-slip effects can be developed modifying the uniaxial steel model by reducing the Young' modulus [20]. Reducing the Young modulus of the steel, the RC elements becomes more flexible and their maximum strength is achieved for larger drift demands than considering the nonmodified Young steel modulus.

Figure 6.9 shows the stresses distribution and forces that develop in a generic cross-section of a RC element when loaded in bending and axial load. The forces on concrete and steel fibres that occur in the section depend on the stress-strain uniaxial law idealized for the concrete and steel. Eurocode 2 part 1-1 [21] propose a parabolic-rectangular stress-strain diagram for confined concrete, which was adopted in the present study (see Figure 6.10a). Eurocode 2 part 1-1 [21] also presents a bilinear stress-strain diagram idealized for reinforcing steel. To consider the bar slippage, a new tri-linear steel stress-strain diagram is proposed for the representation of the reinforcing steel including the bar slippage effect (see Figure 6.10b). The multi-linear models are commonly used to simulate the behaviour of the materials in the fibre section or to simulate the global behaviour of a section [22].

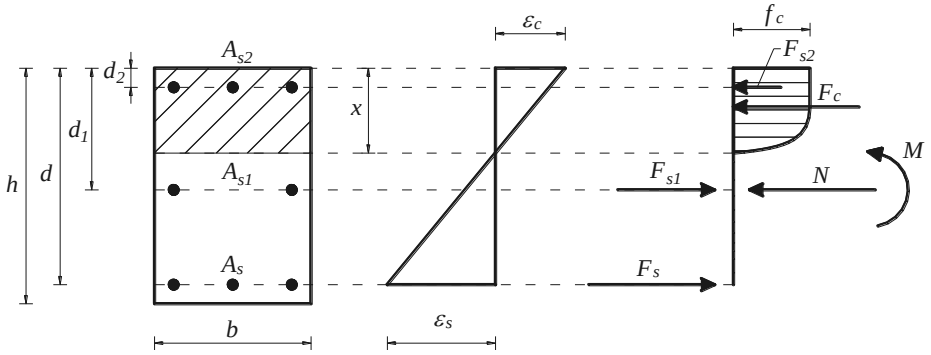

Figure 6.9 – Idealized stress distribution in a section subjected to bending and axial load.

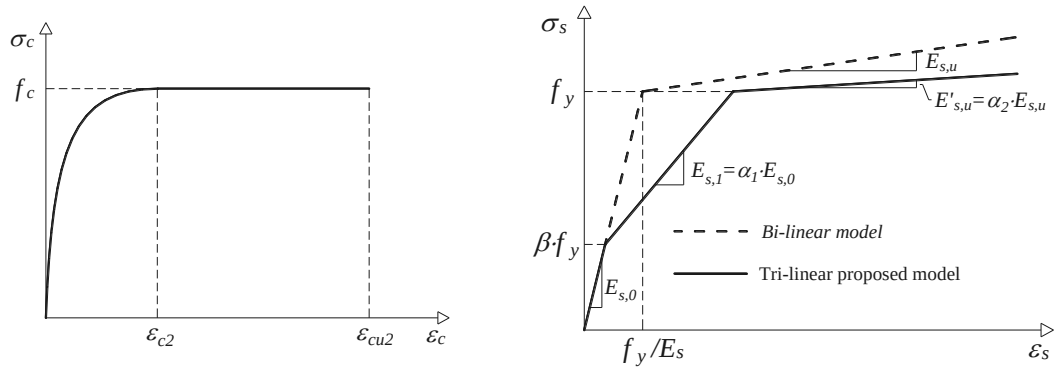

a) b)

Figure 6.10 – Idealized stress-strain diagrams: a) concrete; and b) reinforcing steel.

The first branch of the tri-linear reinforcing steel model is characterized by the steel Young modulus ($E_{s,0}$) up to $\beta \cdot f_y$, where f_y is the steel yield stress and β is an empirical parameter. The slope of the second branch ($E_{s,1}$) is reduced relatively to the slope of the first branch, multiplying by the empirical factor α_1. The slope of the third branch is given by the original hardening slope ($E_{s,u}$) multiplied by the empirical factor α_2.

Analytical expressions were developed to obtain the moment-curvature relationship for a generic section, as shown in Figure 6.9. The idealized uniaxial stress-strain materials' diagrams presented in Figure 6.10 were considered to compute the section forces (F_c, F_s, F_{s1} and F_{s2}) considering the equilibrium at section level. In the analytical approach, it is assumed that the conservation of the plaine sections.

Based on the experimental moment-curvature diagrams obtained in eight cyclic tests carried out on columns with plain reinforcing bars [9], as reported in Chapter 3, the parameters β, α_1 and α_2 of the modified tri-linear steel model were empirically obtained. The parameters for the analytical moment-curvature relationship better matching the corresponding experimental moment-curvature relationships where derived. The best-fits of the moment-curvature diagrams for the eight elements with plain bars were obtained for a β parameter given by Equation (6.1), α_1=0.085 and α_2=0.30, where h represents the cross-section depth in meters.

$$\beta = -1.39 \cdot h + 0.85 \tag{6.1}$$

For the specimen with deformed reinforcing bars (CD) the corresponding parameters obtained are β=0.45, α_1=0.25 and α_2=0.50.

6.5.2 Numerical validation of the proposed model

Two numerical models were developed in OpenSees for the simulation of the envelope of the cyclic response of columns CPA-3 and CD. One model was developed without taking into account the slippage effects and the other considering the slippage by using the proposed tri-linear steel model. The model without the slippage effect corresponds to the model used in the previous section (with *nonlinearBeamColumn element*), but the lateral load imposed now is monotonic. For the model that considers the slippage effect, it was used the *nonlinearBeamColumn element*, the *Concrete02* for simulation of the uniaxial concrete behaviour and the *Hysteretic* model for the steel reinforcement. *Hysteretic* is a

uniaxial multi-linear hysteretic material model, with pinching and degradation of unloading stiffness with ductility demand [12]. In this case, the adopted values for the material model *Hysteretic* follows the stress-strain diagram presented in Figure 6.10b. The parameters β, α_1 and α_2 obtained as reported in previous section were adopted in this comparative analysis.

Figure 6.11 compares the monotonic curves obtained with the numerical models (with and without slippage) with the experimental results. The proposed steel reinforcement model with slippage adopted in the numerical analyses better represented the experimental results. The benefits of using the new tri-linear steel model are much more evident in the column with plain bars (CPA-3). According to Figure 6.5 and Figure 6.7 and for drift demands ranging from 0.5% to 1.5%, the strength associated to the numerical models without *zero-length section element* are considerable larger than the strength of the tested columns. Therefore, the proposed simplified steel model improves the representation of the response of RC elements, which is particularly useful for models that do not allow for the inclusion of *zero-length section element*. This is particularly important for elements subjected to important bond-slip effects, as for RC elements with plain reinforcing bars subjected to large cyclic or monotonic demands.

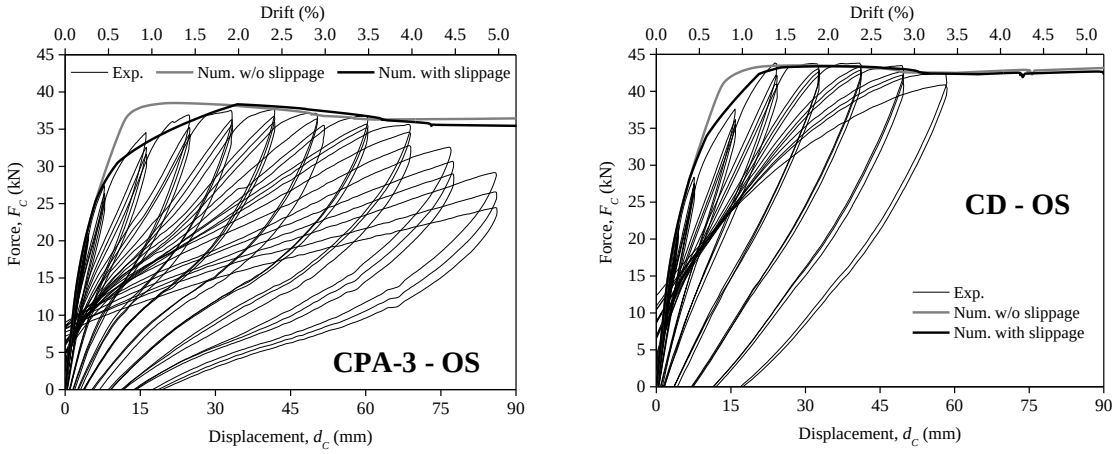

a) b)

Figure 6.11 – Numerical (with and without slippage) and experimental force-displacement relationships: a) column CPA-3; and b) column CD.

6.6 CONCLUSIONS

A parametric study was developed to investigate the adequacy of different models to simulate the cyclic behaviour of two analogous RC columns, one built with plain reinforcing bars and another with deformed reinforcing bars. The numerical models were

built in the OpenSees and the SeismoStruct platforms. Within each platform, nonlinear column elements with distributed plasticity or concentrated plasticity were used to represent the columns. The influence of considering or not the effects of bar slippage in the numerical response was also investigated. For each column specimen, a comparison was established between the numerical and experimental results, namely in terms of force-drift diagrams and evolution of dissipated energy. It is also proposed a new simplified tri-linear steel material model which takes into account the slippage of reinforcing bars.

All developed models, generally, provided a satisfactory simulation of the experimental force-drift diagrams. However, none of the models was able to properly capture the strength degradation, nor the stiffness of the reloading branches, nor the pinching effect (namely in the response of the column specimen with plain bars). The results obtained with the models built in OpenSees and SeismoStruct (considering distributed or concentrated plasticity) are similar for the column with deformed bars. Disregarding the effects of bar slippage, a better fit to the experimental results of the column with plain bars was obtained using the model in OpenSees.

For both column specimens, a better agreement between the numerical and experimental results (in terms of force, stiffness and energy dissipation) was obtained considering the non-linearities concentrated in the plastic hinge regions, either in OpenSees and in SeismoStruct models. This was particularly relevant for the column with plain reinforcing bars, namely in terms of stiffness evolution and energy dissipation.

The uniaxial tri-linear steel model proposed in this work, associated to the fibre section model, led to a better representation of the experimental response than the obtained considering the common steel model (*Steel02*). This result was much more pronounced for the column with plain reinforcing bars, where the slippage develops largely.

The results of the analyses presented confirm the importance of the inclusion of the bond-slip effects in the numerical modelling of RC structural elements with plain reinforcing bars subjected to large demands. However, it is considered essential to develop additional analyses for the validation of the proposed model with a larger experimental database. Also, the proposed model should be upgraded in order to allow for the representation of the cyclic response of RC columns.

6.7 REFERENCES

[1] Ioannou I, Borg R, Novelli V, Melo J, Alexander D, Kongar I, Verrucci E, Cachill B, Rossetto T. The 29th May 2012 Emilia Romagna Earthquake – EPICentre field observation report. No. EPI-FO-290512, University College London, Department of Civil, Environmental and Geomatic Engineering, 2012.

[2] Rossetto T, Peiri N, Alarcon J, So E, Sargeant S, Sword-Daniels V, Libberton C, Verrucci E, Re D, Free M. The L'Aquila, Italy Earthquake of 6 April 2009 – A preliminary field report by EEFIT. The Earthquake Engineering Field Investigation Team, University College London, Department of Civil, Environmental and Geomatic Engineering, 2009.

[3] Monti G, Spacone E. Reinforced concrete fiber beam element with bond-slip. *Journal of Structural Engineering* 2000:126:6:654-661.

[4] Chen G, Baker G. Influence of bond slip on crack spacing in numerical modeling of reinforced concrete. *Journal of Structural Engineering* 2003:129:11:1514-1521.

[5] Sezen H, Setzler EJ. Reinforcement slip in reinforced concrete columns. *ACI Structural Journal* 2008:105:3:280-289.

[6] Kwak HG. Improved numerical approach for the bond-slip behavior under cyclic loads. *Structural Engineering and Mechanics* 1997:5:5:663-677.

[7] Youssef M, Ghobarah A. Strength deterioration due to bond slip and concrete crushing in modeling of reinforced concrete members. *ACI Structural Journal* 1999:96:6:956-966.

[8] Melo J, Fernandes C, Varum H, Rodrigues H, Costa AG, Arêde A. Numerical modelling of the cyclic behaviour of RC elements built with plain reinforcing bars. *Engineering Structures* 2011;33:2:273-286. doi: 10.1016/j.engstruct.2010.11.005.

[9] Melo J, Varum H, Rossetto T. Experimental cyclic behaviour of RC columns with plain bars and proposal for Eurocode 8 formula improvement. *Engineering Structures* 2014. Accepted

[10] Spacone E, Filippou F, Taucer F. Fibre beam-column model for non-linear analysis of R/C frames: part II. Applications. *Earthquake Engineering and Structural Dynamics* 1996:25:727-742.

[11] Zhao J, Sritharan S. Modelling of strain penetration effects in fibre-based analysis of reinforced concrete structures. *ACI Structural Journal* 2007:104:2:133-141.

[12] Mazzoni S, McKenna F, Scott MH, Fenves GL. OpenSees command language manual. Pacific Earthquake Engineering Research Center, University of California, Berkeley, U.S.A., 2007.

[13] Hognestad E. A Study of combined bending and axial load in reinforced concrete. Bulletin Series 339. Univ. of Illinois Exp. Sta., Illinois, U.S.A., 1951.

[14] Guedes JM. Seismic behaviour of reinforced concrete bridges. Modelling, numerical analysis and experimental assessment. PhD Thesis. Faculty of Engineering of the University of Porto, Porto, Portugal, 1997.

[15] Menegotto M, Pinto P. Method of analysis for cyclically loaded reinforced concrete plane frames including changes in geometry and non-elastic behaviour of elements under combined normal force and bending. In: IABSE Symposium: Resistance and Ultimate Deformability of Structures Acted on by Well Defined Repeated Loads, Final Report, Lisbon, Portugal, 1973.

[16] FIB, Task Group 2.5: Bond models; Bond of reinforcement in concrete. State-of-the-art report. FIB Bulletin 10, Lausanne. ISBN 978-2-88394-050-5, 2000.

[17] Seismosoft; Seismostruct, available on the internet site: http://www.seismosoft.com/en/SeismoStruct.aspx, 2014.

[18] Mander JB, Priestley MJN, Park R. Theoretical stress-strain model for confined concrete. *Journal of Structural Engineering* 1988:114:8:1804-1826.

[19] Filippou FC, Popov EP, Bertero VV. Effects of bond deterioration on hysteretic behaviour of reinforced concrete joints. Report EERC 83-19, Earthquake Engineering Research Center, University of California, Berkeley, 1983.

[20] Varum, H. Seismic assessment, strengthening and repair of existing buildings. PhD Thesis, University of Aveiro, Portugal, 2003.

[21] CEN, NP EN 1992-1-1. Eurocode 2, Design of concrete structures. Part 1-1: General rules and rules for buildings. European Committee for Standardization, Brussels, Belgium, 2010.

[22] Arêde A. Seismic assessment of reinforced concrete frame structures with a new flexibility based element. PhD Thesis. Faculty of Engineering of the University of Porto, Porto, Portugal, 1997.

CHAPTER 7

CONCLUSIONS AND FUTURE WORK

7.1 CONCLUSIONS

This thesis deals with the experimental assessment of the cyclic behaviour of RC columns and beam-column joints built with plain reinforcing bars and without adequate detailing for seismic demands. The influence of the bond-slip mechanism and reinforcement detailing on the cyclic response of RC elements was detailed studied. The bond-slip relationship for plain reinforcing bars was also characterised.

Based on the obtained pull-out test results, new empirical expressions were proposed to compute the values of the parameters for the Verderame et al. [1] bond-slip modified model. Moreover, a new constitutive bond-slip relationship was proposed better representing the bond-slip after peak bond strength. The proposed empirical expressions take into account additional parameters affecting the bond-slip mechanism.

The test results on full-scale RC elements (columns and beam-column joints) carried out in the scope of this thesis have shown the crucial role of the bond between the reinforcing bars and the surrounding concrete on the cyclic response of RC structural elements with plain reinforcing bars. The effects of bar slippage were particularly important on the dissipation energy capacity, on the ultimate rotation capacity and on the damage distribution of the tested RC elements. The different detailing of the plain reinforcing bars studied in the RC elements cyclically tested also influenced significantly their response, especially for the exterior beam-column joints.

The experiments on RC columns demonstrated the large slippage contribution to the column deformation (up to 43% increase in the total lateral drift when compared to similar specimens with deformed bars, for the same lateral load). These results are aligned with observations made by other authors [2] for RC beams.

The ultimate rotation capacity of RC elements with plain reinforcing bars computed according to EC8-3 [3] expressions seems to be conservative. Moreover, a large dispersion of results was observed. A new correction coefficient (a_{slip}) was proposed to correct the EC8-3 formula, reducing the results' dispersion and better estimate the ultimate rotation capacity of elements with plain reinforcing bars.

The methodology adopted to compute the energy dissipation at the joint, beams and columns in the interior beam-column joints represents on average 95% of the total hysteretic energy obtained experimentally. Therefore, the methodology adopted allows to obtain the evolution of the dissipated energy by each individual component with adequate accuracy, which permits a better understanding of the complex behaviour of these joints.

The EC8-1 [4] formulation to compute the shear capacity of the joint did not predict the experimental results accurately, especially for the exterior beam-column joints. The reinforcement ratio in the joint might be considered in future improvements of EC8-1 formulation to calculate the horizontal shear capacity.

From the experiments on exterior beam-column joints, the significance of the reinforcement anchorage detailing of the beam to avoid the concrete wedge mechanism was shown. In the core joints without transversal reinforcement, the anchorage of plain bars should not simply consist of a 180 degree end hook at the beam exterior face. But, rather, a 90 degree bend at this point and extending the bar down to the bottom of the joint, where a 180 degree end hook should be adopted.

In the numerical models developed for columns, a better agreement between the numerical and experimental results (in terms of force, stiffness and energy dissipation evolutions) was obtained considering the non-linearities concentrated in the plastic hinge regions. Considering the effects of bar slippage revealed to be essential to reproduce accurately the experimental results.

The new tri-linear steel model proposed, incorporating the slippage, led to a closer match between the numerical results and the experimental response observed in the tested columns with plain reinforcing bars.

This thesis intended to provide a contribution to the state-of-the-knowledge on the behaviour of RC elements reinforced with plain bars and on the associated bond-slip mechanism. The available experimental data on RC elements with reinforced with plain bars was significantly enlarged, which can be used to propose new empirical expressions and to upgrade and to calibrate the available numerical models for simulating the cyclic behaviour of RC elements.

7.2 FUTURE WORK

The work developed in this thesis has contributed to enlarge the available experimental data of cyclically loaded RC elements with plain reinforcing bars. However, the database of RC elements with plain bars is still not sufficient for the full knowledge of these type of elements. Moreover, some of the empirical expressions proposed in this thesis cannot be applied in all typologies of RC elements with plain bars, as a consequence of the scarce data available in the literature. As future research work, among many possibilities, it would be stimulating to:

- Extend the experimental test campaign to beam-column joints with slab on both sides and with transversal beams;
- Perform biaxial cyclic tests on RC columns and beam-column joints with plain reinforcing bars and to compare the experimental results with the results obtained in the uniaxial cyclic tests;
- Study the influence of varying axial load on the cyclic response of columns and beam-column joints with plain reinforcing bars;
- Test RC elements with plain reinforcing bars collected from existing structures;
- Verify the influence of the testing procedure (under displacement control or under force control) in the results of pull-out tests of plain reinforcing bars;
- Develop additional numerical analyses for the validation of the proposed tri-linear steel model with all the available experimental database;

- Upgrade the tri-linear steel model proposed in this thesis in order to allow for the representation of the cyclic response of RC columns;
- Develop and calibrate non-linear models for interior beam-column joints including the bond-slip mechanism and shear deformation of the joint;
- Carry out an experimental campaign specifically for the assessment of the ultimate rotation capacity of RC elements with plain reinforcing bars, covering the representative scenarios of RC elements in existing structures;
- With the experimental results of RC elements with plain reinforcing bars, and with the available models, study the seismic response of structures representative of old RC buildings;
- Develop and calibrate a model for the prediction of the shear capacity of beam-column joints with plain reinforcing bars and without transversal reinforcement in the joint core;
- Design and test strengthening solutions to improve the bond between the reinforcing bar and the surrounding concrete;
- Design and test strengthening solutions to improve the shear capacity of the joint core in beam-column joints with plain reinforcing bars.

7.3 REFERENCES

[1] Verderame GM, Ricci P, Carlo GD, Manfredi G. Cyclic Bond Behavior of Plain Bars. Part II: Analytical Investigation. *Construction and Building Materials* 2009:23(12):3512-3522. doi: 10.1016/j.conbuildmat.2009.07.001

[2] Marefat M, Shirazi S, Rostamshirazi R, Khanmohammadi M. Cyclic response of concrete beams reinforced by plain bars. *Journal of Earthquake Engineering* 2009:13:463-481.

[3] CEN. BS EN 1998-3:2005. Eurocode 8: Design of structures for earthquake resistance. Part 3: Strengthening and repair of buildings. European Committee for Standardization. Brussels. Belgium, 2005.

[4] CEN, NP EN 1998-1, Eurocode 8, Design of structures for earthquake resistance - Part 1: General rules, seismic actions and rules for buildings. European Committee for Standardization, Brussels, Belgium, 2010.